

Metal Halide Perovskites for Photocatalytic Organic Synthesis

Haowei Huang

Supervisor:

Prof. dr. ir. Roeffaers Maarten, KU Leuven

Members of the Examination Committee:

Prof. dr. ir. Aerts Jean-Marie, KU Leuven, Chairman

Prof. dr. Hofkens Johan, KU Leuven, Co-supervisor

Prof. dr. Ujii Hiroshi, KU Leuven

Prof. dr. ir. Ameloot Rob, KU Leuven

Dr. Debroye Elke, KU Leuven

Dr. Douthwaite Richard, University of York

Dissertation presented in
partial fulfilment of the
requirements for the
degree of Doctor of
Bioscience Engineering
(PhD)

May 2020

Doctoraatsproefschrift nr. 1429 aan de faculteit Bio-ingenieurswetenschappen van de KU Leuven

© 2020 KU Leuven, Science, Engineering and Technology

Uitgegeven in eigen beheer, Haowei Huang, Leuven

Alle rechten voorbehouden. Niets uit deze uitgave mag worden vermenigvuldigd en/of openbaar gemaakt worden door middel van druk, fotokopie, microfilm, elektronisch of op welke andere wijze ook zonder voorafgaandelijke schriftelijke toestemming van de uitgever.

All rights reserved. No part of the publication may be reproduced in any form by print, photoprint, microfilm, electronic or any other means without written permission from the publisher.

Preface

It is not the first time to write some farewell words, but still not easy. It has been three years since the first time I arrived at Leuven. Despite the fear of uncertainty for the future and the reluctance of leaving, the time in Leuven has offered me a lot of mixed feelings with much joys and sorrows, which I should acknowledge are essential parts of my personal development.

First of all, I would like to thank my supervisor, Prof. Maarten Roeffaers. In the last three years, he is always supportive of me. He has provided me with a free and creative platform to achieve my academic ideas and pursuit my academic dreams, which is essential for me to develop as an independent researcher. Then, thanks would go to my co-supervisor, Prof. Johan Hofkens, who always offer invaluable suggestions to my research project. I am also grateful to my assessors Prof. Rob Ameloot and Prof. Hiroshi Ujii, for their useful discussions and advices in supervisory committee meetings.

In Maarten's group, I would like to thank Collin, firstly. I still remember he picked me up at Leuven station at the first day I arrived at Leuven. He helped me to fit into an unfamiliar environment quickly. To Haifeng, I feel so lucky to have his company during my PhD. Not only he shared lots of experiences and knowledge on experiment with me but also I received lots of help from him in daily life. Weiyi and Kangwei, I would like to thank them for sharing with some interesting ideas. Julian, he is always nice and friendly; I really enjoy the discussions, collaboration and joint article-writing with him. In addition, I would like to thank all the members in Maarten's lab.

Furthermore, I would like to thank my Chinese collaborators, Prof. Jinlin Long and the members in his lab. He is so generous to open all the setups in his lab for me and give lots of suggestions on my research.

Thanks to Handong, Gang, Chunhua, Li, Chen and some other good friends in Belgium, we have so much fun after work, which helped me to get refreshed especially when I was exhausted from the work. Their company made my PhD life more colorful and gave me a sense of belonging in Leuven.

I would also like to thank the financial support from the European Union (Horizon 2020) Marie Skłodowska-Curie innovation program, phototrain, which enabled me to undertake this PhD.

Lastly, but most importantly, I would like to thank my family. My wife, Wei, always supports me in many ways. I cannot image the life without her in the last decades, and also in the future. I feel sorry to my son Yicheng as I have been absent in his first few years of his childhood. I know I am not a good father in that respect but feel very pleased that he is such a lovely boy. I am extremely grateful for everything my parents have done for me. I cannot be here without all of you.

It is not a time to say goodbye but it is a time to embrace a new stage of life.

May 2020, in Leuven

Abstract

Since Fujishima and Honda first reported in 1972 the photoelectrochemical water splitting of water through TiO_2 under UV light irradiation, photocatalysis has attracted a growing amount of research attention. Various types of materials with photocatalytic properties such as metal oxides, metal sulfides, polymers, MOFs etc have been reported for solar energy conversion, storage and utilization, through reduction and/or oxidation reactions generating added value products including hydrogen, oxygen and hydrocarbons. Recently, metal halide perovskites (MHPs) have found tremendous popularity in solar to electricity conversion due to the high extinction coefficients, the wide absorption range and long electron-hole diffusion lengths of these materials. All of the mentioned MHP properties match well with the necessary conditions set forward for photocatalytic materials making them potentially interesting photocatalyst, a main concern is however related to their (chemical) stability under reaction conditions.

In Chapter 1, the concept of photocatalysis and the development of photocatalytic materials in the last decades are discussed. Next, the photoelectric properties of MHPs are highlighted with an emphasis on their potential as cheap and easy to generate photocatalytic material. After that, the issues hampering MHP-based photocatalysis are identified and general approaches to achieve promising and stable photocatalytic reaction environments are pointed out. Further, we detail the measures being taken to arrive at intrinsically stable photocatalytic materials, removing the need for atypical environments.

Chapter 2 reports on the utilization of formamidinium lead bromide (FAPbBr_3) as photocatalyst for the selective oxidation of benzylic alcohols to corresponding aldehydes in toluene. With 8 h of solar light irradiation, roughly 15% conversion of 0.1 mmol benzyl alcohol in 2.5 ml toluene with near 100% selectivity was achieved using only 10 mg of photocatalysts. To further improve the photocatalytic activity of FAPbBr_3 , a hybrid material with TiO_2 , $\text{FAPbBr}_3/\text{TiO}_2$, was prepared by the in-situ anti-solvent growth. The TiO_2 extract the photo-generated electrons from FAPbBr_3 reducing the charge carrier recombination and enhancing the relative photocatalytic efficiency. The best results were obtained with a 15 wt % $\text{FAPbBr}_3/\text{TiO}_2$ composite with conversion 4 times larger compared to the pristine perovskite material.

The scope of selective chemical conversions that can be photocatalysed with MHPs is expanded in Chapter 3. Here, FAPbBr₃ was used for the more challenging C(sp³)-H activation in alkanes. Inspired by MHPs solar cell structure, the addition of an electron transfer layer (TiO₂) as well as an hole transfer layer (NiO_x) allows for further optimization of the conversion efficiency, by further improving the charge separation properties. This TiO₂/FAPbBr₃/NiO_x construction achieved high conversions of C(sp³)-H bond in alkanes to form aldehydes with excellent selectivities (86 %).

The small bandgap of metal halide perovskites is successfully employed in Chapters 1 and 2 to enable efficient visible light photocatalysis. This small bandgap is however also accompanied by a weak redox ability. Band alignment in the FAPbBr₃/TiO₂ and NiO_x/FAPbBr₃/TiO₂ composites further decreases the redox ability. In chapter 4, a perovskite-based direct Z-scheme photocatalyst, consisting of FAPbBr₃ and Bi₂WO₆, is generated for efficient artificial photosynthesis. To maximally utilize the gained redox ability of the Z-scheme photocatalyst, the CO₂ reduction is coupled to the benzyl alcohol oxidation. Under solar light irradiation, CO and benzaldehyde generation rate reached a maximum of 170 μmol/g/h and 250 μmol/g/h, respectively.

Overall, in this PhD metal halide perovskites, with FAPbBr₃ as prime example, were used to drive organic reactions through visible light photocatalysis. Type II heterojunctions, including single junction and dual-junctions, were successfully generated to optimize charge carrier separation and transportation yielding a strongly improved photo-activity. Next, a direct Z-scheme photocatalyst with strong redox ability, consisting of FAPbBr₃ and Bi₂WO₆, was used to drive organic synthesis coupled with CO₂ reduction. Overall, this work opens a new window for applying MHPs photocatalysis in organic synthesis and also proposes some strategies to improve the activity.

Samenvatting

In 1972 rapporteerde Fujishima en Honda voor het eerst de foto-elektrochemische water splitsing onder UV-lichtbestraling door gebruik te maken van TiO_2 . Dit werk stimuleerde het verdere onderzoek naar tot de ontwikkeling van fotokatalytische materialen voor het gebruik, de conversie en de opslag van zonne-energie. Recentelijk zijn metaalhalogenide perovskieten (MHPs) succesvol geïmplementeerd in de nieuwste generatie zonnecellen. Ze danken dit toenemend succes aan hun opmerkelijke eigenschappen zoals hoge extinctiecoëfficiënten, lichtabsorptie over een breed spectrum en lange elektron-hole-paar leeftijden. Deze eigenschappen maken MHPs ook potentieel interessante voor het gebruik als fotokatalysatoren. Het enige minpunt dat momenteel het gebruik van deze materialen op grote schaal hindert is hun beperkte (chemische) stabiliteit.

In Hoofdstuk 1 wordt het concept van fotokatalyse en de ontwikkeling van fotokatalysatoren in de laatste decennia samengevat. Vervolgens worden de verschillende foto-elektrische eigenschappen van MHPs besproken inclusief de beperkingen en problemen die MHP-gebaseerde fotokatalyse belemmeren. Recent zijn er enkele experimentele oplossingen uitgewerkt waarbij MHPs succesvol als fotokatalysator kunnen worden gebruikt. Deze oplossingen alsook de maatregelen die kunnen genomen worden om intrinsiek stabiele MHP fotokatalysatoren te creëren worden uitgebreid besproken.

Hoofdstuk 2 beschrijft het gebruik van formamidinium loodbromide (FAPbBr_3) als fotokatalysator voor de selectieve oxidatie van benzyalcoholen tot hun overeenkomstige aldehyden in toluen. Na een irradiatietijd van 8 uur met zonlicht werd ongeveer 15% van de 0.1 mmol benzyalcohol oplossing in 2.5 ml toluen geconverteerd, met een selectiviteit van bijna 100%. Om de activiteit van FAPbBr_3 verder te verbeteren, werden hybride materiaal bereid met TiO_2 . TiO_2 extraheert de foto-gegenereerde elektronen uit FAPbBr_3 . Met amper 15 wt% $\text{FAPbBr}_3/\text{TiO}_2$ werd een activiteit bekomen die ruim 4 hoger ligt in vergeleken met de pure MHP.

Meer uitdagende organische reacties, werden bestudeerd in Hoofdstuk 3. Hier werden MHPs gebruikt voor de fotokatalytische conversie van alkanen in aldehyden. Geïnspireerd door de MHPs zonnecelstructuur, werd zowel een elektronen- (TiO_2) als hole-extractiemateriaal (NiO_x) toegevoegd. Deze

hybride structuur optimaliseert de conversie-efficiëntie door een verbeterde ladingsscheiding. Met deze $\text{TiO}_2/\text{FAPbBr}_3/\text{NiO}_x$ werden hoge omzettingsefficiënties van alkanen in aldehydes bekomen.

De kleine bandgap van MHPs verbetert de zonlicht absorptie in FAPbBr_3 maar zorgt er bovendien ook voor dat deze materialen maar een beperkt redox-vermogen bezitten. De combinatie met ladingsscheidingslagen in $\text{FAPbBr}_3/\text{TiO}_2$, $\text{NiO}_x/\text{FAPbBr}_3/\text{TiO}_2$ verzwakt dit redoxvermogen verder. In Hoofdstuk 4 wordt de ontwikkeling van een perovskiet-gebaseerde directe Z-scheme fotokatalysator besproken. Deze hybride fotokatalysator combineert FAPbBr_3 met Bi_2WO_6 . Met zichtbaar licht wordt de fotoreductie van CO_2 gekoppeld aan benzylalcoholoxidatie, hierbij wordt respectievelijk $170 \mu\text{mol/g/h}$ CO en $250 \mu\text{mol/g/h}$ benzaldehyde gevormd.

In dit doctoraatswerk werden de fotokatalytische eigenschappen van MHPs, met FAPbBr_3 als voorbeeldmateriaal, bestudeerd voor verdere toepassingen in bepaalde selectieve organische reacties zoals de oxidatie van alcoholen en alkanen naar de overeenkomstige aldehyden. De toevoeging van ladingsscheidingslagen met de vorming van type II heterojuncties werd succesvol toegepast om een betere foto-activiteit te verkrijgen. Vervolgens werd een direct Z-scheme fotokatalysator met sterk redox-vermogen, bestaande uit FAPbBr_3 en Bi_2WO_6 , gebruikt om een organische reactie aan te sturen in combinatie met CO_2 -reductie. Dit werk beschrijft de succesvolle de toepassing van MHPs als selectieve katalysatoren voor organische conversies. Verder werden enkele veelbelovende strategieën uitgewerkt om de katalytische activiteit te verbeteren.

List of abbreviations

Metal halide perovskites - MHPs
Formamidinium - FA
Normal Hydrogen Electrode - NHE
Graphene oxide - GO
Carbon quantum dots - CQDs
Metal-Organic Framework Compounds - MOFs
Valence band maximum - VBM
Conduction band minimum - CBM
Dimethyl sulfoxide - DMSO
Methylammonium - MA
Reduced graphene oxide - rGO
Photoelectrochemical - PEC
Graphitic carbon nitride - g-C₃N₄
Turnover number - TON
Electron transport layer - ETL
Hole transport layer - HTL
[6,6]-phenyl-C61-butyric acid methyl ester- PCBM
Ethoxylated polyethylenimine - PEIE
Graphite sheet - GS
Organic-inorganic halide perovskites - OIHPs
Photoluminescence - PL
PL quantum yield - PLQY
Electron spin resonance - ESR
5,5-dimethyl-pyrroline N-oxide - DMPO
N,N-Dimethylformamide - DMF
X-ray diffractometry - XRD
Scanning electron microscopy - SEM
X-ray photoelectron spectroscopy - XPS

Time-correlated single photon counting - TCSPC
Instrument response functions - IRF
High resolution TEM micrograph - HRTEM
Time-resolved photoluminescence - TRPL
Toluene - Tol
Benzaldehyde - BD
Benzyl alcohol - BA
Turnover frequency - TOF
Apparent quantum efficiency - AQE
Density functional theory - DFT
Atomic force microscopy - AFM
Transmission electron microscopy -TEM
UV-visible diffuse reflectance spectroscopy - DRS
Ultraviolet photoelectron spectroscopy - UPS
Fourier transform infrared - FTIR
Transient absorption - TA
fs-ps time-resolved IR transient absorption - fs-ps IR
ns- μ s time-resolved IR transient absorption - ns- μ s IR
FAPbBr₃/Bi₂WO₆ - FA/Bi
NiO_x/FAPbBr₃/TiO₂ - Ni/FA/Ti
Full width at half maximum - FWHM

Table of Contents

Preface	I
Abstract.....	III
Samenvatting	V
List of abbreviations.....	VII
Table of Contents.....	IX
Chapter 1 Introduction	1
1.1 Overview	2
1.2 Instability parameters of perovskite.....	5
1.3 MHPs photocatalysis.....	9
1.3.1 Halogen acid solution for photocatalytic hydrogen evolution	9
1.3.2 Apolar and low-polar solvent stabilization	14
1.3.3 Encapsulation and core-shell structure	23
1.3.4 Polar solvent stabilization of MHPs	29
1.4 Project aim	32
1.5 References	34
Chapter 2 Efficient and Selective Photocatalytic Oxidation of Benzylic Alcohols with Hybrid Organic– Inorganic Perovskite Materials	45
2.1 Introduction	47
2.2 Results.....	48
2.3 Conclusion.....	55
2.4 Experiment section	56
2.5 References	59
2.7 Supporting information.....	62
Chapter 3 C(sp ³)–H Bond Activation by Perovskite Solar Photocatalyst Cell.....	76
3.1 Introduction	78
3.2 Results.....	79
3.3 Conclusion.....	85
3.4 Experiment section	86
3.5 References	89
3.6 Supporting Information	94

Chapter 4 Direct Z-Scheme FAPbBr ₃ /Bi ₂ WO ₆ Heterojunction for Photoredox Reaction with Large Driving Force	109
4.1 Introduction	111
4.2 Results	113
4.3 Conclusion	122
4.4 Experiment section	123
4.5 References	127
4.6 Supporting information.....	130
Chapter 5 Summary and future direction	145
Safety Aspects.....	148
Publication list.....	149

Chapter 1

Introduction

Adapted from “Solar-Driven Metal Halide Perovskite Photocatalysis: Design, Stability, and Performance”

Haowei Huang, Bapi Pradhan, Johan Hofkens, Maarten B. J. Roeffaers*, Julian A. Steele*

The original article is licensed under the ACS EditorChoice license, and further permission requests should be directed to the ACS.

<https://pubs.acs.org/doi/10.1021/acsenergylett.0c00058>

Copyright © 2020 American Chemical Society

Contributions

H.H. collected all literature reports and wrote the most part, including 1.1 Overview, 1.3 MHPs photocatalysis and 1.4 Project aim; 1.2 Instability parameters of perovskite was written by B.P.; H.H., J.H., J.A.S. and M.B.J.R. together revised the manuscript with input from all the authors.

1.1 Overview

Like the natural and efficient energy conversion exhibited by photosynthesis, photocatalysis presents an effective way for man-made solar-to-chemical energy conversion.^{1,2} The first report of UV-driven photocatalytic hydrogen production on TiO₂ in 1972³ has motivated decades of scientific exploration and development, leading to several applications important for human society; from energy conversion (e.g. water splitting, CO₂ reduction) and chemical transformations, to the remediation of organic pollutants. Reactions driven by photocatalytic materials generally follow three separate processes: (i) absorption of photons to generate electron and hole pairs, (ii) charge separation and migration to reaction sites on the photocatalyst surface, and (iii) chemical oxidation and reduction at the surface mediated respectively by the photo-generated holes and electrons.⁴

An ideal photocatalytic material should embody several desirable physical traits; namely, broad and strong light absorption, efficient charge separation, long operational stability and the appropriate redox ability for target reactions.⁵ In reality, however, most photocatalysts are far from perfect. For example, pristine TiO₂, graphitic carbon nitride (g-C₃N₄), and BiVO₄ have their own shortcomings such as wide bandgap⁶, rapid recombination of photogenerated charge carriers⁷, and poor photo-reduction potential⁸, respectively. It follows that a strong desire to develop new semiconductor photocatalysts with suitable properties continues to motivate intense materials exploration and research within the field.

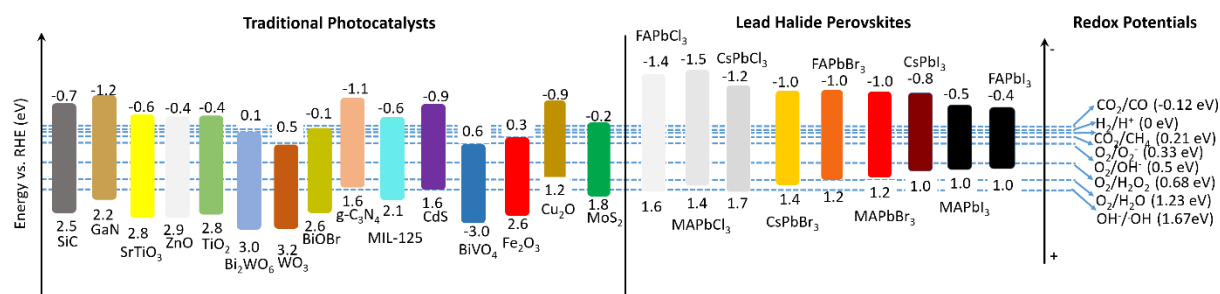


Figure 1-1. Band edge positions of conventional photocatalysts and different MHPs relative to reversible hydrogen electrode (RHE).⁶⁻¹⁶ For comparison the redox potential of some common half-reactions are also presented.¹⁷⁻²⁰

Metal halide perovskite (MHP) semiconductors have recently emerged as promising optoelectronic materials for applications spanning efficient solar cells and LEDs, to lasers and photodetector devices.²¹ MHPs are ionic crystals with the general chemical formula ABX_3 . Here A is a monovalent cation (MA: $CH_3NH_3^+$, FA: $CH(NH_2)_2^+$ and Cs^+), B represents a divalent metal cation [Pb^{2+} , Sn^{2+} or Cu^{2+}], and X is a halogen anion (Cl^- , Br^- or I^-).²² The successful application of MHPs within optoelectronic devices is driven mainly by their low production costs and easy solution processing²², tunable, direct bandgap^{23,24}, long carrier diffusion lengths,²⁵ high carrier mobility²⁶ and unusual tolerance to defects²⁷.

The schematic band structure of direct and indirect bandgap semiconductors are compared in Figure 1-2. In a direct bandgap semiconductor, the bottom of CB and the top of VB lie at the same value of the crystal momentum (k-vector) in the Brillouin zone. With light irradiation ($E_{\text{photon}} > E_g$), an electron-hole pair can produce easily in direct bandgap semiconductor, as the material does not undergo a change in momentum; note that photons only carry energy and almost non-existing amount of momentum. For an indirect bandgap semiconductor, the maximum energy of the VB and the minimum in the CB are not coinciding in crystal momentum space. This means that the generation of an electron-hole pair is only possible if simultaneous to photon absorption the material undergoes a significant change in its momentum through mediation of phonons. However, this also implies that the recombination process is also more efficient for a direct band gap semiconductor than for an indirect band gap semiconductor, where the process must be mediated by a phonon. Surprisingly, MHPs as direct semiconductor, still presents long carrier diffusion lengths. Snaith *et al.* found that the diffusion length is more than 1 micrometer in the mixed halide perovskite $CH_3NH_3PbI_{3-x}Cl_x$. Sargent *et al.* reported that adding a Lewis base to reduce the trap density in perovskite, the electron-diffusion length can reach 2.3 μm . This value is larger than those in traditional photocatalysts, such as 1 μm in C_3N_4 , 2-4 nm in Fe_2O_3 . On the other hand, MHPs exhibit higher carrier mobility compared to traditional photocatalysts. As reported by Snaith *et al.*, for $MAPbI_3$ polycrystalline perovskite films, the mobility can reach $\sim 2 \text{ cm}^2/\text{V/s}$, which is much higher than $10^{-5} \sim 10^{-4} \text{ cm}^2/\text{V/s}$ in TiO_2 . Compared to more traditional photocatalysts, MHPs exhibit relatively narrow bandgap energies as shown in Figure 1-1, enabling the absorption of lower-energy solar photons.

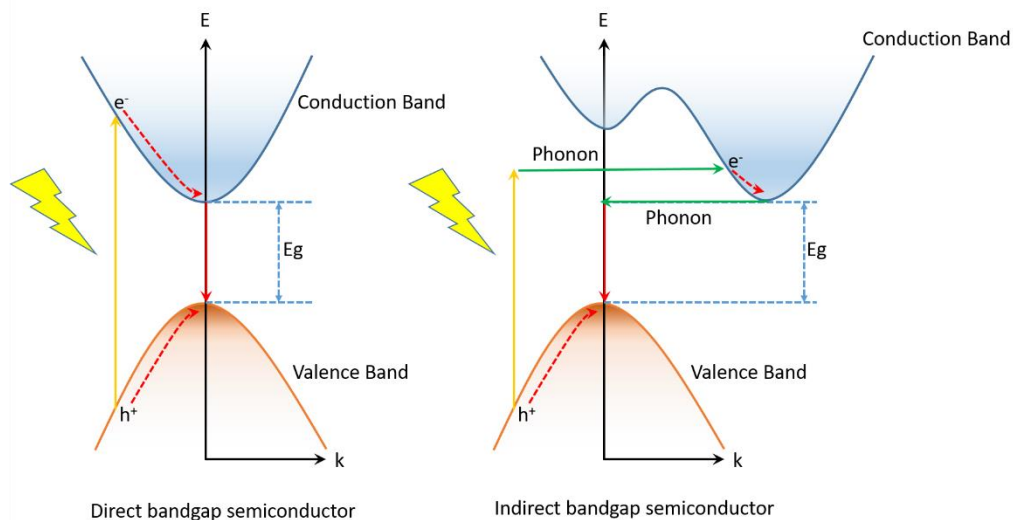


Figure 1-2. Schematic difference between the band structure of direct(left) and indirect(right) bandgap semiconductors in the energy-momentum space.

Based on the reaction thermodynamics, a suitable match is required between the electronic band structure of a semiconductor and reaction redox potential. The potentials of typical photocatalytic half-reaction involved in water splitting, CO₂ reduction, aerobic organic transformation and dye degradation are shown in Figure 1-1.²⁰ Here, the relative position of the MHP conduction band (CB) and valence band (VB) are depicted alongside these redox potentials. Based on their comparison, Figure 1-1 highlights the excellent reduction ability of MHPs, i.e. the relative position of their CB is typically negative enough for H₂ generation, CO₂ reduction, aerobic oxidation and degradation of organic compound (via superoxide radical). Additionally, some members of the MHP family (namely the Cl-based materials and all-inorganic CsPbBr₃) can in theory also achieve water oxidation, due to their relatively positive valence band maximum (VBM). For hydroxyl radical formation, which is often involved in dye degradation, the required potential is above the VBM of MHPs, making them an unsuitable candidate. However, hydroxyl radical formation can also occur via reduction of oxygen to superoxide followed by protonation steps which provide an alternative way to generate hydroxyl radical on MHPs.

Considering the (photo)physical properties exhibited by MHPs, they seemingly satisfy several of the important requirements for good photocatalytic reactions as shown in Figure 1-1. Indeed, the first report of MHP-based photocatalysis appeared as recently as December 2016, where Nam and co-workers²⁸ outlined a strategy for photocatalytic-driven HI splitting using MAPbI₃, exploiting the dynamic equilibrium

of the dissolution and reprecipitation of MAPbI₃ in saturated HI aqueous solutions. This particular approach proved effective, as the ionic lattice of MHPs is highly unstable under more typical photocatalytic reaction conditions. For example, H₂O splitting, CO₂ and N₂ reduction, and dye degradation, all require water or a polar solvent, which facilitate degradation pathways detrimental for long-term use (Figure 1-3).^{29,30} Furthermore, for some radical-based reactions, like dye degradation, water or polar solvents are prerequisite for the formation of the radical species that drive the reaction forward. Within this context, it is the relatively reactive and unstable nature of ionic MHP crystals which have thus far limited their application as a photocatalyst. In this review, the current prospects of effectively applying MHPs in photocatalysis are discussed. We provide a critical analysis of the instability issues hampering progress in this new branch of scientific research, and highlight proved strategies allowing for stable reaction environments. Finally, a brief perspective on the future challenges and possibilities of this promising new technology is provided.

1.2 Instability parameters of perovskite

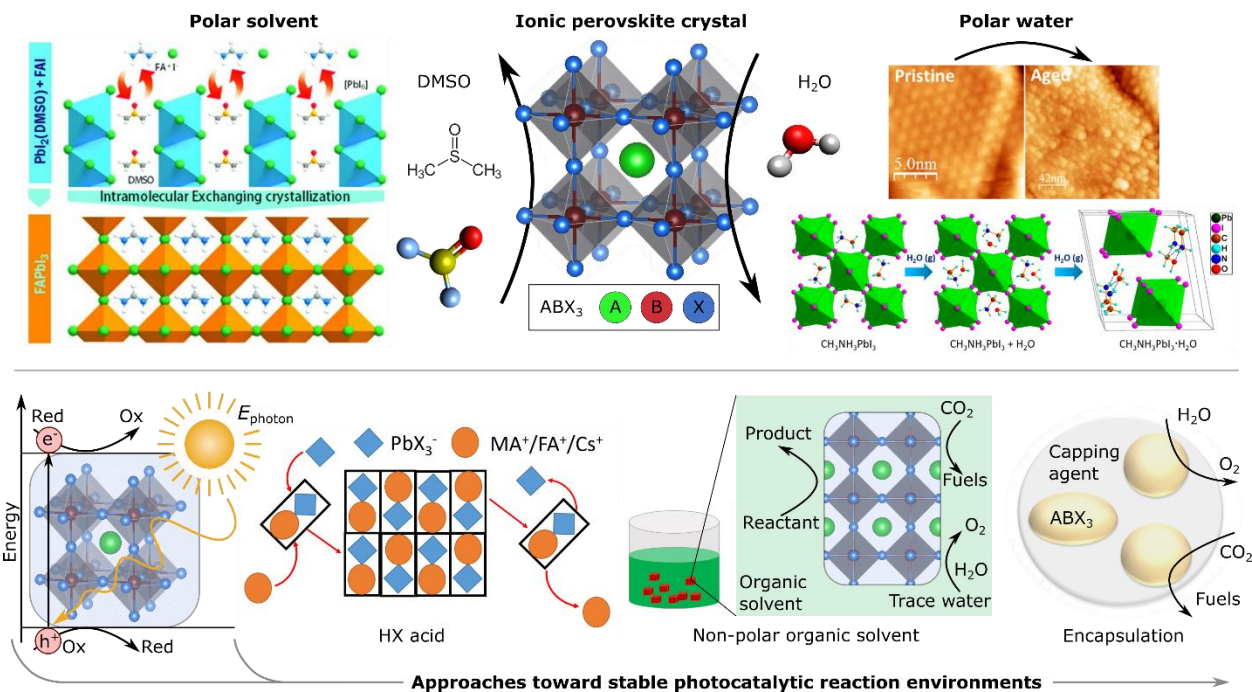


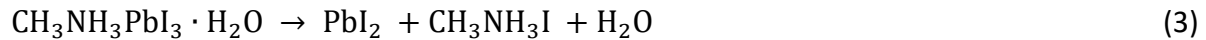
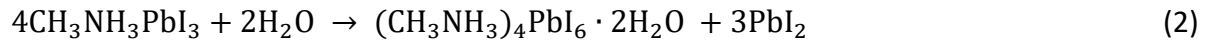
Figure 1-3. Top: Illustration of the vulnerability of MHP surfaces during photocatalytic reactions, when exposed to polar solvents (e.g. DMSO) and water.³¹⁻³³ Polar molecules undergo rapid intramolecular exchange with the organic cation, causing the immediate degradation of the

perovskite chemical structure. Water molecules degrade MHPs in a stepwise fashion, where initially a monohydrate perovskite structure is formed which later decomposes into nonperovskite structures, through different intermediates. Bottom: Three main routes toward creating stable reactions environments when employing MHPs as a photocatalyst: saturated haloacid solutions stabilize MHPs by establishing a dynamic ionic equilibrium between the dissolved ionic species and the solid perovskites; non-polar or relatively low polarity solvent dispersion reduces the degradation pathways; and encapsulation via capping agents or shelling prevents direct contact with polar solvents or reaction products.

The structural and optoelectronic properties of MHPs change significantly upon phase transitions, thermal stress, ambient air exposure (oxygen, moisture) and illumination (UV light). The ionic interactions binding the charged components of MHP crystals render them vulnerable to structural modifications at its surface when coming into contact with polar additives. This particular feature within MHPs defines the limited scope of photocatalytic reactions for which these semiconductors have been effectively applied. As shown in Figure 1-3, MHPs tend to decompose relatively quickly into a PbX_2 ($X=I, Br, Cl$) precipitate, $Cs^+/MA^+/FA^+$ cations and halide anion when exposed to polar molecules. Thermogravimetry results show that in comparison to all-inorganic perovskites (e.g. $CsPbI_3$), organic-inorganic hybrid perovskites present a faster degradation at low-temperature as the amine group in MA^+ cation is volatile. Due to the volatile nature, the degradation product will disappear thus lowering its concentration. Based on Le Chatelier principle, the reaction equilibrium will thus shift to reduce this changing concentration, hence driving the further perovskite degradation. Also, considering the super hygroscopic nature of MAI and FAI, the crystal structure of hybrid perovskites can be rapidly destroyed with moisture.³⁴ Also in Figure 1-3, water interacts with the crystal via hydrogen bonding to hydrate the surface, yielding a polycrystalline non-perovskite structural coating and grain boundaries³³.

The quantitative and systematic investigation of humidity-induced structural and chemical degradation mechanism of $MAPbI_3$ has been performed by ultrafast transient absorption spectroscopy and kinetics studies,³⁵ *in situ* grazing incidence X-ray diffraction³⁶ and via *ab initio*

molecular dynamics simulations³⁷. The absorbed water molecules easily penetrate the MHPs structure and form intermediate monohydrate and dihydrate structures by reacting with the $[\text{PbX}_6]^{4-}$ octahedral units.³² This is followed by rapid material breakdown through hydrolysis (Equation 1-4):^{30, 35-37}



The hydrogen bond between the organic and inorganic units is one of the key features in stabilizing the perovskite structure and is compromised through this process; water forms two new types of hydrogen bonds, a strong one with the lattice halides and another one weakly with the organic cations.^{30,40,41} Notably, the interaction between MA and H_2O is not established until the monohydrate phase transition, where the two become locked.³² In polycrystalline thin films, the monohydrate phase formation occurs independently of the film thickness due to the rapid transport of water molecules across grain boundaries.³² Even in bulk MAPbI_3 single crystals, aging under ambient conditions shows prominent surface restructuring with the formation of grain boundaries.³³ This is a direct consequence of the surface undergoing rapid hydration upon exposure to moisture, relative to the shielded interior. Furthermore, light absorption in MHPs initiates a halide-to-metal charge transfer process which reduces the charge density at the X sites, thereby weakening the $\text{CH}_3\text{NH}_3 \cdots \text{X}$ hydrogen bonding interactions and causing an increased rate of degradation upon illumination under a humid atmosphere.⁴²

As shown in Figure 1-3, when MHPs are exposed to polar solvents like dimethyl sulfoxide (DMSO), the perovskite structure also degrades to form coordination compounds, such as $\text{PbI}_2(\text{DMSO})_2$,

MAI-PbI₂-DMSO via van der Waals interactions.^{43,44} Rapid intramolecular exchange between DMSO and FAI in FAPbI₃ causes immediate decomposition of the perovskite structure. Solution-processed perovskite thin-films possess much more prominent defects when they are fabricated from a polar coordinating solvent (e.g. DMF, DMSO, γ -butyrolactone, acetonitrile), relative to the noncoordinating polar solvents.⁴⁵ This arises from the tendency of coordinating solvents to get intercalated more easily during the perovskite film formation.

The photostability of MHPs in presence of ambient oxygen (O₂) is also low. Reports have shown that iodide-based perovskites (i.e. MAPbI₃) break down under simulated solar irradiation (AM 1.5G) and O₂ exposure.^{46,47} This process is mediated by the rapid generation of iodide vacancies upon photoexcitation, which offers a pathway for oxygen to be introduced into the MHPs crystal lattice. Molecular oxygen reacts with photo-generated electrons at the iodide vacancy sites, producing reactive superoxide species which subsequently reacts with MA cation, resulting in water, methane gas, and lead iodide as the decomposition products.^{47,48} At the same time, illumination can affect the ion distribution in MHPs. With the light irradiation, electrons and holes will be generated in MHPs. At surfaces and grain boundaries of MHPs, there are larger densities of electronic traps. A large number of photogenerated electrons will be trapped near the surface and creating electric fields that induce directional ion migration.

The lattice of MHP semiconductors is increasingly being considered as soft in nature, due to the occurrence of several structural and chemical dynamic effects. Ultimately, the soft nature exhibited by MHP crystals renders their surfaces prone to structural modification and degradation as discussed above. The replacement of A site organic cations with inorganic Cs⁺ – resulting in the formation of an all-inorganic chemical structure – substantially increases resistance to humidity and photostability.^{49,50} The ionization energy Cs compared to MA can explain the higher chemical stability of the all-inorganic perovskites.⁵¹ For example, CsPbBr₃ nanocrystals are found to be substantially more stable in polar solvents, e.g. isopropyl alcohol, ethyl acetate, methyl acetate, acetonitrile, which is encouraging for a vast number of photo-redox catalysis reactions.⁵²

1.3 MHPs photocatalysis

The instability issues outlined above have motivated the development of several approaches aimed toward realizing stable photocatalytic environments, which have been summarized at the bottom of Figure 1-3: (i) placing MHPs in saturated halo acid solutions for solar-driven water splitting,^{28,53-61} (ii) minimizing direct contact with highly polar environments via targeted low polarity solvents and solutions,⁶²⁻⁸⁰ and (iii) encapsulating MHP nanocrystals to screen them from polar molecules.⁸¹⁻⁹⁵ Efforts are also being made toward realizing MHPs which are intrinsically stabilized against exposure to polar solvents. Currently, some all-inorganic MHPs have proven to be stable in polar solvents.⁹⁶⁻¹⁰² In what follows we outline the current state of play for each of these approaches, highlighting their successes and pitfalls, and features which ultimately govern their realistic potential.

1.3.1 Halogen acid solution for photocatalytic hydrogen evolution

Because MHPs are water-soluble ionic compounds, utilizing the precipitation-solubility equilibrium between the perovskite phase and the soluble ionic species is a creative approach to solve the stability problem. Nam *et al.*²⁸ first introduced the photocatalytic H₂ production in MAPbI₃ saturated hydrogen iodide (HI) acid aqueous solution using MAPbI₃ perovskite polycrystalline powders. As shown in Figure 1-4A and 1-4B, in a saturated HI solution, micron-sized MAPbI₃ particles dissolve to form methylammonium cations and PbI_x complex anions, with an equal amount of MAPbI₃ particles recrystallizing in parallel. The MAPbI₃ phase would be largely modulated by the I⁻ and H⁺ ions concentrations in the aqueous solution. In a relatively high ion concentration regime (>3.16 mol/l HI solution), together with a lower iodide concentration (i.e. [I⁻] ≤ [H⁺], whereby HClO₄ is added), the MAPbI₃ perovskite phase remained stable. Figure 1-4C presents the reaction mechanism for photocatalytic HI splitting on MAPbI₃. Upon irradiating with visible light ($\lambda \geq 475$ nm), these mixtures produced roughly 26 $\mu\text{mol H}_2$ in 9 h using MAPbI₃ as a photocatalyst, with the photo-generated holes driving the I⁻ to I₃⁻ oxidation.

In addition, as a good reducing agent of I_3^- to I^- , H_3PO_2 was added to maintain the I^- concentration. Due to the dynamic equilibrium between the $MAPbI_3$ powders and the ionic species in the saturated solution, $MAPbI_3$ remained stable for 160 h under continuous irradiation, without any compromise to the activity as shown in Figure 1-4D. Furthermore, the deposition of Pt on the $MAPbI_3$ (i.e. Pt/ $MAPbI_3$) increased the hydrogen evolution rate to $57 \mu\text{mol/g/h}$, resulting in a solar-to-chemical conversion efficiency (the ratio of solar light converted to chemical energy) of 0.81%. In Pt/ $MAPbI_3$ sample, as the $MAPbI_3$ particles dissolve and re-precipitate, the change in contact between $MAPbI_3$ and Pt is unclear.

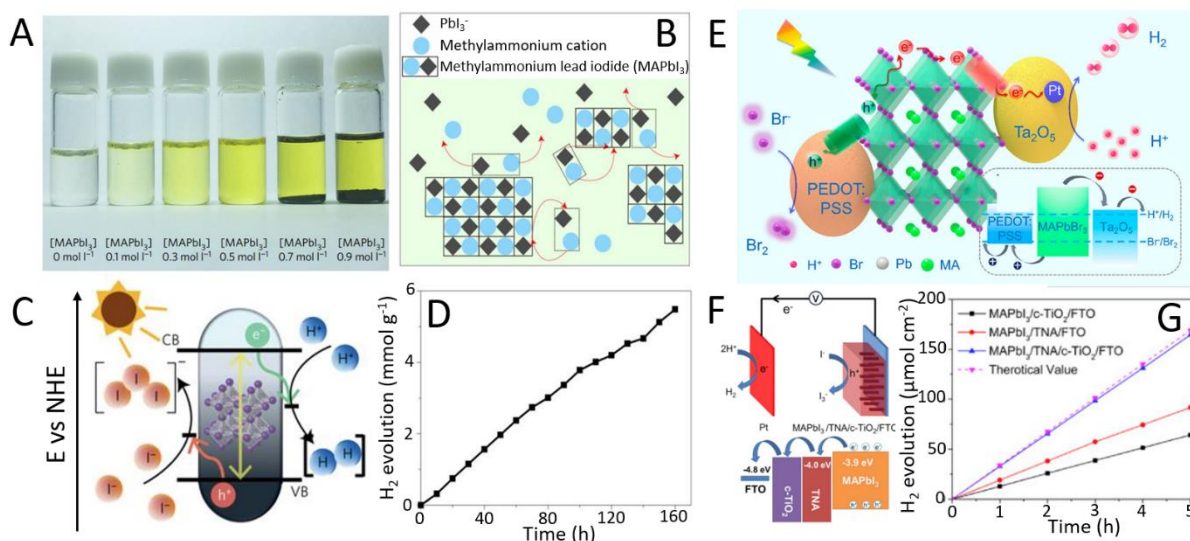


Figure 1-4. (A) $MAPbI_3$ in aqueous HI solutions at different concentrations, (B) scheme representing the equilibrium between $MAPbI_3$ dissolution and recrystallization in a saturated HI solution, (C) band diagram of the $MAPbI_3$ powder for the HI splitting photocatalytic reaction and (D) stable photocatalytic H_2 evolution in the saturated solution for 160 h.²⁸ (E) The reaction mechanism for $MAPbBr_3$ with Pt/ Ta_2O_5 and PEDOT:PSS as the electron- and hole-transporting motifs, respectively, for photocatalytic HBr splitting reaction, and the corresponding energy level diagrams of $MAPbBr_3$, Ta_2O_5 , and PEDOT:PSS.⁵⁶ (F) The scheme of charge transfer in photoelectrochemical HI splitting cell of $MAPbI_3/TNA(c-TiO_2)/FTC$ (FTC doped SnO) photoelectrode as the band alignment, and (G) the H_2 evolution on this cell for 5 h.⁵⁸

In a similar fashion, Li *et al.*⁵⁷ improved the photocatalytic activity of Pt/MAPbI₃ by inserting TiO₂ in between Pt and MAPbI₃. The Pt/TiO₂-MAPbI₃ photocatalyst powders, based on micron-sized MAPbI₃, displayed a nearly 90-fold enhancement for H₂ generation (ca. 7.3 mmol/g/h,) from aqueous HI solution compared to the parent Pt/MAPbI₃ (ca. 830 μmol/g/h) system. The introduction of TiO₂ not only improved the extraction of electrons from MAPbI₃ via suitable band alignment, but also acted to stabilize the Pt cocatalyst. The approach of Huang *et al.*⁵³ was similar, in that they modified MAPbI₃ bulk micro-crystals with reduced graphene oxide (rGO) to efficiently extract electrons from the MAPbI₃ light absorber, as well as provide H₂ release sites. The combined MAPbI₃/rGO system exhibited an H₂ evolution rate of 939 μmol/g/h, which is 67 times larger than that of pure MAPbI₃. After 200 h of irradiation, the composite material remained stable and did not display decreased photocatalytic activity.⁵³ Zhao *et al.* also used rGO to extract the photogenerated electrons, this time from a lead-free “double perovskite” (A₂B^IB^{III}X₆ architecture) Cs₂AgBiBr₆ bulk photocatalyst. In saturated HBr and H₃PO₂ solution, a 48.9 μmol/g/h H₂ release rate was achieved on Cs₂AgBiBr₆/rGO composite with visible light irradiation, which is 80 times higher than that of pure Cs₂AgBiBr₆.⁶¹ Chen *et al.* similarly modified MAPbI₃ bulk microcrystals for photocatalytic applications, though with black phosphorus (BP).⁵⁹ The BP/MAPbI₃ system offered an impressive H₂ evolution rate of 3472 μmol/h/g in HI solution. Widening the fundamental bandgap with bromine atoms at the halide sites, Li *et al.* demonstrated that MAPbBr₃ bulk microcrystals can be used for steady photocatalytic H₂ production in saturated MAPbBr₃ aqueous HBr solution upon visible light irradiation.⁵⁶ Their perovskite semiconductors were further modified with PEDOT:PSS (poly(3,4-ethylenedioxythiophene) polystyrene sulfonate) and Ta₂O₅ as co-catalysts, preparing PEDOT:PSS/MAPbBr₃/Ta₂O₅. As described in Figure 1-4E, due to band alignment of PEDOT:PSS and Ta₂O₅ with MAPbBr₃, these additives acted as hole and electron transporting layers, respectively, for efficient photogenerated charge separation. Notably, in comparison to the pure MAPbBr₃, ca. 52 times enhancement on the hydrogen evolution rate was achieved with the hybrid material, and an apparent quantum efficiency (AQE = N_{electron}/N_{photon}) of ca. 16.4% was reported for 420 nm excitation. However, the photocatalytic activity of this hybrid material decreased gradually within a 4 h time experiment. The instability of this system comes from the

agglomeration of PEDOT:PSS in the reaction solution, thus affecting the interfacial charge transfer between MAPbBr₃ and PEDOT:PSS. Finding a more suitable hole transport material to replace PEDOT:PSS could give rise to high efficiency and stable photocatalytic production of H₂.

Huang et al. doped iodide into hybrid MAPbBr₃ and all-inorganic CsPbBr₃ bulk microcrystals (i.e., MAPbBr_{3-x}I_x⁵⁴ and CsPbBr_{3-x}I_x⁵⁵) to form bandgap funnel structures via the graded distribution of iodide. In saturated HBr/HI mixed acid solution, both the MAPbBr_{3-x}I_x/Pt and CsPbBr_{3-x}I_x/Pt photocatalysts exhibited decent H₂ evolution under visible light irradiation, reaching 2604.8 μmol/g/h and 1120 μmol/g/h, respectively. Furthermore, both samples displayed a high stability during the 50 h of testing. A similar strategy was followed for lead-free perovskite MA₃Bi₂I₉ with a lamellar structure, as the system reaches a precipitation-solubility equilibrium in saturated HI solution.⁶⁰ The photocatalytic rate for H₂ evolution on Pt/MA₃Bi₂I₉, with Pt as co-catalyst, is nearly 170 μmol/g/h in saturated HI solution. After 70 h of cycling, no decrease in H₂ evolution rate was observed for this catalyst.

Photocatalyst	Solution	Light source	Activity (μmol/g/h)	Measured time for stability(h)	Ref
MAPbI ₃	HI solution	visible light ($\lambda \geq 475$ nm)	33	160	28
Pt/TiO ₂ -MAPbI ₃	HI solution	visible light ($\lambda \geq 420$ nm), 200 mW/cm ²	7300	12	57
MAPbI ₃ /rGO	HI solution	visible light ($\lambda \geq 420$ nm), 300 W	939	200	53
Cs ₂ AgBiBr ₆	HBr solution	visible light ($\lambda \geq 420$ nm), 300 W	48.9	120	61

Black Phosphorus/MAPbI ₃	HI solution	visible light ($\lambda \geq 420$ nm), 300 mW/cm ²	3472	200	59
PEDOT:PSS/MAPbBr ₃ /Ta ₂ O ₅	HBr solution	visible light ($\lambda \geq 420$ nm), 150 mW/cm ²	650	4	56
MAPbBr _{3-x} I _x /Pt	HBr/HI mix solution	visible light ($\lambda \geq 420$ nm), 300 W	2604.8	50	54
CsPbBr _{3-x} I _x /Pt	HBr/HI mix solution	visible light ($\lambda \geq 420$ nm), 300 W	1120	50	55
MA ₃ Bi ₂ I ₉ /Pt	HI solution	visible light ($\lambda \geq 400$ nm), 300 W	170	70	60

Table 1-1. Summary of reported photocatalytic hydrogen generation activity from haloacid (HX) solution using MHP-based systems.

The band engineering strategy for MHPs stabilized within a halogen acid solution was further developed by Liu et al., with the photocatalyst being deployed in a solar-driven photoelectrochemical (PEC) cell for H₂ evolution in Figure 1-4F.⁵⁸ The cell consisted of a MAPbI₃-TiO₂ nanorod array (TNA) as the photoanode, achieving efficient and stable H₂ evolution in HI solution (57 wt % HI aqueous solution saturated with MAPbI₃ powder). The amount of evolved H₂ on different PEC cells at 0.14 V vs. Ag/AgCl are shown in Figure 1-4G, in comparison to MAPbI₃/c-TiO₂/FTO and MAPbI₃/TNA/FTO, MAPbI₃/TNA/c-TiO₂/FTO PEC cell exhibits the highest hydrogen evolution rate of 33.3 $\mu\text{mol}/\text{cm}^2/\text{h}$ under solar illumination and this during 5 h of experiment.

As summarized in Table 1, these promising examples demonstrate that saturated aqueous halogen acid solutions offer a suitable reaction medium for MHP-based photocatalytic hydrogen

evolution. Due to the precipitation-solubility equilibrium, MHPs remains stable in the saturated solution, and additional HX acid can circumvent PbX_2 precipitation and suppresses the formation of the hydrated MHP phase. Analogous to the approach taken within the field of photovoltaic solar cells, introducing heterogeneous interfaces (or even compositional grading within the MHP) can tune the energetics of the photocatalyst system, for greatly improved charge separation and reaction activity. However, within the HX acid solution X^- acts as a sacrificial agent and the oxidation of X^- to X_3^- takes priority over H_2O oxidation. Thus, additional reducing agents such as H_3PO_2 need to be consumed to reduce X_3^- back to X^- , however, this ultimately limits the added value of this reaction.¹⁰³ Furthermore, the strong acidity of HX will prevent the selection of certain co-catalysts which are unstable in such environments.

1.3.2 Apolar and low-polar solvent stabilization

The ionic nature of MHPs makes them especially sensitive to degradation by polar molecules, hence low polarity solvents can be employed to create stable photocatalytic reaction conditions. Under such environmental conditions, the relatively weak dipole moment of the solvent does not readily coordinate with the MHP crystal, to dissociate them into complexes of the composing ionic species. This strategy was utilized by both Kuang *et al.*⁶² and Sun *et al.*⁷¹, employing all-inorganic $CsPbBr_3$ quantum dots (QDs) for photocatalytic CO_2 reduction; note that due in contrast to the micron-sized crystals utilized in haloacids this approach also works for MHP nanocrystals and QDs. In Sun's paper, the low polarity solvent used was ethyl acetate mixed with trace amounts of water as hole scavengers (volume ratio: 300:1), see Figure 1-5A.⁷¹ Within 8 h of simulated solar light irradiation, 34, 12 and 0.8 $\mu\text{mol/g}$ of respectively CO , CH_4 and H_2 were generated; note that water acts as hole scavenger thus generated oxygen, but it also water splitting into hydrogen is competing with the CO_2 reduction reaction. The reaction processes can be summarized as (Equation 5-8):





The CsPbBr₃ QDs displayed a good structural stability under these conditions and maintained its surface morphology and crystalline structure during the reaction.⁷¹ In Kuang's work, with 12 h of constant illumination 49.5, 22.9, 1.07 μmol/g of CO, CH₄ and H₂ are produced on the CsPbBr₃ QDs.⁵⁹ To further boost the performance, as depicted in Figure 1-5B, the CsPbBr₃ QDs were modified by the addition of graphene oxide (GO) which is capable of efficient electron extraction and transport.⁶² The generated CsPbBr₃/GO composite had a ca. 25% enhanced electron consumption rate (357.4 μmol/g) in comparison to pristine CsPbBr₃ material (284.7 μmol/g) as is shown in the Figure 1-5C. In this latter example, pure ethyl acetate without addition of water was used as reaction medium. The nature of the hole scavenger in this system is unclear.

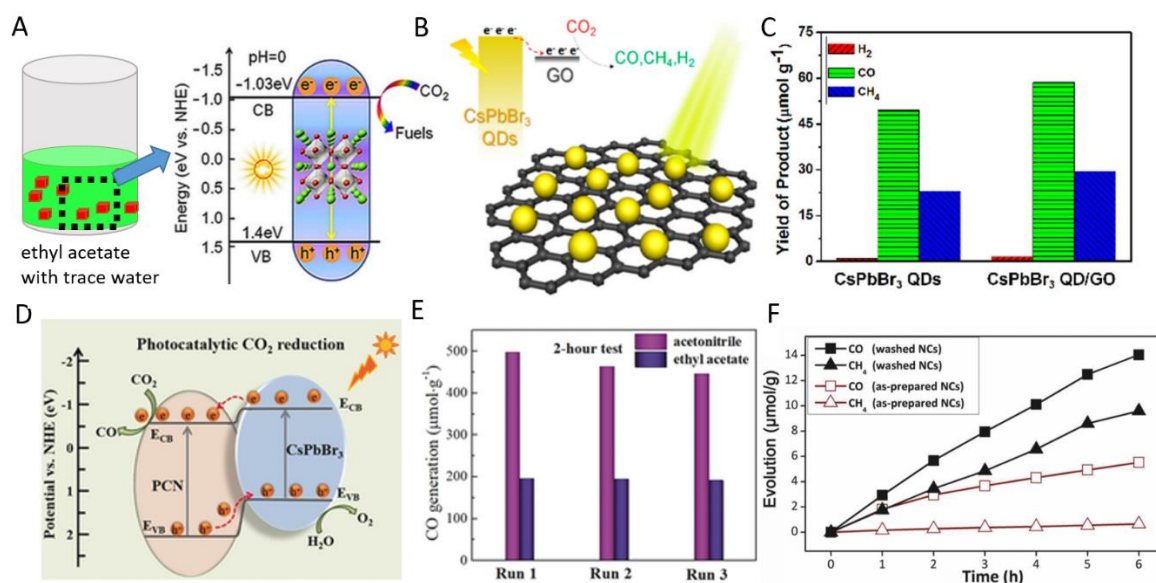


Figure 1-5. (A) CsPbBr₃ for the photocatalytic CO₂ reduction in a 300/1 ethyl acetate/water mixture.⁷¹ (B) the scheme of the CsPbBr₃ with graphene oxide for photocatalysis CO₂ reduction

in ethyl acetate and (C) the yield of products in this reaction system.⁶² (D) band alignment of the composite photocatalyst CsPbBr₃ QDs/g-C₃N₄ for photocatalytic CO₂ reduction in acetonitrile and ethyl acetate, and (E) the CO generation for three consecutive runs of 2 h each in acetonitrile/water and ethyl acetate/water systems on this composite.⁶⁹ (F) Time course of CO and CH₄ evolutions via CO₂ reduction by Cs₂AgBiBr₆ NCs in ethyl acetate;⁷²

This concept was expanded in the work of Xu *et al.*, where CsPbBr₃ QDs/graphitic carbon nitride (g-C₃N₄) composites were engineered for efficient CO₂ photo-reduction. It was found that the presence of g-C₃N₄ improves the electron extraction via type-II bandgap alignment and the chemical bond formed between MHPs and g-C₃N₄, as shown in Figure 1-5D. In this work both acetonitrile and ethyl acetate solvents with trace amounts of water (volume ratio: 300:1) were employed, yielding CO with the formation rates of 148.9 μmol/g/h and 70 μmol/g/h, respectively.⁶⁹ Furthermore, Figure 1-5E presents that with 3 successive cycles of catalysis (6 h in total), only 10.3% and 2.4% activity was lost in the acetonitrile/water and ethyl acetate/water system, respectively. The enhanced stability can be attributed to the surface passivation of CsPbBr₃ by g-C₃N₄ - through the interaction between the amino group on the edges of heptazine in g-C₃N₄ and Br⁻ in CsPbBr₃ QDs. Building on this work, Zhang *et al.* coupled CsPbBr₃ to g-C₃N₄ containing titanium-oxide species, to prepare CsPbBr₃/TiO-g-C₃N₄, which exhibits improved activity on CO₂ reduction in an ethyl acetate/water system, in comparison to CsPbBr₃/g-C₃N₄. Here titanium-oxide species helped to speed up the charge separation and acted as reaction sites to improve the surface reaction.⁷⁵ In a similar fashion, the good charge conductivity of two-dimensional layered Ti₃C₂T_x (T_x: fluorine, oxygen, and hydroxyl groups) MXene material was exploited by Liu *et al.* to accelerate the photogenerated charge separation in CsPbBr₃ nanoparticles. The MXene-MHP photocatalyst yielded CO and CH₄ production rates of 32.15 and 14.64 μmol/g/h, respectively, in pure ethyl acetate solution.⁷³

Partial bromide substitute by chloride in CsPbBr₃ to form CsPbBr_{3-x}Cl_x QDs was used by Su *et al.* to generate MHPs with improved stability for the CO₂ reduction.⁷⁰ The increased Cl content however reduces the visible light response. This shows the need for finding a balance between

stability and activity/photoresponse within a chosen MHP photocatalyst through well-informed materials engineering.

Moving away from Pb-based MHPs to lead-free perovskites, Kuang *et al.* showed CO₂ reduction over Cs₂AgBiBr₆ NCs under solar illumination in pure ethyl acetate.⁷² The stable evolution of CO and CH₄ on Cs₂AgBiBr₆ NCs under simulated solar light irradiation are shown in Figure 1-5F. After 6 h of irradiation, 5.5 and 0.65 μmol/g of CO and CH₄ are generated on Cs₂AgBiBr₆, respectively, with no H₂ side product detected.

Photocatalysts	Solution	Light source	Products and Activities (μmol/g/h)	Measured time for stability(h)	Ref
CsPbBr ₃ QDs	Ethyl acetate/water	300 W Xe lamp, AM 1.5G filter	CO(4.25), CH ₄ (1.5), H ₂ (0.1)	8	71
CsPbBr ₃ QDs/GO	Ethyl acetate	300 W Xe lamp, AM 1.5G filter, 150 mW/cm ²	CO(4.89), CH ₄ (2.47), H ₂ (0.13)	12	62
CsPbBr ₃ QDs/g-C ₃ N ₄	Ethyl acetate/water	300 W Xe lamp 420 nm cut-off filter	CO(70)	6	69
	Acetonitrile/water		CO (148.9)		

CsPbBr ₃ /TiO-g-C ₃ N ₄	Ethyl acetate/water	300 W Xe lamp, 400 nm cut-off filter, 100 mW/cm ²	CO(12.9)	10	75
CsPbBr ₃ /MXene	Ethyl acetate	300 W Xe lamp 420 nm cut-off filter	CO(32.15), CH ₄ (14.64)	12	73
CsPbBr _{3-x} Cl _x QDs	Ethyl acetate	300 W Xe lamp, AM 1.5 filter, 200 mW/cm ²	CO(85), CH ₄ (12)	8	70
Cs ₂ AgBiBr ₆	Ethyl acetate	300 W Xe lamp, AM 1.5G filter, 150 mW/cm ²	CO(0.92), CH ₄ (0.11)	6	72
CsPbBr ₃ @TiO ₂	Ethyl acetate/isopropanol	300 W Xe lamp, AM 1.5G filter, 150 mW/cm ²	CO(3.9), CH ₄ (6.72), H ₂ (1.46)	30	81
MAPbI ₃ @Fe-MOF	Ethyl acetate/water	300 W Xe lamp, 400 nm cut-off filter, 100 mW/cm ²	CO(4.16), CH ₄ (13)	80	83

Co ₂ %@CsPbBr ₃ /Cs ₄ PbBr ₆	Water	300 W Xe lamp, 400 nm cut-off filter, 100 mW/cm ²	CO(11.95)	20	92
CsPbBr ₃ @ZIF-67	Water vapor	100 W Xe lamp, AM 1.5G filter, 150 mW/cm ²	CO(0.77), CH ₄ (3.51)	18	84
CsPbBr ₃ NC/ZnO nanowire/macroporous graphene	Water vapor	A 150 W Xe lamp, AM 1.5G and 420 nm cut-off filter 150 mW/cm ²	CO(0.85), CH ₄ (6.29)	16	96
Cs ₂ SnI ₆ /SnS ₂	Water and methanol vapor	150mW/cm ² visible light, 400 nm long pass filter	CH ₄ (6.09)	9	97
Cs ₃ Bi ₂ I ₉	Water vapor	UV lamp, 80.38 μW/cm ²	CO(7.76), CH ₄ (1.49)	10	98

Table 1-2. Summary of the reported photocatalytic CO₂ reduction performance of MHPs under various illumination conditions.

CO₂ reduction in low polarity solvents with/without trace amounts of water as electron donor expands the potential application of MHP photocatalysts, as summarized in Table 2. In most reports, MHPs still face a poor product selectivity as CO and CH₄ are typically generated

simultaneously, and additionally water splitting generating H₂ is competing for the generated photoelectrons while the holes are scavenged by water forming O₂. Nonetheless, employing a largely apolar environment, even with the inclusion of trace amounts of targeted polar molecules, is a promising route towards long term activity and stability.

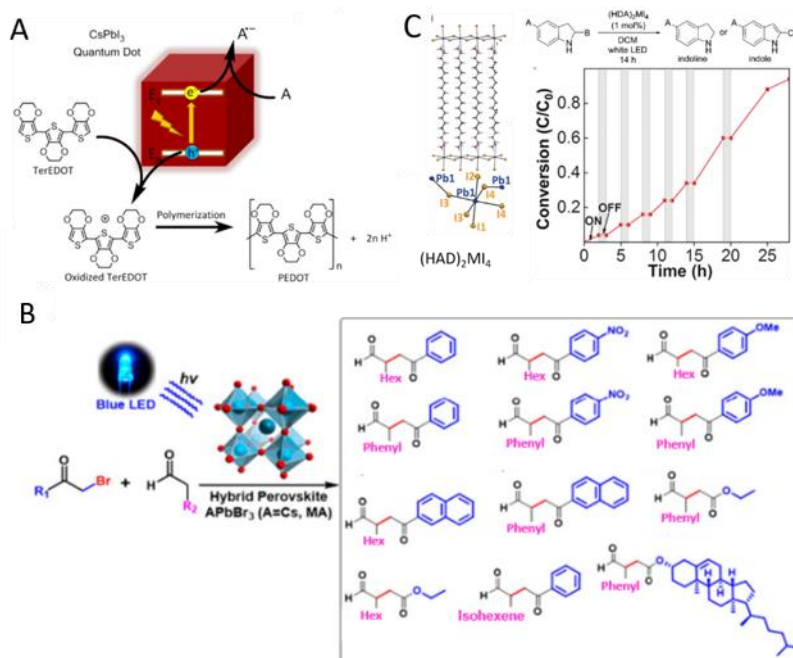


Figure 1-6. (A) Photocatalytic polymerization of TerEDOT by CsPbI₃ QDs under visible light illumination.⁶⁷ (B) Photocatalytic α -alkylation of aldehydes by Cs/MAPbBr₃ in organic solvents.⁶⁶ (C) Crystal structures and photocatalytic activity of 2D (HDA)₂MI₄ (M=Pb, Sn) for indoline-2-carboxylic acid decarboxylation in 25 h.⁸⁰

Next to the photoreduction of CO₂ for the generation of solar fuels, recent efforts have focused on organic transformations within low polarity solvents for solar-driven MHPs photocatalysis. As shown in Figure 1-6A, Tüysüz *et. al.* found that CsPbI₃ QDs can promote the polymerization of 2,2',5',2''-ter-3,4-ethylenedioxythiophene (TerEDOT) to poly(3,4-ethylenedioxythiophene) (PEDOT) in dry toluene under visible light illumination.⁶⁷ In fact, the generated PEDOT further stabilizes the cubic perovskite phase of CsPbI₃ QDs by encapsulating the perovskites and shielding

it from the environment. Very recently, Tüysüz *et al.* confined Cs₃Bi₂Br₉ nanoparticles (2-5 nm) inside large ordered channels of mesoporous silica SAB-15 and used this composite for aliphatic and aromatic C-H bond activation, to develop corresponding aldehydes and ketones.⁷⁸ This study demonstrates that well-dispersed MHP nanoparticles offer a better electron-hole separation and an improved contact with reaction substrates.

Besides the selective oxidation of organics to value-added products in toluene, the complete mineralization of organics to CO₂ and H₂O using MHP photocatalysts has also been investigated. Huang *et al.* synthesized CsPb(Br_{1-x}Cl_x)₃-Au NCs for the Sudan Red III degradation in toluene.⁷⁶ When the CsPb(Br_{1-x}Cl_x)₃-Au NCs system is photo-excited, there is an inner electron field between Au and the perovskite enhancing the charge separation. The dissolved O₂ can be trapped by the photoelectrons on CsPb(Br_{1-x}Cl_x)₃ to produce superoxide anion radicals ([•]O₂⁻), and Au NCs can act as hole reservoirs to enhance hydroxyl radical generation on its surface.⁷⁶ After that, Sudan Red III reacts with these two kinds of radicals to generate non-toxic products. Upon visible light irradiation, 71% Sudan Red III was degraded by CsPb(Br_{1-x}Cl_x)₃-Au within 6 h, which is 3 times higher than the CsPb(Br_{1-x}Cl_x)₃ case (ca. 20% of Sudan Red III degradation). Here, the role of Au NCs is in contrast to the widely employed non-plasma Au-nanoparticle decorated photocatalysts,^{104,105} where Au extracts electrons from the semiconductors and acts both as an electron reservoir and a reduction site to generate hydroxide radical.

Beyond photocatalytic organic transformations in toluene, other low polarity solvents like dichloromethane (DCM), tetrahydrofuran (THF), dioxane, and hexane have been used for MHP-based photocatalytic organic transformations. Wu *et al.*⁶⁸ achieved S-H bond activation using CsPbX₃ (where X=Cl, Br, and I) NCs in DCM. Interestingly, this work also realized C-H activation by evaluating phosphorylation of N-aryl tetrahydroisoquinoline derivatives in both toluene and THF solvent. As seen in Figure 1-6B, Yan *et al.* demonstrated that MAPbBr₃ and CsPbBr₃ nanocrystals could selectively form C-C bond in α -alkylation of aldehydes in DCM, THF and dioxane, via photocatalysis.⁶⁶ A large turnover number (TON) of over 52,000 is achieved in the perovskite-based photocatalytic α -alkylation of aldehydes, under visible light illumination. This large TON is

encouraging for this particular application, and can potentially provide a path toward the commercialization of perovskite photocatalysis in the future. Follow up work by Yan and co-workers showed that not only C-C bond formation, but also a series of organic transformation, C-O and C-N bond-formation, can be achieved on the CsPbBr₃ photocatalyst.⁶⁵ In ethyl acetate, CsPbBr₃ can achieve C-N bond formations via direct N-heterocyclizations forming pyrazoles and pyrroles, upon irradiating with blue light. With a Ni co-catalyst, C-O bond formation via aryl-esterification was realized on CsPbBr₃ in THF, upon irradiating with blue light. In addition, CsPbBr₃ QDs can drive the MBT (2-mercaptobenzothiazole) oxidation in hexane by photocatalysis and photoelectrocatalysis.⁷⁴ Recently, Gualdrón-Reyes and co-workers prepared CsPbBr₃/I_{3-x} nanoparticles via both hot injection (H-I-CsPbBr₃/I_{3-x}) and anion exchange (A-E-CsPbBr₃/I_{3-x}) methods, to investigate the influential role of the surface chemical states in the photo-oxidation of β-naphthol in hexane.⁷⁷ The two different preparation methods arrived at CsPbBr₃/I_{3-x} nanoparticles with different iodide vacancy (V_I) concentrations on the surface, with a larger V_I population found in A-E-CsPbBr₃/I_{3-x}. As a result, A-E-CsPbBr₃/I_{3-x} formed superoxide radicals, •O₂⁻, species involved in the photodegradation of organic compounds. The V_I sites were found to provide key surface chemical states to produce •O₂⁻. On the other hand, the VB is shifted to more negative values and the bandgap is narrowed in H-I-CsPbBr₃/I_{3-x} by increasing the iodide content.

In Figure 1-6C, Soo *et al.* synthesized 2D Pb and Sn halide perovskite microcrystals with the long-chain alkyl group 1-hexadecylammonium (HDA): (HDA)₂PbI₄ and (HDA)₂SnI₄.⁸⁰ These MHPs exhibited photocatalytic activity in decarboxylation and dehydrogenation of indoline-2-carboxylic acids in DCM. Figure 1-6D presents the stable performance of these materials during a 25 h “on-off” irradiation study. However, if the two Pb- and Sn-based perovskites are compared, the Sn-based structures exhibit inferior stability due to the self-oxidation of Sn²⁺ to Sn⁴⁺.

This collection of recently reported results using MHPs as photocatalyst in low polarity solvents demonstrate their potential in a wide range of photocatalytic reactions; including CO₂ reduction, selective organic transformations for value-added products, organic pollutant degradation. The reduced polarity of the created environment results in a relatively low solubility for MHPs which

preserves the original structure rather than relying on a precipitation-solubility equilibrium as was discussed for aqueous conditions. Under these conditions, MHP nanoparticles and QDs can be used to drive photocatalytic reactions rather than micron-sized MHPs in water further optimizing the accessible surface area.

1.3.3 Encapsulation and core-shell structure

A straightforward stabilization method consists of encapsulating the MHP by a protective layer inside core-shell particles. The protective layer prevents direct contact between the MHP and destabilizing polar molecules. Care should be taken that the shell material does not block the light from reaching the MHP. Kuang and co-workers used amorphous TiO_2 as the encapsulating material to generate $\text{CsPbBr}_3@ \text{TiO}_2$ core-shell structures.⁸¹ Figure 1-7A shows the TEM picture of this core-shell structure that CsPbBr_3 nanocrystal was capped by amorphous TiO_2 . This photocatalyst was used for CO_2 reduction in ethyl acetate/water under solar light irradiation, exhibiting better activity than bare CsPbBr_3 due to improved electron transfer from CsPbBr_3 to TiO_2 . Most importantly, this core-shell structure shows impressive stability improvement, retaining over 90% of its initial photocatalytic activity after 15 h of use. Even after 30 h of constant simulated solar light illumination, the encapsulated material still possessed comparable photocatalytic activity, as shown in Figure 1-7B. Recently, Wu *et al.* covered CsPbBr_3 microparticles with porous graphitic carbon nitride (p-g- C_3N_4) and used it for malachite green degradation in polar isopropanol. This catalyst exhibited a stable activity during ten cycles (~4.7 h in total), as p-g- C_3N_4 acted to protect the CsPbBr_3 surface.⁹⁴ The core-shell structure was also shown to help stabilize the MHP not only in low polarity solvents, but also in a high polarity solvent like water.

Zheng *et al.* also prepared anatase coated CsPbBr_3 nanoparticles for photocatalytic applications, Figure 1-7C displays a TEM micrograph of the core-shell system.⁸² The tight TiO_2 shell was prepared via a two steps process, which starts from a simple wet chemical hydrolysis of titanium butoxide in relative humidity (RH) of 30%, to form TiO_x layer at the outside of CsPbBr_3 NCs at 25

°C. Next, a 300 °C heating step promotes the formation of the tight TiO₂ (a-TiO₂). Compared to pristine CsPbBr₃ NCs, the core/shell CsPbBr₃/a-TiO₂ NCs present a higher photocurrent and a smaller resistance in 0.1 M Na₂SO₄ aqueous solution due to the formation of type II band alignment in the CsPbBr₃/a-TiO₂ core/shell heterostructure. On the other hand, the CsPbBr₃/a-TiO₂ composite was relatively stable and was able to be stored in water for more than 12 weeks in the dark without leading to any phase change or chemical decomposition. Furthermore, within 8 h of irradiation, as shown in Figure 1-7D, the photocurrent of core/shell NCs does not show any reduction, indicating excellent PEC (photoelectric chemistry) stability in water. A protective layer on the outside of MHPs, especially tight crystallized shell, could decrease the direct contact from the polar solvent which indeed enhance the stability of MHPs photocatalyst.

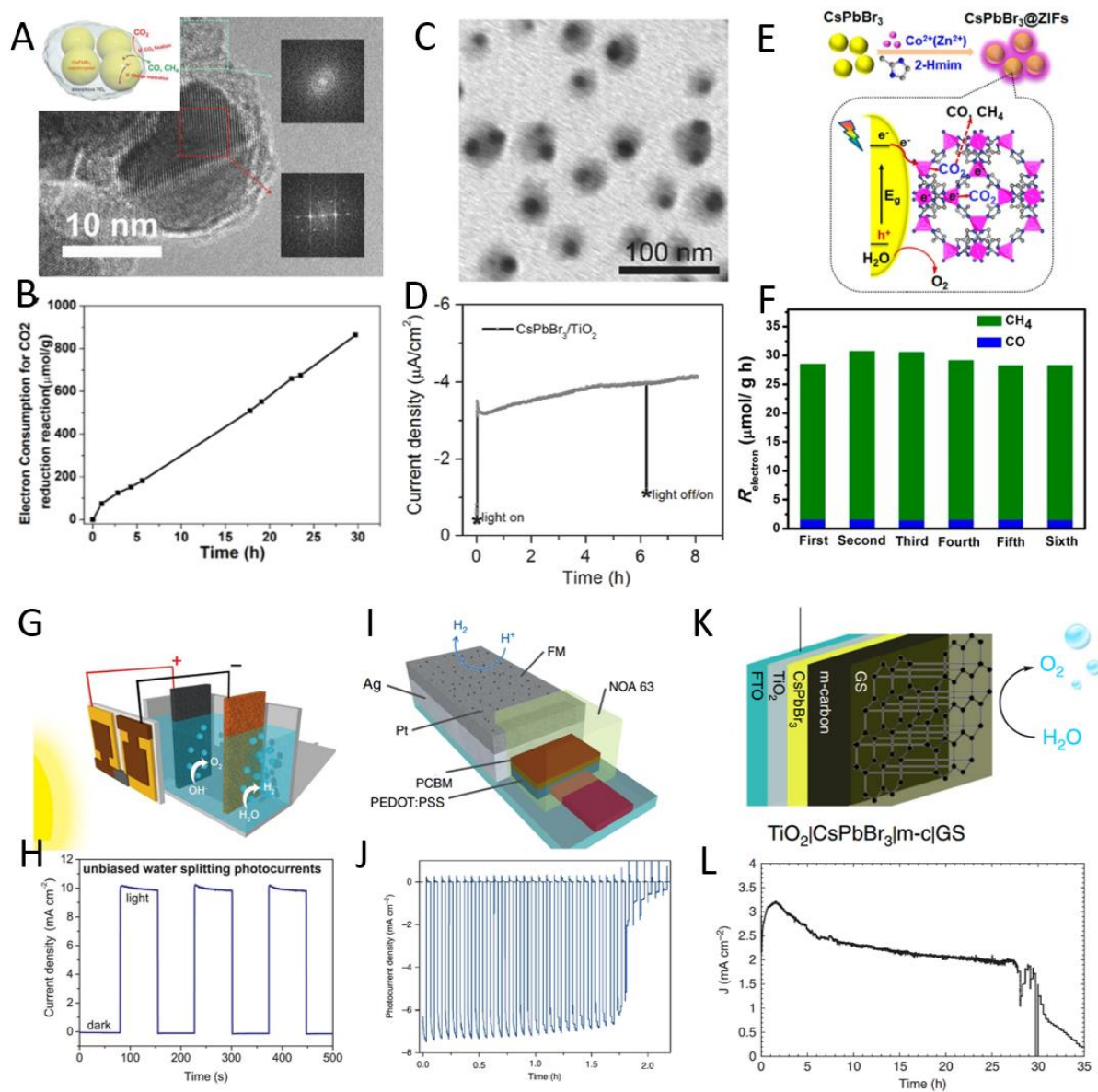


Figure 1-7. (A) TEM images of amorphous TiO₂-encapsulated CsPbBr₃ nanocrystal and (B) time course of photocatalytic CO₂ reduction in ethyl acetate with isopropanol traces upon solar light irradiation.⁸¹ (C) TEM image of anatase TiO₂-coated CsPbBr₃/TiO₂ core/shell NCs and (D) controlled potential electrolysis of the CsPbBr₃/TiO₂ NCs electrode in neutral water within 8 h.⁸² (E) Schematic of CsPbBr₃@ZIF-67 formation and the charge transfer in this material and (F) its application for CO₂ photo-reduction in ethyl acetate solution.⁸⁴ (G) Perovskite water-splitting

solar cell and (H) current density–time curve of the device without external bias under solar light illumination.⁹⁰ (I) Structure diagram of FTO/PEDOT:PSS/perovskite/PCBM/PEIE:Ag photocathode for water reduction and (J) the photocathode stability test by light-chopped chronoamperometry.⁹¹ (K) Schematic diagram of TiO₂|CsPbBr₃|m-c|GS photoanode, and (L) its long-term stability of TiO₂|CsPbBr₃|m-c|GS70 for water oxidation with solar light irradiation.⁹⁴

On the other hand, encapsulation is not merely limited to the synthesis of individual core-shell photocatalyst structures, as shown in Figures 6A and C. The small size of MHP QDs allows trapping porous structures such as metal-organic frameworks (MOF). CsPbBr₃ QDs trapped in the ZIF-type MOFs (ZIF-67, ZIF-8) showed a steady CO₂ photoreduction in an ethyl acetate and water mixture.⁸⁴ Figure 1-7E presents a schematic of the synthesized CsPbBr₃@ZIF hybrids by directly growing ZIF around CsPbBr₃ QDs. The catalytic stability of CsPbBr₃@ZIF was also tested by recycling photocatalytic reaction. After cycling 6 times (18 h in total), no obvious decay was obtained in Figure 1-7F, indicating the good protective function of the ZIF shell. Very recently, Lu et al. incorporated iodide-based perovskite MAPbI₃ into Fe-MOF, which exhibited an impressive activity on CO₂ reduction in an ethyl acetate/water solution (over 80 h: CO, 4.16 μmol/g/h; CH₄, 13 μmol/g/h).⁸³ Ghosh et. al. incorporated a Br-based perovskite into the ZIF-8 pore structure to prepare a composite photocatalyst, MA(OA)PbBr₃@ZIF-8 (OA is n-octylammonium).⁸⁶ OA, a long alkyl chain ammonium cation, was used as a capping ligand to stabilize the MHP nanoparticles and control the crystallization process for the formation of colloidal NPs inside MOF.⁸⁶ This material presents outstanding chemical stability under a variety of conditions which would normally be detrimental for the MHPs, such as water immersion, UV light irradiation and high temperature (100 and 140 °C) heating. Furthermore, they exhibit promising activity and stability towards photocatalytic organic dye (methyl orange) degradation in water.⁸⁶ Although the photo-generated holes found in the VB of MA(OA)PbBr₃ cannot directly oxidize H₂O, the electrons in the CB will react with O₂ to generate superoxide radicals ([•]O₂⁻) which react with H₂O to produce the hydroxyl radicals.

Alternatively, adding hydrophobic ligands to coat the NC surface is another effective method toward creating a waterproof “shell” on the MHP crystal exterior. Lu *et al.* adopted this approach with their CsPbBr₃/Cs₄PbBr₆ nanocrystals and used the highly hydrophobic ligand hexafluorobutyl methacrylate.⁹² The resultant MHP-based system possessed an outstanding tolerance to H₂O; after 100 h of storage in water, 90 % of the PL intensity of this MHP component was retained. Further doping the photocatalyst with Co (generating Co_{2%}@CsPbBr₃/Cs₄PbBr₆) allowed for a CO yield of roughly 240 μmol/g in 20 h via CO₂ reduction, in pure water. Similarly, larger hydrophobic organic spacer cations (A-site cation, such as 2-phenylethylammonium (PEA) or n-butylammonium (n-BA)) have been used to form lower-dimensional 2D or quasi-2D layer perovskites.¹⁰⁶ The addition of these A-site cations have been found to benefit the overall material stability in polar environments, by acting as a protecting layer against moisture attack. These improvements to stability have been widely demonstrated for MHP-based solar cells and LEDs and offer a promising direction toward developing more stable MHP photocatalysts in future.

Coating MHPs with hole and electron transport layers (HTL and ETL, respectively) and electrodes in PEC devices also prevents direct contact with polar solvents, providing another effective route toward long term stabilization. Currently, there are two different directions for this particular approach: 1) implementing a MHP solar cell-electrode (photoelectrode) system, with the MHP PV separated completely from the electrode and electrolyte; 2) MHP photoelectrode, with the MHP integrated into an electrode. Grätzel and co-workers were the first to construct a MHP-based solar cell-electrode (photoelectrode) system, for the application of water splitting in an alkaline electrolyte. Here, they combined a perovskite tandem solar cell and a bifunctional NiFe layered double hydroxide (i.e. origin of both water oxidation and reduction), with the perovskite placed out of the solution to keep it stable, as shown in Figure 1-7G.⁹⁰ Under solar light irradiation, this device offered relatively impressive water splitting performance; Figure 1-7H shows the “on-off” current density–time curve of the device without external bias for water splitting in that the unbiased water splitting current reached 10 mA/cm², which corresponds to a 12.3% solar-to-hydrogen efficiency. Kamat *et. al.* and Mathews *et. al.* proposed MHP-based solar

cell ensembles with BiVO_4 and Fe_2O_3 photoanodes, respectively, for the same water-splitting reactions.^{87,89} Using these photoanodes, single-junction MAPbI_3 solar cell can achieve water splitting, as holes in these photoanodes can mediate water oxidation. Specifically, the BiVO_4 - MAPbI_3 and Fe_2O_3 - MAPbI_3 exhibited solar-to-hydrogen conversion efficiencies of 2.5% and 2.4% at neutral pH, respectively.

Meanwhile, some researchers appropriately integrated MHPs into the electrode to prepare a MHP photoelectrode for the PEC reaction. In 2015, Zheng et. al. reported the first MAPbI_3 -photoelectrode for water splitting.⁸⁸ In this work, a Ni layer was coated onto MAPbI_3 both as a physical passivation barrier and as a hole transport layer. However, after 15-20 min of continuous tests, the photocurrent of this photoelectrode experienced a sharp decrease. Reisner *et al.* further adopted a solar cell-like structure to develop a metal-encapsulated perovskite photocathode - $\text{FTO/PEDOT:PSS/MAPbI}_3/\text{PCBM}([6,6]\text{-phenyl-C}_{61}\text{-butyric acid methyl ester})/\text{PEIE}(\text{ethoxylated polyethylenimine})\text{:Ag}$ - for PEC hydrogen evolution in an aqueous medium.⁹¹ As shown in Figure 1I, the perovskite solar cell provide the photocathode and two additional protective layers, composed of Ag and an eutectic alloy (InBiSn), were deposited to fully cover the solar cell. These two protective layers not only form a water-resistant metal-encapsulated photocathode and protect the perovskite, but also transfer the photogenerated electrons to the surface to react with water. This photocathode can be stored in water for 6 h without any decomposition. Furthermore, as shown in Figure 1-7J, the photocathode retained more than 80% of the initial photocurrent after continuous illumination for 1.5 h. Recently, Poli *et al.* used graphite sheets (GS) as a protective layer to create a $\text{TiO}_2/\text{CsPbBr}_3/\text{carbon/GS}$ photoanode, as shown in Figure 1-7K. A 25- μm -thick deposit of GS offers a more compact seal, to stop water from reaching the perovskite. Furthermore, GS is superhydrophobic, which also enhances the water-resistance of this photoanode. Under solar illumination, the system emitted stable for 30 h in the aqueous electrolyte with above 2 mA/cm^2 photocurrent at 1.23 V_{RHE} .⁹⁴

In 2019, Reisner *et al.* expanded the reaction scope when using MHP-photoelectrodes, for CO_2 reduction. They integrated a MHP-photoelectrode with BiVO_4 photoanode to prepare a tandem

device for syngas production.⁹³ Under bias-free operation, this tandem device, which consists of BiVO₄, FAMA_{0.22}Cs_{0.07}Pb_{1.32}I_{3.27}Br_{0.66}, and cobalt catalyst on carbon nanotubes (CoMTPP@CNT), offers the production rates of H₂ and CO of 0.58 ± 0.33 and 0.18 ± 0.16 μmol/cm²/h in CO₂ saturated water, respectively. In this tandem device, FAMA_{0.22}Cs_{0.07}Pb_{1.32}I_{3.27}Br_{0.66} and BiVO₄ harvest solar light to generate carriers, with holes remaining in the BiVO₄ for water oxidation and electrons moving to CoMTPP@CNT for CO₂ and H₂O reduction. The selectivity of products on CoMTPP@CNT can be controlled by the pH of the electrolyte; more H₂ was found to be released in acidic solutions, relatively low production was observed in alkaline conditions, and neutral pH favoured more CO₂ reduction. Furthermore, in comparison to a single component photocatalyst, such as a MAPbBr₃, a mixed compound FAMA_{0.22}Cs_{0.07}Pb_{1.32}I_{3.27}Br_{0.66} system presents a better efficiency and stability.¹⁰⁷

Overall, based on the discussion above, MHP film systems achieve “steady” PEC energy conversion in aqueous conditions via several methods, including MHP solar cells coupled with an electrocatalyst and photoelectrocatalyst, and protective layers fully covering to form a MHP photoelectrode. In these systems, MHP, as a harvester of light to absorb solar light and generate carriers, was isolated from the aqueous solution. As a result, the stability of MHP which be effectively improved. These PEC systems offer an efficient method for the utilization of solar energy by halide perovskites in aqueous solutions.

1.3.4 Polar solvent stabilization of MHPs

The approaches outlined above, while offering varying degrees of success under rather regimented conditions, fail to offer a path toward widespread adoption. As has been highlighted throughout, this failure stems from the instability of MHPs when exposed to inherently reactive environments. Clearly, developing MHPs which can intrinsically endure common photocatalytic conditions, and importantly display long term photocatalytic performance, represents an ideal scenario. In comparison to hybrid organic-inorganic perovskites, all-inorganic perovskites are more stable due to their higher formation energy, lower configurational entropy, non-volatile

and lower hygroscopic nature.¹⁰⁹ Owing to the elimination of weakly-bonded organic components in the crystal structure, all-inorganic perovskites exhibit relatively higher resilience against environmental triggers. Recently, some all-inorganic perovskites have been used with success for reactions employing water vapor. Kuang et al. prepared CsPbBr₃ NC/MRGO (macroporous graphene oxide) composite, though further modified the system by adding hierarchical branched ZnO nanowires (BZNW), generating CsPbBr₃/BZNW/MRGO composite, for photocatalytic CO₂ reduction in the presence of water vapor. Compared to both pristine CsPbBr₃ NCs and CsPbBr₃/MRGO, the addition of the ZnO nanowires enhanced the photoelectron consumption rate to > 50 μmol/g/h⁹⁶. Furthermore, during 4 cycles or 16 h of simulated solar illumination the CH₄ generation remained steady without any apparent decrease. Then, Kuang et al. also explored the stability of lead-free MHP photocatalyst when exposed to polar molecules. With methyl alcohol and water vapor a lead-free Cs₂SnI₆ perovskite nanocrystal combined with SnS₂ nanosheets achieved the CO₂ to CH₄ (6.09 μmol/g/h) reduction. This hybrid system provided a stable photocatalytic activity over 3 successful reaction cycles (9 h in total).⁹⁷ Similarly, Diao et al. prepared Rb₃Bi₂I₉, Cs₃Bi₂I₉, MA₃Bi₂I₉ with an ultrasonication top-down method, arriving at materials which can remain stable for 7 days under 70 % humidity.⁹⁸ These perovskites were then used for CO₂ photo-reduction with water vapor. As shown in Figure 1-8A, CO₂ and H₂O can be adsorbed on the perovskite surface and form different intermediate species, including dioxycarbon anion bridge carbonate, monodentate carbonate, and bidentate carbonate. The time-dependent evolution of CH₄ on these perovskites under light irradiation is shown in Figure 1-8B, in which the production of CH₄ increases steadily in 10 h. More surprisingly, in 2018, Navas *et al.* prepared CsSnBr₃ microparticles for photocatalytic dye degradation in water solution.⁹⁹ As the CsSnBr₃ VB (1.9 eV vs. RHE) is more positive than the redox potential of OH⁻/[•]OH,¹⁰⁸ the generated hydroxyl radicals degraded the violet dye as shown in Figure 1-8C. Meanwhile, as shown in Figure 1-8D, within 5 cycles (15 h in total) in 2.0 mg/L crystal violet dye aqueous solution, there was no compromise in the photo-activity.

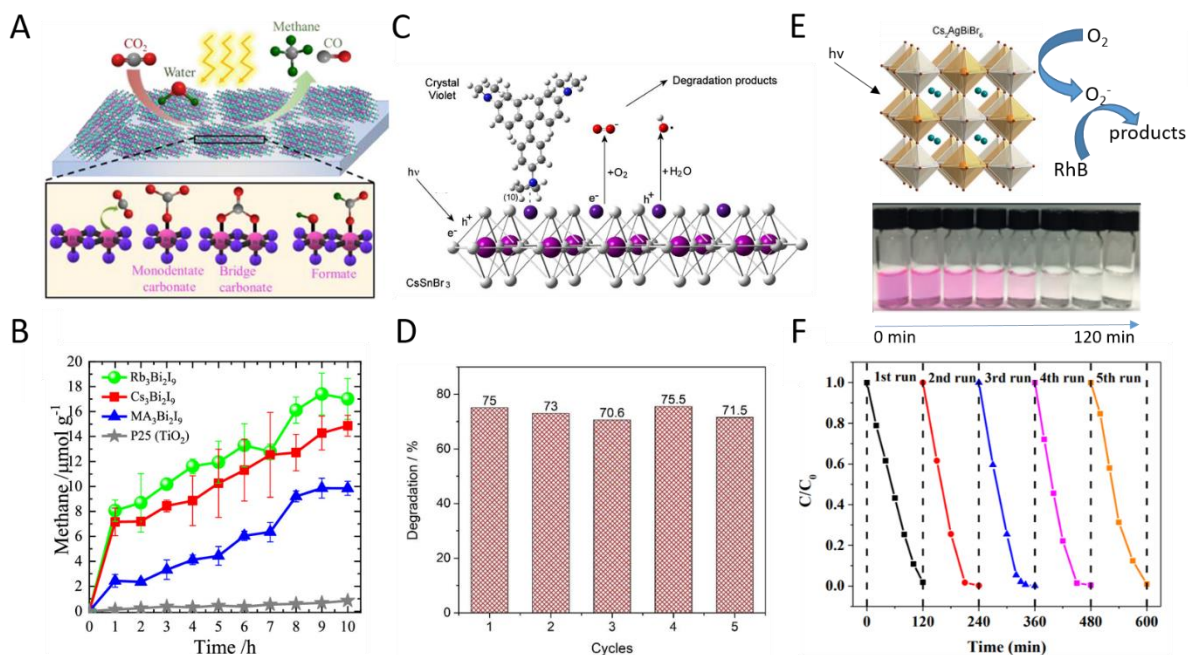


Figure 1-8. (A) Scheme of CO₂ photoreduction with water vapor on Bi-based perovskite photocatalysts and (B) the CH₄ generation during 10 h.⁹⁸ (C) Scheme of the photodegradation of Crystal violet on CsSnBr₃ and (D) stability test for the photodegradation of Crystal violet in 5 cycles.⁹⁹ (E) Scheme of the photodegradation of RhB on the Cs₂AgBiBr₆ and photographs of RhB at different irradiation times, and (F) recycling test of photocatalytic RhB degradation upon visible-light irradiation.¹⁰⁰

On the other hand, researchers have also explored all-inorganic MHP photocatalysts for steady operation in alcohols. For example, Fan *et al.* prepared CsPbBr₃ nanoparticles for tetracycline hydrochloride (TC-HCl, antibiotic) degradation in ethanol.¹⁰² Upon visible light irradiation, 76% TC-HCl could be degraded in 30 min. Within 4 cycles of experiments of in total 120 min, CsPbBr₃ still maintained nearly 90% of its initial activity. The partial activity loss can be attributed to the loss of photocatalyst material during recovery between consecutive cycles. Relying on the relatively higher chemical robustness of Cs₂AgBiBr₆, Xu *et al.* demonstrated microparticles of this material suitable for photocatalytic reaction in ethanol.¹⁰⁰ In Figure 1-8E, with Upon continuous irradiation, ca. ~98% Rhodamine B (RhB) was degraded by Cs₂AgBiBr₆ photocatalyst within 2 h. In

this reaction, the efficient production of superoxide radicals provides the dominant species involved in RhB degradation. As shown in Figure 1-8F, the material maintained its photo-activity and comparable stability in ethanol following 6 h of irradiation (5 cycles), although a little bit of AgBr was generated as water molecules might lead to partial dissolution of the Cs₂AgBiBr₆ crystal. Similarly, Tüysüz *et al.* synthesized lead-free perovskite Cs₃Bi₂Br₉ submicron/nanoparticles and used them for the ring-opening reaction of epoxides in isopropanol.¹⁰¹ In Cs₃Bi₂Br₉, Lewis acid Bi sites adsorbed and activated epoxides. Upon light irradiation, holes and electrons generated in Cs₃Bi₂Br₉ reacted with alcohols and O₂ to form alcohol radicals and superoxide radicals, respectively. Alcohol radicals and alcohol anions generated by the reaction between superoxide radicals and alcohols would serve as nucleophiles to react with activated epoxides. Upon visible light irradiation, 99 % styrene oxide was converted by Cs₃Bi₂Br₉ after 6 h irradiation. Furthermore, with 3 cycles (18 h in total), Cs₃Bi₂Br₉ still exhibited a decent activity (retaining 80% of its initial photocatalytic activity).

The high humidity tolerance of all-inorganic MHPs makes them ideal materials for the photocatalytic CO₂ reduction in the presence of high polarity solvent vapors. Furthermore, the photodegradation of organic pollutants has proved that some all-inorganic MHPs remain stable in high polarity conditions. These discussed results open opportunities to apply these materials to perform chemical conversions involving polar solvents or molecules, even water splitting without the need of haloacids, biomass reforming and N₂ reduction.

1.4 Project aim

In this chapter we have examined the recent progress made in the field of MHP-based photocatalysis, focusing on the instability issues currently holding it back. To overcome material instability, several “stable” MHP-based photocatalytic systems have been designed and realized; including H₂ generation from saturated halo acid solutions; CO₂ reduction and organic synthesis in low- and non-polarity solvents; encapsulation and capping of MHPs for CO₂ reduction and photoelectrochemical water splitting; and dye degradation of MHPs in suitable polar solvents.

Prospects to intrinsically improve the crystal stability by designing novel composite perovskites have also been demonstrated. On the basis of the current knowledge and material limitations, this thesis will describe some promising results on MHPs photocatalytic organic reactions, benzyl alcohol oxidation and C(sp³)-H activation. Several promising paths toward future improving the MHP-based photocatalysis can be identified: Single type II heterojunction structure, solar cell structure with two type II heterojunctions and a Z-scheme structure.

To be more specific, in Chapter 2, we report the use of FAPbBr₃ as photocatalysts for benzylic alcohols oxidation in a non-polar toluene solution. In this study, pure FAPbBr₃ micro/nanocrystals were first proven to be efficient photocatalysts under solar excitation; within 8 h of irradiation, FAPbBr₃ bulk microcrystals exhibited a conversion rate of roughly 15% with near 100% selectivity (0.1 mmol benzyl alcohol in 2.5 mL toluene, 10 mg catalyst). More importantly, after 5 reaction cycles (40 h in total) the FAPbBr₃ photocatalyst displayed no decrease in activity. Again, the activity of the MHP photocatalyst can be improved by selecting a suitable co-catalyst and re-engineering the band structure of the system. For instance, modifying FAPbBr₃ into a FAPbBr₃/TiO₂ hybrid nanomaterial by *in-situ* anti-solvent growth realized the highest conversion rate of benzyl alcohol when optimized (ca. 63% conversion, with 15 wt % FAPbBr₃ in FAPbBr₃/TiO₂ composite), being 4 times higher than the pristine MHP case.

The direct functionalization of saturated C-H bonds to form high value-added chemicals is another challenging topic in modern chemistry. In chapter 3, we use FAPbBr₃ bulk microcrystals to photo-activate the C(sp³)-H bond in aromatic hydrocarbons and to form the corresponding alcohols and aldehydes. Similar to tailoring the energetics within solar cells, the addition of an electron transfer layer (TiO₂) and hole transfer layer (NiO_x) allows for optimizing the conversion efficiency of the MHP photocatalyst, by improving charge separation properties. This TiO₂/FAPbBr₃/NiO_x achieved C(sp³)-H bond activation in toluene with high selectivity and high conversion rates of benzaldehyde generation from toluene.

By efficient charge separation and transportation, MHPs-based type II heterojunction photocatalyst present a higher activity in organic synthesis in comparison to pristine FAPbBr₃. However, those hetero-structures would further compromise on the redox ability of MHPs. In Chapter 4, we develop a perovskite-based direct Z scheme photocatalyst, FAPbBr₃/Bi₂WO₆, with a strong redox ability. The physical chemistry details of this hetero-structure and the photophysical pathways of photoexcited carriers are revealed via a combination of complementary techniques. In this chapter, we also develop a new organic reaction, benzyl alcohol oxidation coupled with CO₂ reduction. CO and benzaldehyde as main products are generated with high efficiency and near 100% selectively on this Z scheme catalyst.

1.5 References

- (1) Kim, D.; Sakimoto, K. K.; Hong, D.; Yang, P. Artificial Photosynthesis for Sustainable Fuel and Chemical Production. *Angew. Chem. Int. Ed.* **2015**, *54*, 3259-3266.
- (2) Kamat, P. V. Meeting the Clean Energy Demand: Nanostructure Architectures for Solar Energy Conversion. *J. Phys. Chem. C* **2007**, *111*, 2834-2860.
- (3) Fujishima, A.; Honda, K. Electrochemical Photolysis of Water at a Semiconductor Electrode. *Nature* **1972**, *238*, 37-38.
- (4) Hisatomi, T.; Kubota, J.; Domen, K. Understanding TiO₂ Photocatalysis: Mechanisms and Materials *Chem. Soc. Rev.* **2014**, *43*, 7520-7535.
- (5) Zhou, H.; Qu, Y.; Zeid, T.; Duan, X. Towards highly efficient photocatalysts using semiconductor nanoarchitectures. *Energy Environ. Sci.* **2012**, *5*, 6732-6743.
- (6) Ge, M.; Li, Q.; Cao, C.; Huang, J.; Li, S.; Zhang, S.; Chen, Z.; Zhang, K.; Al-Deyab, S. S.; Lai, One-dimensional TiO₂ Nanotube Photocatalysts for Solar Water Splitting. *Adv. Sci.* **2017**, *4*, 1600152.
- (7) Wen, J.; Xie, J.; Chen, X.; Li, X. A review on g-C₃N₄-based photocatalysts. *Appl. Surf. Sci.* **2017**, *391*, 72-123.
- (8) He, R. a.; Cao, S.; Zhou, P.; Yu, J. Recent advances in visible light Bi-based photocatalysts. *Chinese J. Catal.* **2014**, *35*, 989-1007.
- (9) Elumalai, N. K.; Mahmud, M. A.; Wang, D.; Uddin, A. Perovskite Solar Cells: Progress and Advancements. *Energies* **2016**, *9*, 861.

- (10) Wu, Y.; Chen, W.; Chen, G.; Liu, L.; He, Z.; Liu, R. The Impact of Hybrid Compositional Film/Structure on Organic–Inorganic Perovskite Solar Cells. *Nanomaterials* **2018**, *8*, 356.
- (11) Tamirat, A. G.; Rick, J.; Dubale, A. A.; Su, W.-N.; Hwang, B.-J. Using hematite for photoelectrochemical water splitting: a review of current progress and challenges. *Nanoscale Horiz.* **2016**, *1*, 243-267.
- (12) Hendon, C. H.; Tiana, D.; Fontecave, M.; Sanchez, C.; D'arras, L.; Sassoey, C.; Rozes, L.; Mellot-Draznieks, C.; Walsh, A. Engineering the Optical Response of the Titanium-MIL-125 Metal–Organic Framework through Ligand Functionalization. *J. Am. Chem. Soc.* **2013**, *135*, 10942-10945.
- (13) Jiang, Y.; Cho, S.-Y.; Shim, M. Light-emitting diodes of colloidal quantum dots and nanorod heterostructures for future emissive displays. *J. Mater. Chem. C* **2018**, *6*, 2618-2634.
- (14) Kibria, M. G.; Mi, Z. Artificial photosynthesis using metal/nonmetal-nitride semiconductors: current status, prospects, and challenges. *J. Mater. Chem.* **2016**, *4*, 2801-2820.
- (15) Wang, Y.; Zhang, Z.; Zhang, L.; Luo, Z.; Shen, J.; Lin, H.; Long, J.; Wu, J. C. S.; Fu, X.; Wang, X.; Li, C. Visible-Light Driven Overall Conversion of CO₂ and H₂O to CH₄ and O₂ on 3D-SiC@2D-MoS₂ Heterostructure. *J. Am. Chem. Soc.* **2018**, *140*, 14595-14598.
- (16) Xie, S.; Zhang, Q.; Liu, G.; Wang, Y. Photocatalytic and photoelectrocatalytic reduction of CO₂ using heterogeneous catalysts with controlled nanostructures. *Chem. Commun.* **2016**, *52*, 35-39.
- (17) Wu, J.; Huang, Y.; Ye, W.; Li, Y. CO₂ Reduction: From the Electrochemical to Photochemical Approach. *Adv. Sci.* **2017**, *4*, 1700194.
- (18) Xiao, X.; Jiang, J.; Zhang, L. Selective oxidation of benzyl alcohol into benzaldehyde over semiconductors under visible light: The case of Bi₁₂O₁₇Cl₂ nanobelts. *Appl. Catal. B-Environm.* **2013**, *142-143*, 487.
- (19) Kong, D.; Zheng, Y.; Kobielski, M.; Wang, Y.; Bai, Z.; Macyk, W.; Wang, X.; Tang, J. Recent advances in visible light-driven water oxidation and reduction in suspension systems. *Mater. Today* **2018**, *21*, 897-924.
- (20) Li, X.; Yu, J.; Jaroniec, M. Hierarchical photocatalysts. *Chem. Soc. Rev.* **2016**, *45*, 2603-2636.
- (21) Stranks, S. D.; Snaith, H. J. Metal-halide perovskites for photovoltaic and light-emitting devices. *Nat. Nanotech.* **2015**, *10*, 391-402.

- (22) Ha, S.-T.; Su, R.; Xing, J.; Zhang, Q.; Xiong, Q. Metal halide perovskite nanomaterials: synthesis and applications. *Chem. Sci.* **2017**, *8*, 2522-2536.
- (23) Brenner, T. M.; Egger, D. A.; Kronik, L.; Hodes, G.; Cahen, D. Hybrid organic-inorganic perovskites: low-cost semiconductors with intriguing charge-transport properties. *Nat. Rev. Mater.* **2016**, *1*, 15007.
- (24) Mosconi, E.; Amat, A.; Nazeeruddin, M. K.; Grätzel, M.; De Angelis, F. First-Principles Modeling of Mixed Halide Organometal Perovskites for Photovoltaic Applications. *J. Phys. Chem. C* **2013**, *117*, 13902-13913.
- (25) Herz, L. M. Charge-Carrier Dynamics in Organic-Inorganic Metal Halide Perovskites. *Annu. Rev. Phys. Chem.* **2016**, *67*, 65-89.
- (26) Wehrenfennig, C.; Eperon, G. E.; Johnston, M. B.; Snaith, H. J.; Herz, L. M. High Charge Carrier Mobilities and Lifetimes in Organolead Trihalide Perovskites. *Adv. Mater.* **2014**, *26*, 1584-1589.
- (27) Jin, H.; Debroye, E.; Keshavarz, M.; Scheblykin, I. G.; Roeffaers, M. B. J.; Hofkens, J.; Steele, J. A. It's a trap! On the nature of localised states and charge trapping in lead halide perovskites. *Mater. Horizons*, **2020**, *7*, 397-410.
- (28) Park, S.; Chang, W. J.; Lee, C. W.; Park, S.; Ahn, H. Y.; Nam, K. T. Photocatalytic hydrogen generation from hydriodic acid using methylammonium lead iodide in dynamic equilibrium with aqueous solution. *Nat. Energy* **2017**, *2*, 16185.
- (29) Quan, L. N.; García de Arquer, F. P.; Sabatini, R. P.; Sargent, E. H. Metal-halide perovskites for photovoltaic and light-emitting devices. *Adv. Mater.* **2018**, *30*, 1801996.
- (30) Wang, R.; Mujahid, M.; Duan, Y.; Wang, Z.-K.; Xue, J.; Yang, Y. A Review of Perovskites Solar Cell Stability. *Adv. Funct. Mater.* **2019**, *29*, 1808843.
- (31) Yang, W. S.; Noh, J. H.; Jeon, N. J.; Kim, Y. C.; Ryu, S.; Seo, J.; Seok, S. I. High-performance photovoltaic perovskite layers fabricated through intramolecular exchange. *Science* **2015**, *348*, 1234-1237.
- (32) Zhu, Z.; Hadjiev, V. G.; Rong, Y.; Guo, R.; Cao, B.; Tang, Z.; Qin, F.; Li, Y.; Wang, Y.; Hao, F.; Venkatesan, S.; Li, W.; Baldelli, S.; Guloy, A. M.; Fang, H.; Hu, Y.; Yao, Y.; Wang, Z.; Bao, J. Interaction of Organic Cation with Water Molecule in Perovskite MAPbI₃: From Dynamic Orientational Disorder to Hydrogen Bonding *Chem. Mat.* **2016**, *28*, 7385-7393.

- (33) Murali, B.; Dey, S.; Abdelhady, A. L.; Peng, W.; Alarousu, E.; Kirmani, A. R.; Cho, N.; Sarmah, S. P.; Parida, M. R.; Saidaminov, M. I.; Zhumekenov, A. A.; Sun, J.; Alias, M. S.; Yengel, E.; Ooi, B. S.; Amassian, A.; Bakr, O. M.; Mohammed, O. F. Surface Restructuring of Hybrid Perovskite Crystals. *ACS Energy Lett.* **2016**, *1*, 1119-1126.
- (34) Kwon, Y. S.; Lim, J.; Yun, H.-J.; Kim, Y.-H.; Park, T. A diketopyrrolopyrrole-containing hole transporting conjugated polymer for use in efficient stable organic-inorganic hybrid solar cells based on a perovskite. *Energy Environ. Sci.* **2014**, *7*, 1454-1460.
- (35) Christians J. A.; Miranda Herrera P. A.; Kamat. P. V. Transformation of the Excited State and Photovoltaic Efficiency of $\text{CH}_3\text{NH}_3\text{PbI}_3$ Perovskite upon Controlled Exposure to Humidified Air. *J. Am. Chem. Soc.* **2015**, *137*, 1530-1538.
- (36) Yang J.; Siempelkamp B. D.; Liu D.; Kelly T. L. Investigation of $\text{CH}_3\text{NH}_3\text{PbI}_3$ Degradation Rates and Mechanisms in Controlled Humidity Environments Using *in Situ* Techniques. *ACS Nano* **2015**, *9*, 1955-1963.
- (37) Mosconi E.; Azpiroz J. M.; Angelis F. D. Ab Initio Molecular Dynamics Simulations of Methylammonium Lead Iodide Perovskite Degradation by Water. *Chem. Mater.* **2015**, *27*, 4885-4892.
- (38) Niu, G.; Guo, X.; Wang, L. Review of recent progress in chemical stability of perovskite solar cells. *J Mater. Chem. A* **2015**, *3*, 8970-8980.
- (39) Huang, J. B.; Tan, S. Q.; Lund, P. D.; Zhou, H. P. Impact of H_2O on organic-inorganic hybrid perovskite solar cells. *Energy Environ. Sci.* **2017**, *10*, 2284-2311.
- (40) Boyd, C. C.; Cheacharoen, R.; Leijtens, T.; McGehee, M. D. Understanding Degradation Mechanisms and Improving Stability of Perovskite Photovoltaics. *Chem. Rev.* **2019**, *119*, 3418-3451
- (41) El-Mellouhi, F.; Marzouk, A.; Bentría, E. T.; Rashkeev, S. N.; Kais, S.; Alharbi, F. H. Hydrogen Bonding and Stability of Hybrid Organic-Inorganic Perovskites. *ChemSusChem* **2016**, *9*, 2648-2655.
- (42) Manser, J. S.; Saidaminov, M. I.; Christians, J. A.; Bakr, O. M.; Kamat, P. V. Making and Breaking of Lead Halide Perovskites. *Accounts Chem. Res.* **2016**, *49*, 330-338.
- (43) Jeon, N. J.; Noh, J. H.; Kim, Y. C.; Yang, W. S.; Ryu, S.; Seok, S. I. Solvent engineering for high-performance inorganic–organic hybrid perovskite solar cells. *Nat. Mater.* **2014**, *13*, 897.

- (44) Jung, M.; Ji, S.-G.; Kim, G.; Seok, S. I. Perovskite precursor solution chemistry: from fundamentals to photovoltaic applications. *Chem. Soc. Rev.* **2019**, *48*, 2011-2038.
- (45) Noel, N. K.; Habisreutinger, S. N.; Wenger, B.; Klug, M. T.; Hörantner, M. T.; Johnston, M. B.; Nicholas, R. J.; Moore, D. T.; Snaith, H. J. A low viscosity, low boiling point, clean solvent system for the rapid crystallisation of highly specular perovskite films. *Energy Environ. Sci.* **2017**, *10*, 145-152.
- (46) Pearson, A. J.; Eperon, G. E.; Hopkinson, P. E.; Habisreutinger, S. N.; Wang, J. T. W.; Snaith, H. J.; Greenham, N. C. Oxygen Degradation in Mesoporous Al₂O₃/CH₃NH₃PbI_{3-x}Cl_x Perovskite Solar Cells: Kinetics and Mechanisms. *Adv. Energy Mater.* **2016**, *6*, 1600014.
- (47) Abdelmageed, G.; Jewell, L.; Hellier, K.; Seymour, L.; Luo, B.; Bridges, F.; Zhang, J. Z.; Carter, S. Mechanisms for light induced degradation in MAPbI₃ perovskite thin films and solar cells. *Appl. Phys. Lett.* **2016**, *109*, 233905.
- (48) Aristidou, N.; Eames, C.; Sanchez-Molina, I.; Bu, X. N.; Kosco, J.; Islam, M. S.; Haque, S. A. Fast oxygen diffusion and iodide defects mediate oxygen-induced degradation of perovskite solar cells. *Nat. Commun.* **2017**, *8*, 15218.
- (49) Kulbak, M.; Gupta, S.; Kedem, N.; Levine, I.; Bendikov, T.; Hodes, G.; Cahen, D. Cesium enhances long-term stability of lead bromide perovskite-based solar cells. *J. Phys. Chem. Lett.* **2016**, *7*, 167-172.
- (50) Lee, J.W.; Kim, D.H.; Kim, H.S.; Seo, S.W.; Cho, S.M.; Park, N.G. Formamidinium and cesium hybridization for photo-and moisture-stable perovskite solar cell. *Adv. Energy Mater.* **2015**, *5*, 1501310.
- (51) Zheng, C.; Rubel, O.; Ionization Energy as a Stability Criterion for Halide Perovskites. *J. Phys. Chem. C*, **2017**, *121*, 22, 11977-11984
- (52) Kim, Y.; Yassitepe, E.; Voznyy, O.; Comin, R.; Walters, G.; Gong, X.; Kanjanaboos, P.; Nogueira, A. F.; Sargent, E. H. Efficient Luminescence from Perovskite Quantum Dot Solids. *ACS Appl. Mater. Interfaces* **2015**, *7*, 25007-25013.
- (53) Wu, Y.; Wang, P.; Zhu, X.; Zhang, Q.; Wang, Z.; Liu, Y.; Zou, G.; Dai, Y.; Whangbo, M.-H.; Huang, B. Composite of CH₃NH₃PbI₃ with Reduced Graphene Oxide as a Highly Efficient and Stable

Visible-Light Photocatalyst for Hydrogen Evolution in Aqueous HI Solution. *Adv. Mater.* **2018**, *30*, 1704342.

(54) Wu, Y.; Wang, P.; Guan, Z.; Liu, J.; Wang, Z.; Zheng, Z.; Jin, S.; Dai, Y.; Whangbo, M.-H.; Huang, B. Enhancing the Photocatalytic Hydrogen Evolution Activity of Mixed-Halide Perovskite $\text{CH}_3\text{NH}_3\text{PbBr}_{3-x}\text{I}_x$ Achieved by Bandgap Funneling of Charge Carriers. *ACS Catal.* **2018**, *8*, 10349-10357.

(55) Guan, Z.; Wu, Y.; Wang, P.; Zhang, Q.; Wang, Z.; Zheng, Z.; Liu, Y.; Dai, Y.; Whangbo, M.-H.; Huang, B. Perovskite photocatalyst $\text{CsPbBr}_{3-x}\text{I}_x$ with a bandgap funnel structure for H_2 evolution under visible light. *Appl. Catal. B-Environ.* **2019**, *245*, 522-527.

(56) Wang, H.; Wang, X.; Chen, R.; Zhang, H.; Wang, X.; Wang, J.; Zhang, J.; Mu, L.; Wu, K.; Fan, F.; Zong, X.; Li, C. Promoting Photocatalytic H_2 Evolution on Organic-Inorganic Hybrid Perovskite Nanocrystals by Simultaneous Dual-Charge Transportation Modulation. *ACS Energy Lett.* **2019**, *4*, 40-47.

(57) Wang, X.; Wang, H.; Zhang, H.; Yu, W.; Wang, X.; Zhao, Y.; Zong, X.; Li, C. Dynamic Interaction between Methylammonium Lead Iodide and TiO_2 Nanocrystals Leads to Enhanced Photocatalytic H_2 Evolution from HI Splitting. *ACS Energy Lett.* **2018**, *3*, 1159-1164.

(58) Luo, J.; Yang, H.; Liu, Z.; Li, F.; Liu, S.; Ma, J.; Liu, B. Organic-inorganic hybrid perovskite - TiO_2 nanorod arrays for efficient and stable photoelectrochemical hydrogen evolution from HI splitting *Mater. Today Chem.* **2019**, *12*, 1-6.

(59) Li, R.; Li, X.; Wu, J.; Lv, X.; Zheng, Y.-Z.; Zhao, Z.; Ding, X.; Tao, X.; Chen, J.-F. Few-layer black phosphorus-on- MAPbI_3 for superb visible-light photocatalytic hydrogen evolution from HI splitting. *Appl. Catal. B-Environ.* **2019**, *259*, 118075

(60) Guo, Y.; Liu, G.; Li, Z.; Lou, Y.; Chen, J.; Zhao, Y. Stable Lead-Free $(\text{CH}_3\text{NH}_3)_3\text{Bi}_2\text{I}_9$ Perovskite for Photocatalytic Hydrogen Generation. *ACS Sustainable Chem. Eng.* **2019**, *7*, 15080-15085.

(61) Wang, T.; Yue, D.; Li, X.; Zhao, Y. Lead-free double perovskite $\text{Cs}_2\text{AgBiBr}_6/\text{RGO}$ composite for efficient visible light photocatalytic H_2 evolution. *Appl. Catal. B-Environm.* **2019**, 118399.

(62) Xu, Y. F.; Yang, M. Z.; Chen, B. X.; Wang, X. D.; Chen, H. Y.; Kuang, D. B.; Su, C. Y. A CsPbBr_3 Perovskite Quantum Dot/Graphene Oxide Composite for Photocatalytic CO_2 Reduction. *J. Am. Chem. Soc.* **2017**, *139*, 5660-5663.

- (63) Huang, H.; Yuan, H.; Janssen, K. P. F.; Solís-Fernández, G.; Wang, Y.; Tan, C. Y. X.; Jonckheere, D.; Debroye, E.; Long, J.; Hendrix, J.; Hofkens, J.; Steele, J. A.; Roeffaers, M. B. J. Efficient and Selective Photocatalytic Oxidation of Benzylic Alcohols with Hybrid Organic–Inorganic Perovskite Materials. *ACS Energy Lett.* **2018**, *3*, 755-759.
- (64) Huang, H.; Yuan, H.; Zhao, J.; Solís-Fernández, G.; Zhou, C.; Seo, J. W.; Hendrix, J.; Debroye, E.; Steele, J. A.; Hofkens, J.; Long, J.; Roeffaers, M. B. J. C(sp³)-H Bond Activation by Perovskite Solar Photocatalyst Cell. *ACS Energy Lett.* **2014**, *4*, 203-208.
- (65) Zhu, X.; Lin, Y.; San Martin, J.; Sun, Y.; Zhu, D.; Yan, Y. Lead halide perovskites for photocatalytic organic synthesis. *Nat. Commun.* **2019**, *10*, 2843.
- (66) Zhu, X.; Lin, Y.; Sun, Y.; Beard, M. C.; Yan, Y. Lead-Halide Perovskites for Photocatalytic α -Alkylation of Aldehydes. *J. Am. Chem. Soc.* **2019**, *141*, 733-738.
- (67) Chen, K.; Deng, X. H.; Dodekatos, G.; Tuysuz, H. Photocatalytic Polymerization of 3,4-Ethylenedioxythiophene over Cesium Lead Iodide Perovskite Quantum Dots. *J. Am. Chem. Soc.* **2017**, *139*, 12267-12273.
- (68) Wu, W. B.; Wong, Y. C.; Tan, Z. K.; Wu, J.. Photo-induced thiol coupling and C-H activation using nanocrystalline lead-halide perovskite catalysts. *Catal. Sci. Technol.* **2018**, *8*, 4257-4263.
- (69) Ou, M.; Tu, W.; Yin, S.; Xing, W.; Wu, S.; Wang, H.; Wan, S.; Zhong, Q.; Xu, R. Amino-Assisted Anchoring of CsPbBr₃ Perovskite Quantum Dots on Porous g-C₃N₄ for Enhanced Photocatalytic CO₂ Reduction *Angew. Chem.* **2018**, *130*, 13758-13762.
- (70) Guo, S.-H.; Zhou, J.; Zhao, X.; Sun, C.-Y.; You, S.-Q.; Wang, X.-L.; Su, Z.-M. Enhanced CO₂ photoreduction via tuning halides in perovskites *J. Catal.* **2019**, *369*, 201-208.
- (71) Hou, J.; Cao, S.; Wu, Y.; Gao, Z.; Liang, F.; Sun, Y.; Lin, Z.; Sun, L. Inorganic Colloidal Perovskite Quantum Dots for Robust Solar CO₂ Reduction. *Chem: Eur. J.* **2017**, *23*, 9481-9485.
- (72) Zhou, L.; Xu, Y.-F.; Chen, B.-X.; Kuang, D.-B.; Su, C.-Y. Synthesis and Photocatalytic Application of Stable Lead-Free Cs₂AgBiBr₆ Perovskite Nanocrystals. *Small* **2018**, *14*, 1703762.
- (73) Pan, A.; Ma, X.; Huang, S.; Wu, Y.; Jia, M.; Shi, Y.; Liu, Y.; Wangyang, P.; He, L.; Liu, Y. CsPbBr₃ Perovskite Nanocrystal Grown on MXene Nanosheets for Enhanced Photoelectric Detection and Photocatalytic CO₂ Reduction. *J. Phys. Chem. Lett.* **2019**, *10*, 6590-6597.

- (74) Cardenas-Morcoso, D.; Gualdrón-Reyes, A. F.; Ferreira Vitoreti, A. B.; García-Tecedor, M.; Yoon, S. J.; Solis de la Fuente, M.; Mora-Seró, I.; Gimenez, S. Photocatalytic and Photoelectrochemical Degradation of Organic Compounds with All-Inorganic Metal Halide Perovskite Quantum Dots. *J. Phys. Chem. Lett.* **2019**, *10*, 630-636.
- (75) Guo, X.-X.; Tang, S.-F.; Mu, Y.-F.; Wu, L.-Y.; Dong, G.-X.; Zhang, M. Engineering a CsPbBr₃-based nanocomposite for efficient photocatalytic CO₂ reduction: improved charge separation concomitant with increased activity sites. *RSC Adv.* **2019**, *9*, 34342-34348.
- (76) Feng, X.; Ju, H.; Song, T.; Fang, T.; Liu, W.; Huang, W. Highly Efficient Photocatalytic Degradation Performance of CsPb(Br_{1-x}Cl_x)₃-Au Nanoheterostructures. *ACS Sustainable Chem. Eng.* **2019**, *7*, 5152-5156.
- (77) Gualdrón Reyes, A. F.; Rodriguez-Pereira, J.; Amado - Gonzalez, E.; Rueda-P, J.; Ospina, R.; Masi, S.; Yoon, S. J.; Tirado, J.; Jaramillo, F.; Agouram, S.; Munoz-Sanjose, V.; Gimenez, S.; Mora-Seró, I. Unravelling the Photocatalytic Behavior of All-Inorganic Mixed Halide Perovskites: The Role of Surface Chemical States. *ACS Appl. Mater. Interfaces* **2020**, *12*, 914-924
- (78) Dai, Y.; Poidevin, C.; Ochoa-Hernández, C.; Auer, A.; Tüysüz, H. Supported bismuth halide perovskite photocatalyst for selective aliphatic and aromatic C-H bond activation. *Angew. Chem. Int. Ed.* **2020**, *59*, 2-11.
- (79) Schünemann, S.; van Gastel, M.; Tüysüz, H. A CsPbBr₃ /TiO₂ Composite for Visible-Light-Driven Photocatalytic Benzyl Alcohol Oxidation. *ChemSusChem* **2018**, *11*, 2057-2061.
- (80) Hong, Z.; Chong, W. K.; Ng, A. Y. R.; Li, M.; Ganguly, R.; Sum, T. C.; Soo, H. S. Hydrophobic Metal Halide Perovskites for Visible-Light Photoredox C-C Bond Cleavage and Dehydrogenation Catalysis. *Angew. Chem. Int. Ed.* **2019**, *58*, 3456-3460.
- (81) Xu, Y.-F.; Wang, X.-D.; Liao, J.-F.; Chen, B.-X.; Chen, H.-Y.; Kuang, D.-B. Amorphous-TiO₂-Encapsulated CsPbBr₃ Nanocrystal Composite Photocatalyst with Enhanced Charge Separation and CO₂ Fixation. *Adv. Mater. Interfaces* **2018**, *5*, 1801015.
- (82) Li, Z.-J.; Hofman, E.; Li, J.; Davis, A. H.; Tung, C.-H.; Wu, L.-Z.;f Zheng, W. Photoelectrochemically Active and Environmentally Stable CsPbBr₃/TiO₂ Core/Shell Nanocrystals. *Adv. Funct. Mater.* **2018**, *28*, 1704288.

- (83) Wu, L.-Y.; Mu, Y.-F.; Guo, X.-X.; Zhang, W.; Zhang, Z.-M.; Zhang, M.; Lu, T.-B. Encapsulating Perovskite Quantum Dots in Iron-Based Metal-Organic Frameworks (MOFs) for Efficient Photocatalytic CO₂ Reduction. *Angew. Chem. Int. Ed.* **2019**, *58*, 9491-9495.
- (84) Kong, Z.-C.; Liao, J.-F.; Dong, Y.-J.; Xu, Y.-F.; Chen, H.-Y.; Kuang, D.-B.; Su, C.-Y. Core@Shell CsPbBr₃@Zeolitic Imidazolate Framework Nanocomposite for Efficient Photocatalytic CO₂ Reduction. *ACS Energy Lett.* **2018**, *3*, 2656-2662.
- (85) Nam, S.; Mai, C. T. K.; Oh, I. Ultrastable Photoelectrodes for Solar Water Splitting Based on Organic Metal Halide Perovskite Fabricated by Lift-Off Process. *ACS Appl. Mater. Interfaces* **2018**, *10*, 14659-14664.
- (86) Mollick, S.; Mandal, T. N.; Jana, A.; Fajal, S.; Desai, A. V.; Ghosh, S. K. Ultrastable Luminescent Hybrid Bromide Perovskite@MOF Nanocomposites for the Degradation of Organic Pollutants in Water. *ACS Appl. Nano Mater.* **2019**, *2*, 1333-1340.
- (87) Chen, Y. S.; Manser, J. S.; Kamat, P. V. All Solution-Processed Lead Halide Perovskite-BiVO₄ Tandem Assembly for Photolytic Solar Fuels Production. *J. Am. Chem. Soc.* **2015**, *137*, 974-981.
- (88) Da, P. M.; Cha, M. Y.; Sun, L.; Wu, Y. Z.; Wang, Z. S.; Zheng, G. F. High-Performance Perovskite Photoanode Enabled by Ni Passivation and Catalysis. *Nano Lett.* **2015**, *15*, 3452-3457.
- (89) Gurudayal; Sabba, D.; Kumar, M. H.; Wong, L. H.; Barber, J.; Gratzel, M.; Mathews, N. Perovskite-Hematite Tandem Cells for Efficient Overall Solar Driven Water Splitting. *Nano Lett.* **2015**, *15*, 3833-3839.
- (90) Luo, J. S.; Im, J. H.; Mayer, M. T.; Schreier, M.; Nazeeruddin, M. K.; Park, N. G.; Tilley, S. D.; Fan, H. J.; Gratzel, M. Water photolysis at 12.3% efficiency via perovskite photovoltaics and Earth-abundant catalysts. *Science* **2014**, *345*, 1593-1596.
- (91) Crespo-Quesada, M.; Pazos-Outon, L. M.; Warnan, J.; Kuehnel, M. F.; Friend, R. H.; Reisner, E. Metal-encapsulated organolead halide perovskite photocathode for solar-driven hydrogen evolution in water. *Nat. Commun.* **2016**, *7*, 12555.
- (92) Mu, Y.-F.; Zhang, W.; Guo, X.-X.; Dong, G.-X.; Zhang, M.; Lu, T.-B. Water-Tolerant Lead Halide Perovskite Nanocrystals as Efficient Photocatalysts for Visible-Light-Driven CO₂ Reduction in Pure Water. *ChemSusChem* **2019**, *12*, 4769-4774.

- (93) Andrei, V.; Reuillard, B.; Reisner, E. Bias-free solar syngas production by integrating a molecular cobalt catalyst with perovskite–BiVO₄ tandems. *Nat. Mater.* **2020**, *19*, 289-194.
- (94) Poli, I.; Hintermair, U.; Regue, M.; Kumar, S.; Sackville, E. V.; Baker, J.; Watson, T. M.; Eslava, S.; Cameron, P. J. Graphite-protected CsPbBr₃ perovskite photoanodes functionalised with water oxidation catalyst for oxygen evolution in water. *Nat. Commun.* **2019**, *10*, 2097.
- (95) Wang, Q.; Qin, W.; Wu, X.; Yu, S. Isopropanol-assisted synthesis of highly stable MAPbBr₃/p-g-C₃N₄ intergrowth composite photocatalysts and their interfacial charge carrier dynamics. *Nanoscale Adv.* **2020**, *2*, 274-285.
- (96) Jiang, Y.; Liao, J.-F.; Xu, Y.-F.; Chen, H.-Y.; Wang, X.-D.; Kuang, D.-B. Hierarchical CsPbBr₃ nanocrystal-decorated ZnO nanowire/macroporous graphene hybrids for enhancing charge separation and photocatalytic CO₂ reduction. *J. Mater. Chem. A* **2019**, *7*, 13762-13769.
- (97) Wang, X.-D.; Huang, Y.-H.; Liao, J.-F.; Jiang, Y.; Zhou, L.; Zhang, X.-Y.; Chen, H.-Y.; Kuang, D.-B. *In Situ* Construction of a Cs₂SnI₆ Perovskite Nanocrystal/SnS₂ Nanosheet Heterojunction with Boosted Interfacial Charge Transfer. *J. Am. Chem. Soc.* **2019**, *141*, 13434-13441.
- (98) Bhosale, S. S.; Kharade, A. K.; Jokar, E.; Fathi, A.; Chang, S.-m.; Diao, E. W.-G. Mechanism of Photocatalytic CO₂ Reduction by Bismuth-Based Perovskite Nanocrystals at the Gas–Solid Interface. *J. Am. Chem. Soc.* **2019**, *141*, 51, 20434-20442.
- (99) Reyes-Pérez, F.; Gallardo, J. J.; Aguilar, T.; Alcántara, R.; Fernández-Lorenzo, C.; Navas, J. Visible-Light-Enhanced Photocatalytic Activity of Totally Inorganic Halide-Based Perovskite. *ChemistrySelect* **2018**, *3*, 10226-10235.
- (100) Zhang, Z.; Liang, Y.; Huang, H.; Liu, X.; Li, Q.; Chen, L.; Xu, D. Stable and Highly Efficient Photocatalysis with Lead-Free Double-Perovskite of Cs₂AgBiBr₆. *Angew. Chem. Int. Ed.* **2019**, *58*, 7263-7267.
- (101) Dai, Y.; Tüysüz, H. Lead-Free Cs₃Bi₂Br₉ Perovskite as Photocatalyst for Ring-Opening Reactions of Epoxides. *ChemSusChem* **2019**, *12*, 2587-2592.
- (102) Qian, X.; Chen, Z.; Yang, X.; Zhao, W.; Liu, C.; Sun, T.; Zhou, D.; Yang, Q.; Wei, G.; Fan, M. Perovskite cesium lead bromide quantum dots: A new efficient photocatalyst for degrading antibiotic residues in organic system. *J. Clean. Prod.* **2020**, *249*, 119335.

- (103) Schneider, J.; Bahnemann, D. W. Undesired Role of Sacrificial Reagents in Photocatalysis. *J. Phys. Chem. Lett.* **2013**, *4*, 3479-3483.
- (104) Yang, J.; Wang, D.; Han, H.; Li, C. Roles of Cocatalysts in Photocatalysis and Photoelectrocatalysis. *Acc. Chem. Res.* **2013**, *46*, 1900-1909
- (105) Panayotov D. A.; Frenkel A. I.; Morris J. R.; Catalysis and Photocatalysis by Nanoscale Au/TiO₂: Perspectives for Renewable Energy *ACS Energy Lett.* **2017**, *2*, 1223-1231.
- (106) Yan, J.; Qiu, W.; Wu, G.; Heremans, P.; Chen, H. Recent progress in 2D/quasi-2D layered metal halide perovskites for solar cells. *J. Mater. Chem. A* **2018**, *6*, 11063-11077.
- (107) Andrei, V.; Hoyer, R. L. Z.; Crespo-Quesada, M.; Bajada, M.; Ahmad, S.; De Volder, M.; Friend, R.; Reisner, E. Scalable Triple Cation Mixed Halide Perovskite-BiVO₄ Tandems for Bias-Free Water Splitting. *Adv. Energy Mater.* **2018**, *8*, 1801403.
- (108) Gupta, S.; Bendikov, T.; Hodes, G.; Cahen, D. CsSnBr₃, A Lead-Free Halide Perovskite for Long-Term Solar Cell Application: Insights on SnF₂ Addition. *ACS Energy Lett.* **2016**, *1*, 1028-1033.
- (109) Zhou, Y.; Zhao, Y., Chemical stability and instability of inorganic halide perovskites. *Energy Environ. Sci.* **2019**, *12*, 1495-1511.

Chapter 2

Efficient and Selective Photocatalytic Oxidation of Benzylic Alcohols with Hybrid Organic–Inorganic Perovskite Materials

Haowei Huang, Haifeng Yuan*, Kris P. F. Janssen, Guillermo Solís-Fernández, Ying Wang, Collin Y. X. Tan, Dries Jonckheere, Elke Debroye, Jinlin Long, Jelle Hendrix, Johan Hofkens*, Julian A. Steele, Maarten B. J. Roeffaers*

Adapted with permission from ACS Energy Lett. 2018, 3, 4, 755-759

The original article is licensed under the ACS AuthorChoice license, and further permission requests should be directed to the ACS.

<https://pubs.acs.org/doi/abs/10.1021/acsenergylett.8b00131>

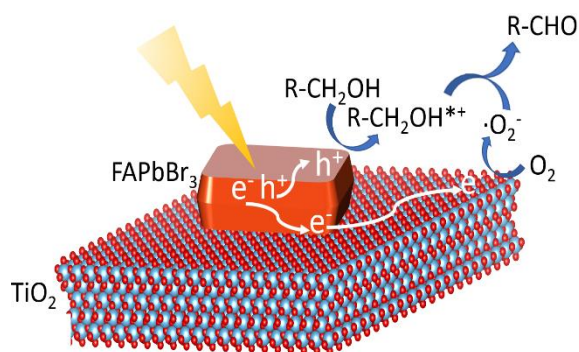
Copyright © 2018 American Chemical Society

Contributions

H.H., H. Y., J. H. and M.B.J.R. designed the project; H.H. conducted the most experiments, including samples preparation, SEM, DRS, PL, PLQY, and activity tests; G.S.F., Y. W., C. Y. X. T, and D. J. performed part of the experiments; K.P.F.J., E.D., J. H., and J. L. supported the experiments and helped to analyse the results; H.H. analyzed all results and wrote the draft; H. H., H. Y., J. A.S. and M.B.J.R. together revised the manuscript with input from all the authors.

Abstract: The impressive optoelectronic performance and low production cost of metal halide perovskites have inspired applications well beyond efficient solar cells. Herein, we widen the materials engineering options available for the efficient and selective photocatalytic oxidation of benzylic alcohols – an industrially significant reaction – using formamidinium lead bromide (FAPbBr₃) and other perovskite based materials. The best performance was obtained using a FAPbBr₃/TiO₂ hybrid photocatalyst under simulated solar illumination. Detailed optical studies reveal the synergetic photophysical pathways arising in FAPbBr₃/TiO₂ composites. An experimentally supported model rationalizing the large conversion enhancement over the pure constituents shows that this strategy offers new prospects for metal halide perovskites in photocatalytic application.

Table of Contents



2.1 Introduction

Organic-inorganic halide perovskites (OIHPs) have emerged as an extremely exciting family of semiconductor materials, garnering strong promise for a range of photonic applications. This stems from several advantages of OIHPs over other well-established semiconductors, such as low-cost facile processing, tunable bandgaps, and superior charge transport properties.¹ Early interest for OIHPs was sparked by their immediate success in efficient light harvesting.^{2,3} In just a few years perovskite-based solar cell devices have rocketed to remarkably high power conversion efficiencies, exceeding 22%.⁴

While novel photon-electrical and electrical-photon energy conversions using OIHPs continues to embody main stream perovskites research, their application in photocatalytic and photoelectrochemical processes remains relatively unexplored. Among many candidates for semiconductor photocatalysts, titanium dioxide (TiO₂) is at present a prominent choice within both industry and fundamental research, due to its wide optical bandgap (380 nm), efficient photoactivity however limited to UV, high stability, and low cost.⁵ On the other hand, OIHPs offer strong potential to extend the efficient harvesting and utilization of light well into visible wavelengths. Yet the inherent instability of organic halide perovskites when exposed to moisture make them generally incompatible with typical photocatalytic reactions in aqueous media, like water splitting, CO₂ reduction, and organic waste decomposition. Recently, Nam *et al.*⁶ overcame this limitation by using an oversaturated aqueous HI solution, and all-inorganic CsPbBr₃ and CsPbI₃ quantum dots^{7,8} have been applied in the photocatalytic reduction of CO₂ and the oxidation of PEDOT respectively. Considering how the interesting properties of OIHPs (high solar absorption and good charge separation and transport) continue to offer inexpensive solutions to a wide variety of optics research problems, it is surprising that serious efforts to exploit OIHPs for improving important photocatalytic reactions is yet to be made. One of the extremely important industrial organic reactions is the selective oxidation of alcohols to carbonyls,^{9,10} which is conventionally performed by stoichiometric quantities of inorganic oxidant; notably dichromate and permanganate, noble metal catalysts Pt, Pd, Au, or organic oxidants such as 2, 2, 6, 6-tetramethylpiperidine oxide.¹⁰⁻¹⁷

Herein we build on the strong photoactivity of formamidinium (FA; HC(NH₂)₂⁺) lead bromide (FAPbBr₃) perovskites for the highly efficient and selective photocatalytic oxidation of benzylic alcohols. By utilizing the relative band alignment of photo-generated charge carriers within in FAPbBr₃/TiO₂ hybrids,^{18,19} the best performance under simulated solar illuminated was obtained. The photophysical pathways of photo-

excited carriers within the hybrid system are detailed and are found to benefit from truly synergetic effects; namely, the improved separation and transport of electrons and holes into their respective active regions.

2.2 Results

Our FAPbBr₃, TiO₂ and FAPbBr₃/TiO₂ samples are prepared using a simple room-temperature antisolvent precipitation method,²⁰ with further procedural details provided in the Supporting Information. Pure FAPbBr₃ and TiO₂ crystallize into their thermodynamically stable cubic perovskite and anatase phases, respectively (powder X-ray diffraction (p-XRD), Figure 2-S1).²⁰⁻²² p-XRD of FAPbBr₃/TiO₂ consists of peaks from both phases, indicating successful synthesis of a FAPbBr₃/TiO₂ hybrid. Scanning electron microscopy (SEM) of the system further confirms this result, as shown in Figure 2-S2. From the SEM micrographs, the average size of the pure FAPbBr₃ is around 3 μm. In contrast, the average size of the hybrid material obtained via the same antisolvent precipitation however in presence of the anatase TiO₂ as seed is about 180 nm, being one order of magnitude smaller than pure FAPbBr₃. Besides their morphological differences, X-ray photoelectron spectroscopy (XPS) experiments (Figure 2-S3) reveals no difference in the chemical state of the FAPbBr₃ in the pristine or TiO₂ mixed material. Rather, TiO₂ influences the FAPbBr₃ crystallization process yielding smaller crystals. The particle size, shape and crystallinity can be affected by altering the nucleation process and the subsequent crystal growth. Not that, the number of seeds and the size of the final product will be inversely proportional to each other. When these TiO₂ NPs were used as seeds for FAPbBr₃ growth, TiO₂ acts as a nucleation point. The large surface area enhances the precipitation and nucleation rate of MHP which caused more MHP seeds and yielded smaller crystals.

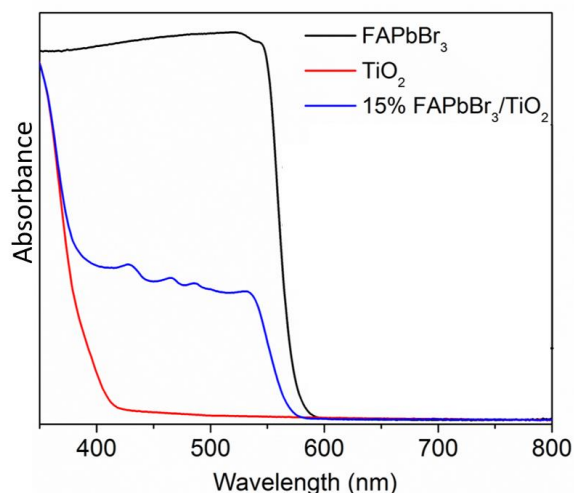


Figure 2-1. UV–Vis DRS spectra of FAPbBr₃, TiO₂, and 15% FAPbBr₃/TiO₂.

The optical absorption edges of FAPbBr₃, TiO₂ and FAPbBr₃/TiO₂ are determined from UV-Vis diffuse reflection spectroscopy (DRS, Figure 2-1). Typical bandgaps are seen here for both pure materials; 380 nm (3.2 eV) for anatase TiO₂ and 580 nm (2.2 eV) for FAPbBr₃.^{21,23,24} Compared to bare TiO₂, the absorption properties of 15% FAPbBr₃/TiO₂ is enhanced substantially in the visible, through the superposition of both characteristic absorption spectra. The absorption edge corresponding to FAPbBr₃ in the mixed material is slightly blue shifted by 10 nm, relative to pure FAPbBr₃, attributed to the reduced crystal sizes.²⁴ FAPbBr₃/TiO₂ materials with relative compositions of 1, 5, 10, and 25 wt% FAPbBr₃ are also synthesized, with their optical properties summarized in Figure 2-S4. In accordance with increasing absorption volume, elevating the relative concentration of FAPbBr₃ in the composite also sees the weight of the Vis absorption increase. Furthermore, there are some extra absorption features (400~500 nm) in FAPbBr₃/TiO₂, which can be attributed to a minor contribution from 2D perovskites.²⁴

Next, the photocatalytic properties of the full range of materials synthesised are evaluated under simulated solar illumination by applying the selective photocatalytic oxidation of benzylic alcohol in an apolar solvent (toluene) and using molecular oxygen. Their photocatalytic performances are displayed in Figure 2-2A, where the pure FAPbBr₃ and TiO₂ (10 mg) controls both exhibit a conversion rate of roughly 15 % (0.1mmol benzyl alcohol in 2.5 ml toluene), after 8 h illumination. However, their conversion selectivity to benzaldehyde differs from 99 % for pure FAPbBr₃ to 95 % for pure TiO₂ with benzoic acid as main side product. On the other hand, considering the performance of the FAPbBr₃/TiO₂ composite series in Figure 2-2A, a substantial enhancement is exhibited by the hybrid system, compared its pure constituents. The addition of only 1wt% of FAPbBr₃ already leads to a doubling in activity compared to pure TiO₂. The highest photocatalytic conversion of benzyl alcohol peaked at 63 % for the 15 wt% FAPbBr₃/TiO₂ composite, totalling a 4-fold enhancement over the pure controls. Further increases in the FAPbBr₃ amount over 15 wt% reduces the conversion rate. This can be attributed to two reasons: (1) the increased quantity of perovskite precursors leads to larger FAPbBr₃ nanocrystals and aggregates resulting in longer distances to be travelled by the formed charge carriers and thus reducing the efficiency of charge separation; (2) the increased TiO₂ surface coverage by perovskite materials also reduces the exposed surface area of TiO₂ to the reagent solution. TiO₂ plays an important role in charge separation and it reduces O₂ to form the reactive superoxide radical, as described in scheme 1. As a result of both of these

factors excessive amounts of perovskite will not necessarily lead to further improved photocatalytic performance.

Clearly, combining the two solid-state semiconductors dramatically increases its overall capacity for photocatalytic oxidation of benzyl alcohol, without compromising the excellent reaction selectivity (99 % across all composites). However, the potential influence of size effects is yet to be considered. To assess the possible role crystal size might play, nanocrystalline FAPbBr₃ was synthesized using an altered synthesis procedure (see Supporting information for experimental and characterization details). Additionally, the synergetic role between both materials was evaluated by preparing FAPbBr₃/SiO₂ using the same antisolvent method and mechanical mixed FAPbBr₃/TiO₂-M. With these materials - controlling for the morphological parameters such as size and utilizing a mixed media - no discernible benefit was gained; full summary of the activity results can be found in Table 2-S1. Nano FAPbBr₃ presented a similar activity as the FAPbBr₃ microcrystals, indicating that the size of FAPbBr₃ does not affect the photoactivity in this case. Then, the addition of a support material without the interaction with FAPbBr₃ such as SiO₂ does not lead to an enhanced activity in FAPbBr₃/SiO₂ composite. Furthermore, compared to the sum of FAPbBr₃ and TiO₂ on BA conversion (30 % = 15% + 15%), there is a ca. two-fold enhancement of BA conversion for the FAPbBr₃/TiO₂ photocatalyst (63%). Thus, the enhanced photocatalytic performance exhibited by the FAPbBr₃/TiO₂ hybrid systems must ultimately manifest from an intrinsic synergy arising from the interplay between the composite and the interface.^{18,19}

The stability of the materials when exposed to repeated reaction cycles is further tested. Figure 2-2B shows the results from both FAPbBr₃ and 15% FAPbBr₃/TiO₂ following their reuse as a photocatalyst during five reaction cycles. While no reduction in activity is observed in the pure FAPbBr₃ sample, the FAPbBr₃/TiO₂ composite slowly decreased in activity. Based on additional experiments (Figure 2-S6) we conclude that the more polar reaction product, benzaldehyde, leads to a partial dissolution of the FAPbBr₃, an effect that is accelerated by illumination. Therefore, the FAPbBr₃ content in the hybrid composite reduces while more benzaldehyde is produced, resulting in a notable effect on the activity of FAPbBr₃/TiO₂. The slow dissolution of the perovskite material is currently limiting the long-term stability of the catalysts and may cause Pb pollution. We remain optimistic that this problem can be resolved in the future by (1) minimizing the contact between the photocatalyst and the more polar reaction products, (2) further developments of lead-free OIHP photocatalysts. The turnover number (TON) of benzyl alcohol oxidation on 15%

FAPbBr₃/TiO₂ is 89 at the first 5 cycles, which shows that benzyl alcohol oxidation on FAPbBr₃/TiO₂ is a real catalytic reaction.

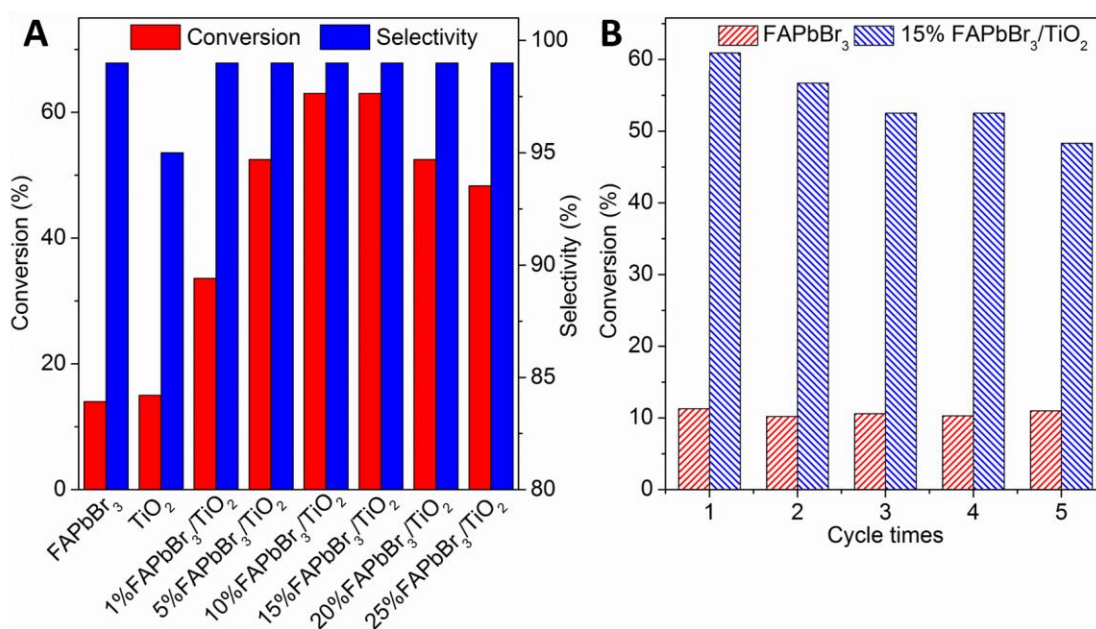


Figure 2-2. (A) Photocatalytic oxidation of benzyl alcohol over pure FAPbBr₃, TiO₂ and a series of FAPbBr₃/TiO₂ hybrids. (B) Recycle test for pure FAPbBr₃ and 15% FAPbBr₃/TiO₂. Reaction conditions: benzyl alcohol (0.1 mmol), photocatalysts (0.01 g), solvent of toluene (2.5 mL) saturated with molecular oxygen, AM1.5G simulated light irradiation, irradiation time (8 h).

Interestingly, the ability for FAPbBr₃/TiO₂ composites to oxidise with high selectivity alcohols is not merely limited to benzyl alcohol. As summarized in Table 2-S2 high selectivity is also realised when performing similar experiments on other aromatic alcohols. Additionally, we further tested other popular wide bandgap OIHPs, such as MAPbBr₃ and CsPbBr₃, in the selective photo-oxidation of benzyl alcohol.²⁵ Comparable conversions are found on MAPbBr₃/TiO₂ and CsPbBr₃/TiO₂ composites, as summarized in Table 2-S3. These results prove that the described photocatalytic strategy reported here is generic. Similar experiments on material involving iodine, MAPbI₃ and MAPbI₃/TiO₂, however, were unsuccessful due to photo-oxidation of I⁻ to form I₃⁻ and the Pb-I bond breaking and formation Pb-O bonds by oxygen intercalated in perovskite photocatalyst.^{20,21,26,27}

Next, we shine light on the photophysical benefit of implementing a hybrid system – over its pure counterparts – by examining their important optical properties. Figure 2-3A shows the pronounced effect

of TiO₂ on the steady-state photoluminescence (PL) spectra of FAPbBr₃. Pure FAPbBr₃ exhibits the known weak PL emission centered around 560 nm, with a high energy shoulder near 545 nm we attribute the presence of smaller FAPbBr₃ nanocrystals (see Figure 2-S2).^{28,29} On the other hand, 15% FAPbBr₃/TiO₂ shows a blue-shifted PL emission peaking at 545 nm, at the same position as nanocrystalline FAPbBr₃ (see Figure 2-S7), assigned to smaller crystallites with a larger bandgap (see Figure 2-S8).^{24,28} This is consistent with the DRS and SEM results. More vividly, the PL intensity and PL quantum yield (PLQY) of FAPbBr₃/TiO₂ (PLQY=10.4%) is observed to increase significantly relative to pure FAPbBr₃. In the presence of charge consuming photocatalytic reactions such as the oxidation of benzyl alcohol, the luminescence intensity strongly reduces (Figure 2-S9).

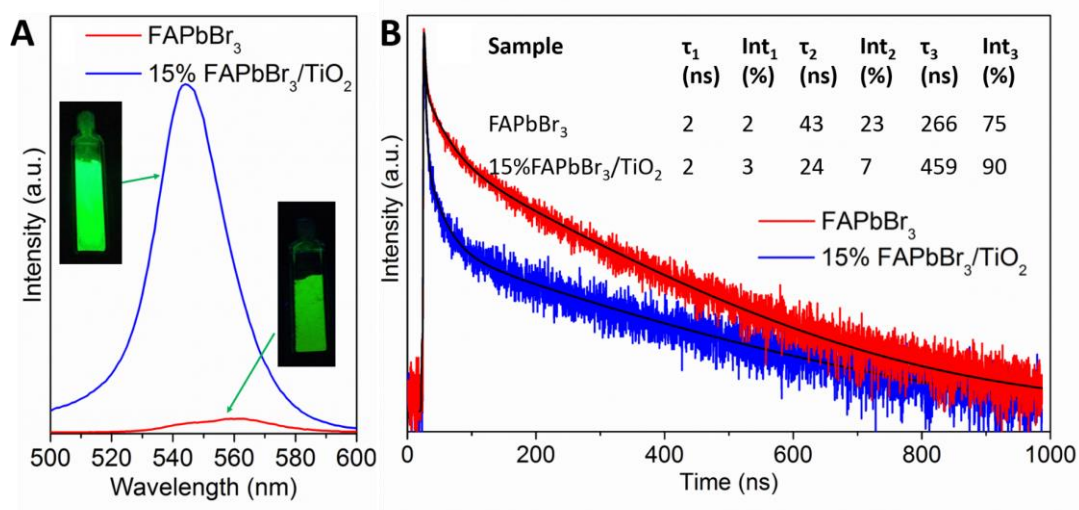
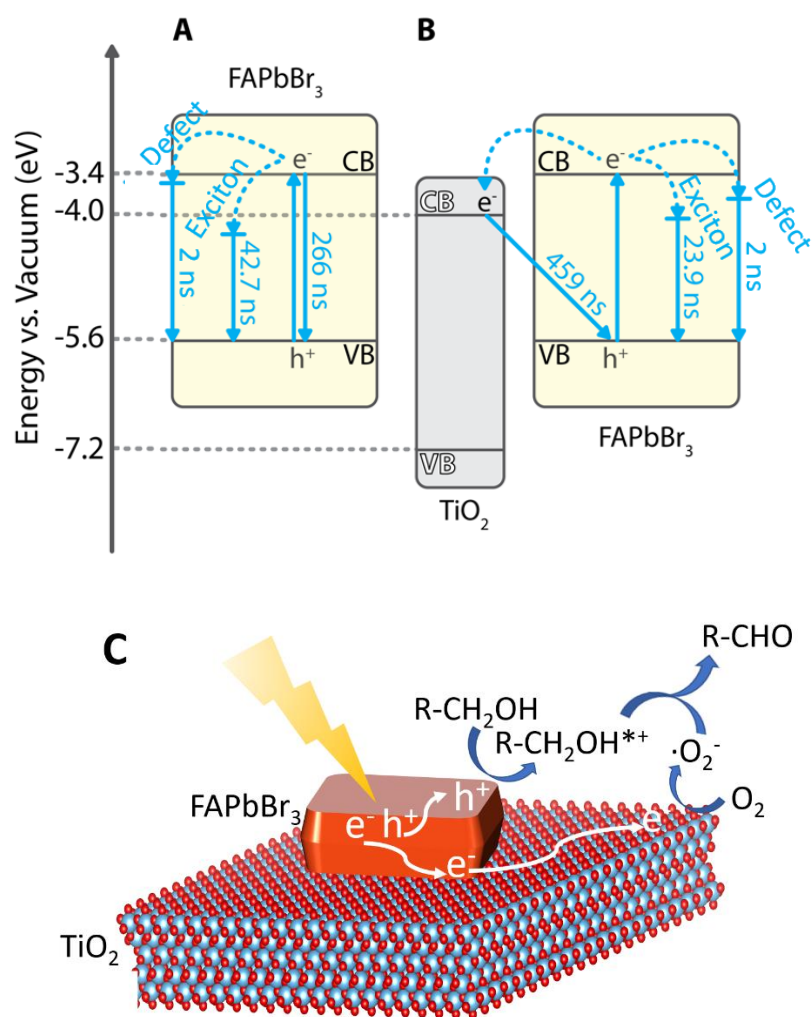


Figure 2-3. (A) Steady-state PL spectra and (B) PL decay spectra of the prepared FAPbBr₃ and 15% FAPbBr₃/TiO₂, including the corresponding multiexponential fitting parameters.

Time-resolved PL analysis is employed to unravel the charge carrier dynamics in the materials' solid state, as shown in Figure 2-3B. The PL decays kinetics of FAPbBr₃ and 15% FAPbBr₃/TiO₂ are agreeably fit with a three-exponential decay function, with their analyzed fit parameters contained in the inset; for completeness, a complete list of parameters used appears in Table 2-S4. Three recombination lifetimes are assigned to distinct processes; trap-assisted (τ_1), exciton (τ_2) and free-carrier (τ_3).²⁴ Note that the difference in charge dynamics between the two decays in Figure 2-3B resides mainly in the exciton and free-carrier recombination, in that the contribution of the former is reduced from 23% in FAPbBr₃ to 7% in FAPbBr₃/TiO₂ while speeding up from 42.7 ns to 23.9 ns. Conversely the free-carrier contribution increased from 75% in FAPbBr₃ to 90% for the FAPbBr₃/TiO₂ hybrid system, while τ_3 is extended from 266

ns to 459 ns, respectively. The suppressed exciton recombination and shorter lifetime indicates exciton dissociation at the FAPbBr₃/TiO₂ interface, a physical feature used to efficiently extract electrons in solar cell devices.^{1,30} The extraction of electrons to TiO₂ leaves holes in the FAPbBr₃, increasing free-carrier PL emission, aligning with our previous observations. Moreover, the ratio of free-carrier emission (90%) in PL decay is in line with a PL intensity drop in toluene after adding benzyl alcohol, indicating the free carriers to be involved in the photocatalytic reaction. During the benzyl alcohol photo-oxidation process, the photogenerated charge carriers are separated at the interface between TiO₂ and FAPbBr₃ and consumed in reactions, thus reducing the PL emission due to the electron-hole recombination. In addition, the extended free carrier lifetime is favorable for the interfacial transfer of carriers to reactive substrates to achieve a higher photo-activity.³¹ Under light irradiation, this composite forms a long lifetime excitation state to carry out the photoconversion from alcohol to aldehyde. In building a clear picture of how the photocatalytic behavior is so dramatically enhanced for the hybrid system, the different recombination pathways described above are summarized and identified in Scheme 2-1A and B.



Scheme 2-1. The experimentally supported mechanistic energy diagram of photo-induced charge transfer in (A) FAPbBr₃ and (B) FAPbBr₃/TiO₂.^{26,32} (C) Corresponding schematic of the proposed selective photocatalytic benzyl alcohol to benzaldehyde oxidation process over the FAPbBr₃/TiO₂ hybrid.

To further support this model, electron spin resonance (ESR) spectroscopy was performed to identify the generated reactive active oxygen species under solar light irradiation with 5,5-dimethyl-pyrroline N-oxide (DMPO) is used as the trapping agent (Figure 2-4A). In dark, only negligible DMPO- $\cdot\text{O}_2^-$ signals were recorded.³³ When excited by solar light irradiation, however, the ESR signals of $\cdot\text{O}_2^-$ species in FAPbBr₃ increase significantly, indicating that photo-generated electrons in FAPbBr₃ reduce O₂ to $\cdot\text{O}_2^-$. Besides this $\cdot\text{O}_2^-$ species, the ESR spectra for the TiO₂ and FAPbBr₃/TiO₂ hybrid show an additional signal coming from

the nitroxide radical which is formed by the light-induced cleavage of the N-C bond and the ring opening of DMPO- $\cdot\text{O}_2^-$ adduct.³⁴ Because of the CB alignment, photo-generated electrons in FAPbBr₃ can be efficiently funneled into TiO₂, as evidenced by our PL results. Therefore, more nitroxide radicals are generated in FAPbBr₃/TiO₂, indicating more charge carriers are transferred to TiO₂, leading to improved photocatalysis efficiency. In addition, the evacuation of photo-generated electrons from FAPbBr₃ to TiO₂ leaves densely populated photo-generated holes in FAPbBr₃ that are available for oxidation reactions. We summarize the mechanism for the organic transformation over FAPbBr₃/TiO₂ in Scheme 1: upon solar light illumination, electrons and holes are generated in FAPbBr₃ and electrons are injected into TiO₂ to reduce the molecular oxygen absorbed on TiO₂ into $\cdot\text{O}_2^-$ species, whereas the photo-generated holes remain in FAPbBr₃ and oxidize the benzylic alcohol substrates to carbocations. The carbocations react with $\cdot\text{O}_2^-$ species to produce the final product, in corresponding to aldehydes.

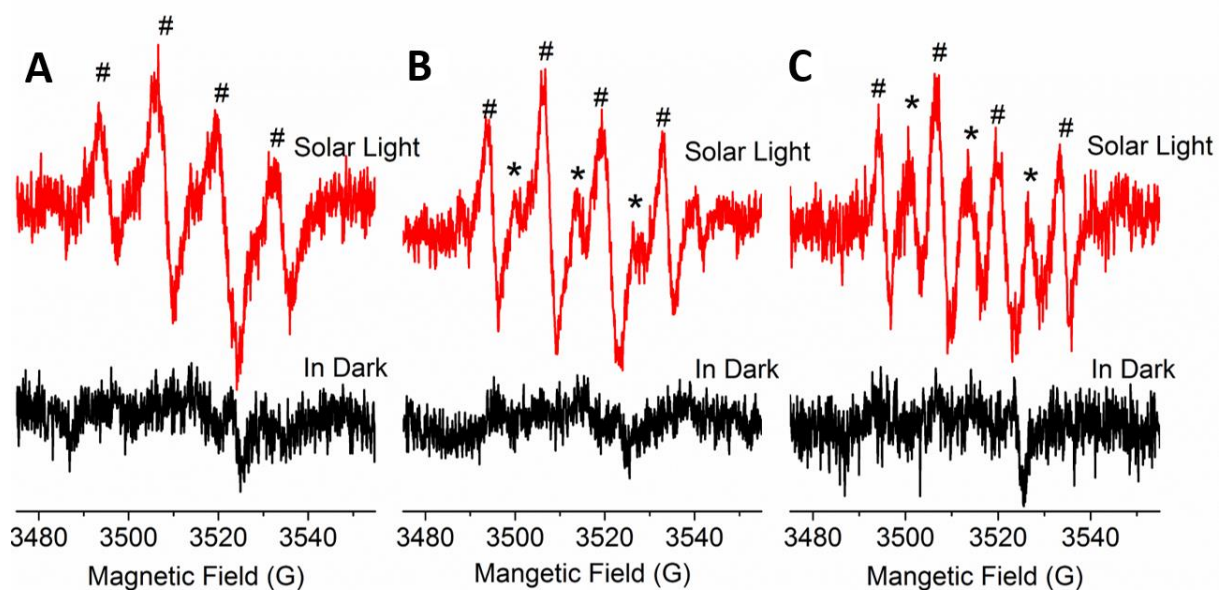


Figure 2-4. DMPO-trapped (#) superoxide radical and (*) Nitroxide-like radical EPR spectra of (A) FAPbBr₃, (B) TiO₂ and (C) 15% FAPbBr₃/TiO₂ dispersed in toluene.

2.3 Conclusion

In summary, the band alignment in the FAPbBr₃/TiO₂ composites facilitates the efficient and highly selective photocatalytic oxidization of benzylic alcohols into aldehydes. By funneling the photo-generated electrons from the perovskite into TiO₂, an excellent photoactivity and a more than 4-fold enhanced in photocatalytic efficiency were realized. This work sheds light on applications of OIHP materials for broader

photocatalytic reactions, not only reduction but also oxidation. We suggest an improved cyclability of such systems can involve an appropriate stabilizing capping agent and conclude that these results ultimately widened the pallet for commercially viable photocatalytic semiconductor systems, using OIHPS/TiO₂ hybrid composites.

2.4 Experiment section

Materials

Anatase TiO₂ and PbBr₂ was purchased from Aldrich and FABr were purchased from TCI. All chemicals were used without further purification.

Sample Preparation

Formamidinium lead bromide was synthesized by the room-temperature antisolvent precipitation method. FABr and PbBr₂ were dissolved in 10 mL of N,N-Dimethylformamide (DMF) in 1:1 molar ratio, to make a 1M precursor-solution. The precursor-solution was added dropwise into a vigorously stirred 5 ml toluene solution. The mixture was kept stirred at room temperature overnight, resulting in an orange-red suspension. The suspension was then washed 3 times with toluene and dried in a vacuum oven at 80° C.

The series of X% FAPbBr₃/TiO₂ samples (where X is equal to the wt%) were synthesized by the same method. In a typical experiment, 100 mg anatase TiO₂ was first added to 5 ml toluene solution. Then, 0.03 ml precursor-solution was added dropwise into the vigorously stirred TiO₂ toluene suspension. The mixture was kept stirring at room temperature overnight. The suspension was then washed with toluene for 3 times by centrifugation and dried in vacuum oven at 80° C to produce the samples referred to as 15% FAPbBr₃/TiO₂ (wt%).

Nano-FAPbBr₃ was synthesized by the same method. In a typical experiment, 0.02 mmol of PbBr₂ and 0.02 mmol of FABr were dissolved in 1 ml DMF. The precursor-solution was added into the vigorously stirred 5 ml toluene solution with 9.4 µl of oleylamine and 64.11 µl of oleic acid. The mixture was kept stirring at

room temperature for 5 minutes. The suspension was then washed 3 times with toluene (centrifugation at 7000 rpm for 5 minutes) and dried in vacuum oven at 80° C.

Sample Characterization

X-ray diffractometry (XRD) measurements were performed on a Stoe X-ray diffractometer using Cu K α 1 radiation ($\lambda = 1.5406 \text{ \AA}$). Scanning electron microscopy (SEM) images of samples were taken with a FEI-Q FEG250 system. X-ray photoelectron spectroscopy (XPS) data were recorded on a VG ESCALAB XPS System with a monochromatized Al K α X-ray sources (15 kV, 200 W 500 μm pass energy = 20 eV). All binding energies were referenced to the C1s peak at 284.6 eV of surface adventitious carbon. Electron spin resonance spectra were obtained over Bruker ESP 300 E electron paramagnetic resonance spectrometer. The optical absorption spectra of the samples were studied by the Lambda-950 UV-vis spectrometer. The steady-state photoluminescence was recorded on an Edinburgh FLS980, from 500 to 600 nm with 1 nm increments and 1 s integration time, under an excitation wavelength of 395 nm. Fluorescence lifetime data was recorded on a home-built confocal FLIM microscope. Emission from a pulsed 485-nm laser diode (LDH-D-C-485, Picoquant, Berlin, Germany) was cleaned up (Chroma ET485/20x, F49-482, AHF Analysentechnik, Tübingen, Germany) and the laser pulsing was set to 1 MHz (PDL 828 Sepia2, Picoquant). The laser was coupled into a single-mode polarization maintaining optical fiber (PMC-400Si-2.6-NA012-3-APB-150-P, Schäfter+Kirchhoff GmbH, Hamburg, Germany) using a 60FC-4-RGBV11-47 fiber coupler (SuK). Light was collimated using a collimator with xyz adjustable lens (60FC-L-4-RGBV11-47, (SuK), the linear polarization cleaned up (CCM1-PBS251, Thorlabs GmbH, Dachau, Germany) and light was reflected via a 3-mm thick polychroic mirror (Chroma zt405/488/561/640rpc, F73-410, AHF) into a galvanometric mirror scanner (TILL Yanus IV digital scanner, FEI Munich, Gräfelfing, Germany) that was connected to the back port of the microscope body (IX71, Olympus Belgium, Berchem Belgium). Imaging was controlled via a home-written software (C#, Microsoft Visual Studio®). Inside the microscope body the light was reflected upwards (3-mm thick Full Reflective Ag Mirror, F21-005, AHF, mounted in a TIRF Filter Cube for BX2/IX2, F91-960, AHF) to the objective (UPLSAPO-60XW, Olympus). Sample emission transmitted through the polychroic mirror was focussed through a 50- μm pinhole (P50S, Thorlabs) via an achromatic lens (AC254-150-A-ML, Thorlabs) and collimated again (AC254-50-A-ML, Thorlabs). After collimation, the emission was reflected on (H560LPXR, F48-559, AHF) and transmitted through (H507LPXR, F48-507) two dichroic mirrors, and emission was filtered (HQ 525/50, Chroma) and focused (AC254-50-A-ML, Thorlabs)

on an avalanche photodiode (τ -SPAD, Picoquant). The detector was connected to a time-correlated single photon counting (TCSPC) device (Hydraharp 400, Picoquant) and powered using a power supply (DSN-102, Picoquant). The laser powers used was 0.15 nW, measured between the polychroic mirror and the galvo (LabMax Top, Coherent, Santa Clara, California, USA)(about 40% reached the sample) that correspond to 50 mW/cm² (taking into account the size of the focal spot and percentage of laser that actually reaches the sample). Data was loaded in the PAM software (<https://pam.readthedocs.io>) written in MATLAB (The MathWorks, Eindhoven, The Netherlands). Instrument response functions (IRF) were recorded by removing the emission filter and imaging the reflection of the laser on the coverslip surface.

Photocatalytic Activity Measurements

All photocatalytic reactions were conducted in a 20 mL quartz reactor and with a magnetic stirring rod (500 rpm). The specific procedure was as follows: 0.01 g photocatalyst, 0.1 mmol benzyl alcohol and 2.5 mL toluene prior to being saturated with molecular oxygen were loaded into the reactor and then the whole system was sealed up. For phenethyl alcohol, 1-Phenylethanol and 4-fluorobenzyl alcohol, 0.5 mmol of the substrates was dissolved in toluene and saturated with molecular oxygen before transferred into the reactor. The mixture was irradiated with a 150 W Xe lamp with AM 1.5G filter to simulate the solar light spectrum. After irradiation of 8 h, the suspension was centrifuged at 10000 rpm for 10 min and the liquid was analyzed by a Shimadzu GC-2010 equipped with an FID detector and CP Sil-5 column (Figure 2S-11).

The conversion rate and selectivity to product can be calculated by the following formulas:

$$\text{Conversion (\%)}: X = (c_B - c_A)/c_B \times 100$$

and

$$\text{Selectivity (\%)}: S = 100 \times c_P/(c_B - c_A),$$

where c_B and c_A and c_P are the concentration of reactant before and after the reaction, and the amount of target product, respectively.

Turnover Number(TON) and Turnover Frequency(TOF) Calculation

TON= sum of the molar of benzaldehyde in 5 cycles / the molar of perovskite in 10 mg catalyst

2.5 References

- (1) Zhao, Y. X.; Zhu, K. Organic–inorganic hybrid lead halide perovskites for optoelectronic and electronic applications. *Chem. Soc. Rev.* **2016**, *45*, 655-689.
- (2) Lee, M. M.; Teuscher, J.; Miyasaka, T.; Murakami, T. N.; Snaith, H. J. Efficient hybrid solar cells based on meso-superstructured organometal halide perovskites. *Science* **2012**, *338*, 643-647.
- (3) Kazim, S.; Nazeeruddin, M. K.; Gratzel, M.; Ahmad, S. Perovskite as light harvester: a game changer in photovoltaics. *Angew. Chem. Int. Ed.* **2014**, *53*, 2812-2824.
- (4) Yang, W. S.; Park, B. W.; Jung, E. H.; Jeon, N. J.; Kim, Y. C.; Lee, D. U.; Shin, S. S.; Seo, J.; Kim, E. K.; Noh, J. H. *et al.* Iodide management in formamidinium-lead-halide–based perovskite layers for efficient solar cells. *Science* **2017**, *356*, 1376-1379.
- (5) Fujishima, A.; Zhang, X. T.; Tryk, D. A. TiO₂ photocatalysis and related surface phenomena. *Surf. Sci. Rep.* **2008**, *63*, 515-582.
- (6) Park, S.; Chang, W. J.; Lee, C. W.; Park, S.; Ahn, H. Y.; Nam, K. T. Photocatalytic hydrogen generation from hydriodic acid using methylammonium lead iodide in dynamic equilibrium with aqueous solution. *Nat. Energy* **2017**, *2*, 16185.
- (7) Xu, Y. F.; Yang, M. Z.; Chen, B. X.; Wang, X. D.; Chen, H. Y.; Kuang, D. B.; Su, C. Y. A CsPbBr₃ perovskite quantum dot/graphene oxide composite for photocatalytic CO₂ Reduction. *J. Am. Chem. Soc.* **2017**, *139*, 5660-5663.
- (8) Chen, K.; Deng, X. H.; Dodekatos, G.; Tuysuz, H. Photocatalytic polymerization of 3, 4-Ethylenedioxythiophene over cesium lead iodide perovskite quantum dots. *J. Am. Chem. Soc.* **2017**, *139*, 12267-12273.
- (9) Sheldon, R. A.; Arends, I.; Ten Brink, G. J.; Dijkman, A. Green, catalytic oxidations of alcohols. *Acc. Chem. Res.* **2002**, *35*, 774-781.
- (10) Sheldon, R. A.; Arends, I.; Dijkman, A. New developments in catalytic alcohol oxidations for fine chemicals synthesis. *Catal. Today* **2000**, *57*, 157-166.
- (11) Fang, W. H.; Chen, J. S.; Zhang, Q. H.; Deng, W. P.; Wang, Y. Hydrothermalite-supported gold catalyst for the oxidant-free dehydrogenation of benzyl alcohol: studies on support and gold size effects. *Chem. Eur. J.* **2011**, *17*, 1247-1256.
- (12) Yamaguchi, K.; Mizuno, N. Supported ruthenium catalyst for the heterogeneous oxidation of alcohols with molecular oxygen. *Angew. Chem. Int. Ed.* **2002**, *41*, 4538-4542.

- (13) Sheldon, R. A.; Arends, I. Organocatalytic oxidations mediated by nitroxyl radicals. *Adv. Synth. Catal.* **2004**, *346*, 1051-1071.
- (14) Dijkstra, A.; Marino-Gonzalez, A.; Payeras, A. M. I.; Arends, I.; Sheldon, R. A. Efficient and selective aerobic oxidation of alcohols into aldehydes and ketones using ruthenium/TEMPO as the catalytic system. *J. Am. Chem. Soc.* **2001**, *123*, 6826-6833.
- (15) Dess, D. B.; Martin, J. C. Dess, Daniel B., and J. C. Martin. "A useful 12-I-5 triacetoxyperiodinane (the Dess-Martin periodinane) for the selective oxidation of primary or secondary alcohols and a variety of related 12-I-5 species. *J. Am. Chem. Soc.* **1991**, *113*, 7277-7287.
- (16) Mori, K.; Hara, T.; Mizugaki, T.; Ebitani, K.; Kaneda, K. Hydroxyapatite-supported palladium nanoclusters: a highly active heterogeneous catalyst for selective oxidation of alcohols by use of molecular oxygen. *J. Am. Chem. Soc.* **2004**, *126*, 10657-10666.
- (17) Zhan, B. Z.; White, M. A.; Sham, T. K.; Pincock, J. A.; Doucet, R. J.; Rao, K. V. R.; Robertson, K. N.; Cameron, T. S. Zeolite-confined nano-RuO₂: A green, selective, and efficient catalyst for aerobic alcohol oxidation. *J. Am. Chem. Soc.* **2003**, *125*, 2195-2199.
- (18) Tan, H. R.; Jain, A.; Voznyy, O.; Lan, X. Z.; de Arquer, F. P. G.; Fan, J. Z.; Quintero-Bermudez, R.; Yuan, M. J.; Zhang, B.; *et al.* Efficient and stable solution-processed planar perovskite solar cells via contact passivation. *Science* **2017**, *355*, 722-726.
- (19) Liu, F.; Zhang, Y. H.; Ding, C.; Toyoda, T.; Ogomi, Y.; Ripolles, T. S.; Hayase, S.; Minemoto, T.; Yoshino, K.; Dai, S. Y.; *et al.* Ultrafast electron injection from photoexcited perovskite CsPbI₃ QDs into TiO₂ nanoparticles with injection efficiency near 99%. *J. Phys. Chem. Lett.* **2018**, *9*, 294-297.
- (20) Eperon, G. E.; Stranks, S. D.; Menelaou, C.; Johnston, M. B.; Herz, L. M.; Snaith, H. J. Formamidinium lead trihalide: a broadly tunable perovskite for efficient planar heterojunction solar cells. *Energy Environ. Sci.* **2014**, *7*, 982-988.
- (21) Zhumekenov, A. A.; Saidaminov, M. I.; Haque, M. A.; Alarousu, E.; Sarmah, S. P.; Murali, B.; Dursun, I.; Miao, X. H.; Abdelhady, A. L.; Wu, T.; *et al.* Formamidinium lead halide perovskite crystals with unprecedented long carrier dynamics and diffusion length. *ACS Energy Lett.* **2016**, *1*, 32-37.
- (22) Wang, C. C.; Ying, J. Y. Sol-gel synthesis and hydrothermal processing of anatase and rutile titania nanocrystals. *Chem. Mat.* **1999**, *11*, 3113-3120.
- (23) Huang, H. W.; Lin, J. J.; Fan, L. Z.; Wang, X. X.; Fu, X. Z.; Long, J. L. Heteroatomic Ni, Sn clusters-grafted anatase TiO₂ photocatalysts: structure, electron delocalization, and synergy for solar hydrogen production. *J. Phys. Chem. C* **2015**, *119*, 10478-10492.

- (24) Zheng, K. B.; Zidek, K.; Abdellah, M.; Messing, M. E.; Al-Marri, M. J.; Pullerits, T. Trap states and their dynamics in organometal halide perovskite nanoparticles and bulk crystals. *J. Phys. Chem. C* **2016**, *120*, 3077-3084.
- (25) Adinolfi, V.; Peng, W.; Walters, G.; Bakr, O. M.; Sargent, E. H. The Electrical and Optical Properties of Organometal Halide Perovskites Relevant to Optoelectronic Performance. *Adv. Mater.* **2018**, *30*, 1700764.
- (26) Perumal, A.; Shendre, S.; Li, M. J.; Tay, Y. K. E.; Sharma, V. K.; Chen, S.; Wei, Z. H.; Liu, Q.; Gao, Y.; Buenconsejo, P. J. S.; *et al.* High brightness formamidinium lead bromide perovskite nanocrystal light emitting devices. *Sci. Rep.* **2016**, *6*, 36733.
- (27) Yang, Y.; Ri, K.; Mei, A. Y.; Liu, L. F.; Hu, M.; Liu, T. F.; Li, X.; Han, H. W. The size effect of TiO₂ nanoparticles on a printable mesoscopic perovskite solar cell. *J. Mater. Chem. A* **2015**, *3*, 9103-9107.
- (28) Protesescu, L.; Yakunin, S.; Bodnarchuk, M. I.; Bertolotti, F.; Masciocchi, N.; Guagliardi, A.; Kovalenko, M. V. Monodisperse formamidinium lead bromide nanocrystals with bright and stable green photoluminescence. *J. Am. Chem. Soc.* **2016**, *138*, 14202-14205.
- (29) Arora, N.; Dar, M. I.; Hezam, M.; Tress, W.; Jacopin, G.; Moehl, T.; Gao, P.; Aldwayyan, A. S.; Deveaud, B.; *et al.* Photovoltaic and amplified spontaneous emission studies of high-quality formamidinium lead bromide perovskite films. *Adv. Funct. Mater.* **2016**, *26*, 2846-2854.
- (30) Gao, P.; Gratzel, M.; Nazeeruddin, M. K. Organohalide lead perovskites for photovoltaic applications. *Energy Environ. Sci.* **2014**, *7*, 2448-2463.
- (31) Huang, H. W.; Lin, J. J.; Zhu, G. B.; Weng, Y. X.; Wang, X. X.; Fu, X. Z.; Long, J. L. A long-lived mononuclear cyclopentadienyl ruthenium complex grafted onto anatase TiO₂ for efficient CO₂ photoreduction. *Angew. Chem. Int. Ed.* **2016**, *55*, 8314-8318.
- (32) Mei, A. Y.; Li, X.; Liu, L. F.; Ku, Z. L.; Liu, T. F.; Rong, Y. G.; Xu, M.; Hu, M.; Chen, J. Z.; Yang, Y.; *et al.* A hole-conductor-free, fully printable mesoscopic perovskite solar cell with high stability. *Science* **2014**, *345*, 295-298.
- (33) Dvoranova, D.; Barbierikova, Z.; Brezova, V. Radical Intermediates in Photoinduced Reactions on TiO₂ (An EPR Spin Trapping Study). *Molecules* **2014**, *19*, 17279-17304.
- (34) Diaz-Urbe, C. E.; Daza, M. C.; Martinez, F.; Paez-Mozo, E. A.; Guedes, C. L. B.; Di Mauro, E. J. Visible light superoxide radical anion generation by tetra (4-carboxyphenyl) porphyrin/TiO₂: EPR characterization. *Photochem. Photobiol., A* **2010**, *215*, 172-178.

2.7 Supporting information

Supporting Figures

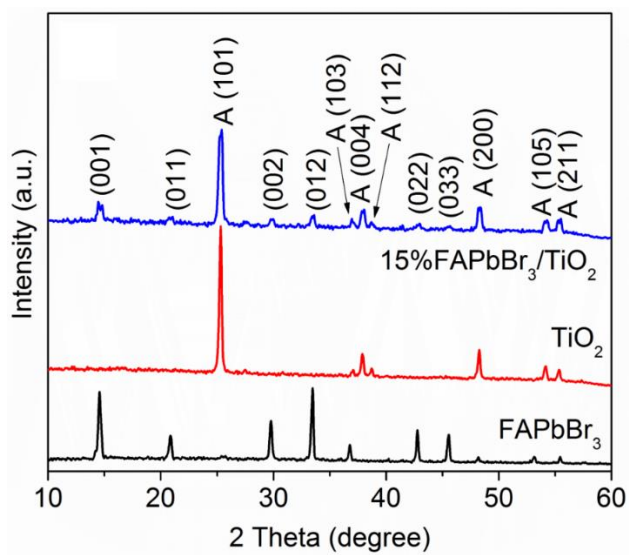


Figure 2-S1. XRD of FAPbBr₃, TiO₂, and 15% FAPbBr₃/TiO₂ prepared via the antisolvent method

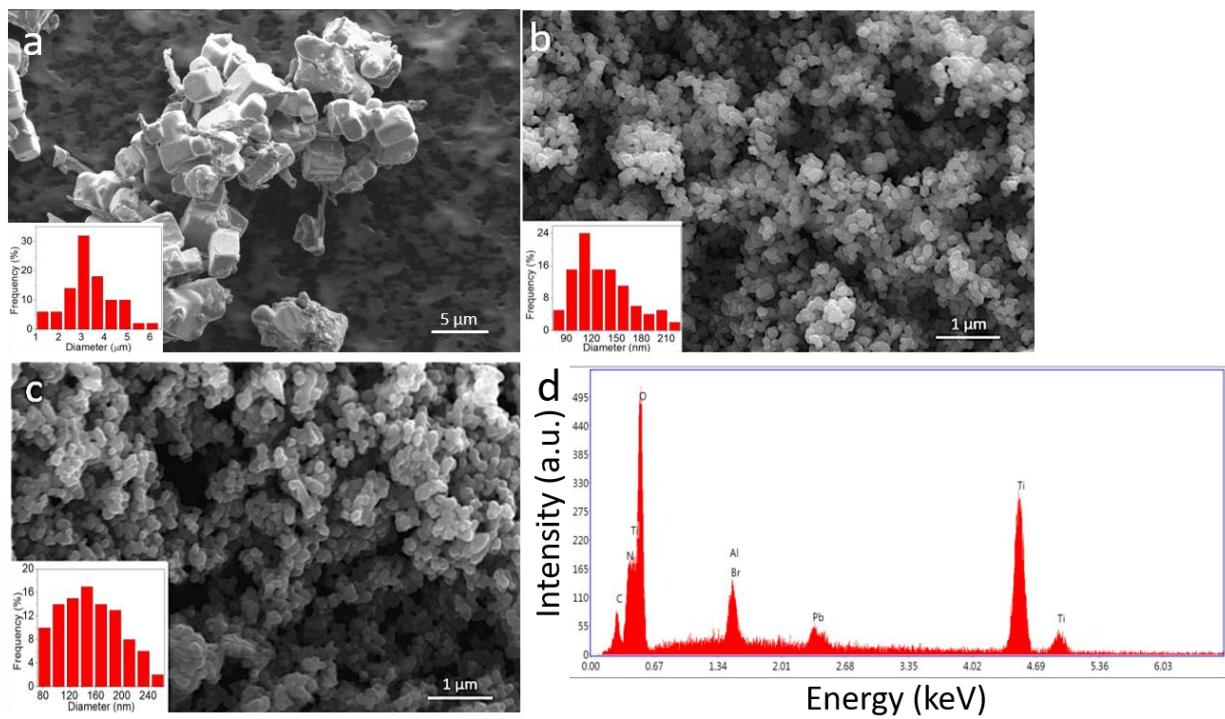


Figure 2-S2. SEM images of (a) FAPbBr₃, (b) TiO₂, (c) FAPbBr₃/TiO₂ and (d) EDX spectrum recorded from the FAPbBr₃/TiO₂.

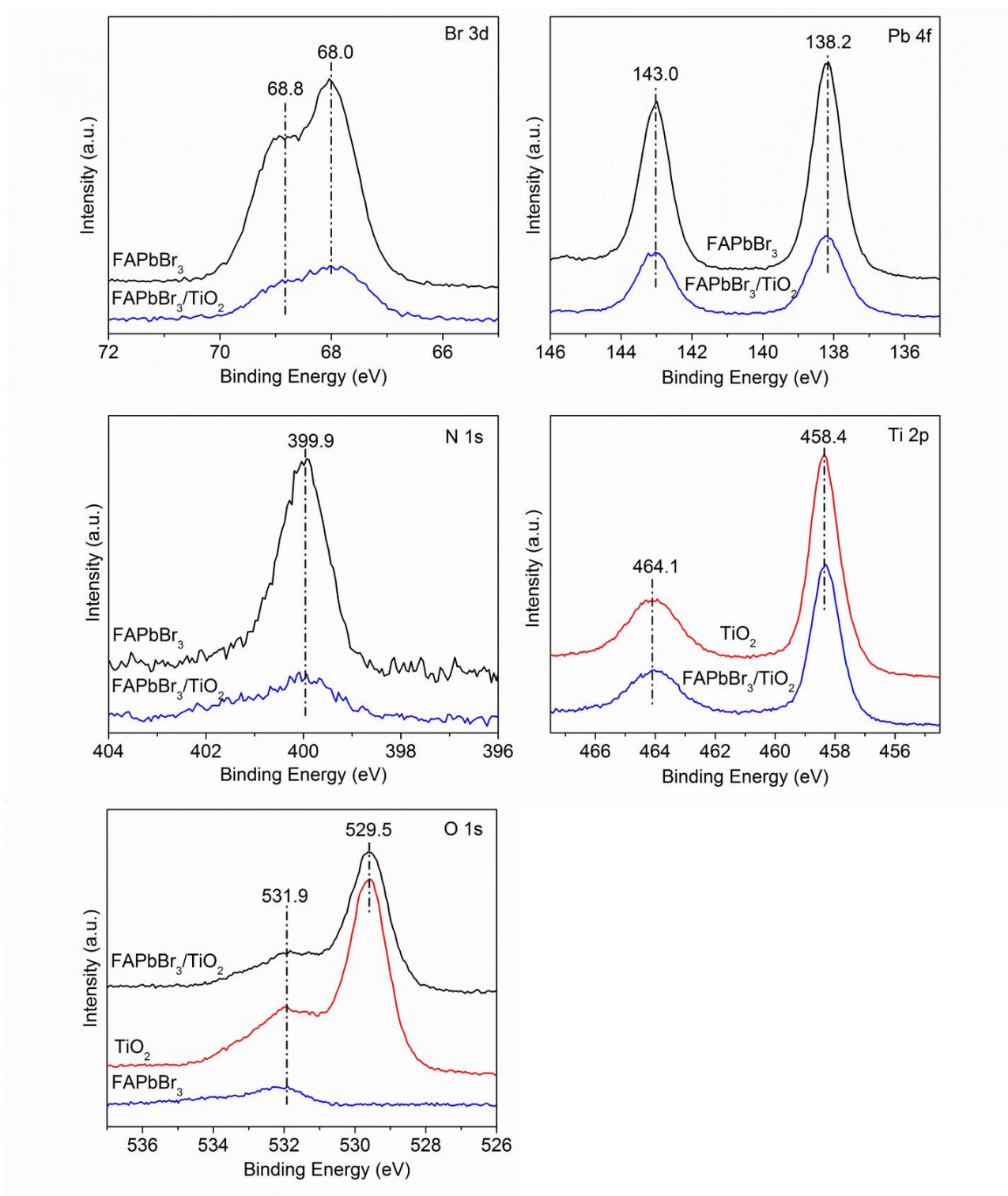


Figure 2-S3. XPS spectra of FAPbBr₃, TiO₂ and FAPbBr₃/TiO₂. Note that spectra have been offset for clarity.

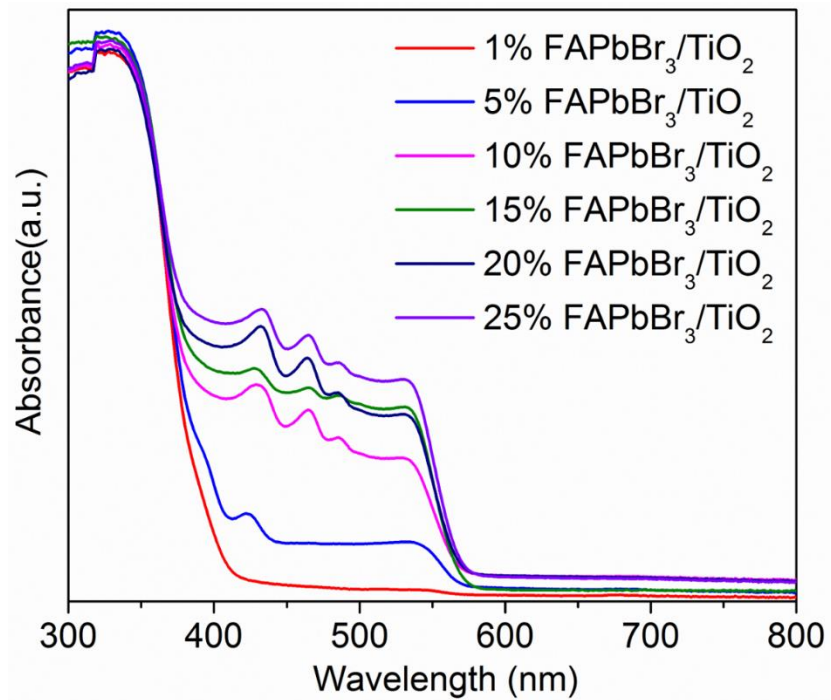


Figure 2-S4. UV-vis DRS spectra of the series of x% FAPbBr₃/TiO₂.

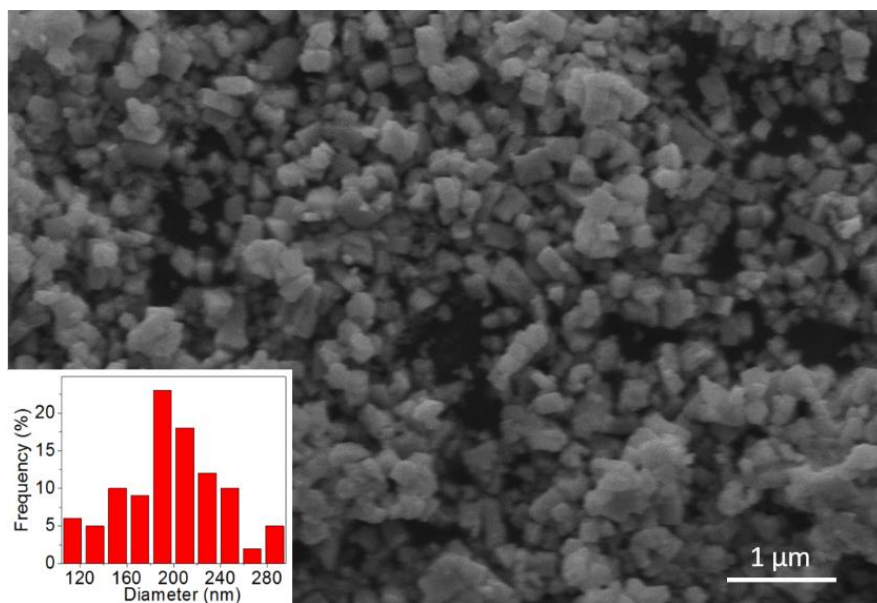


Figure 2-S5. SEM image of nano-FAPbBr₃

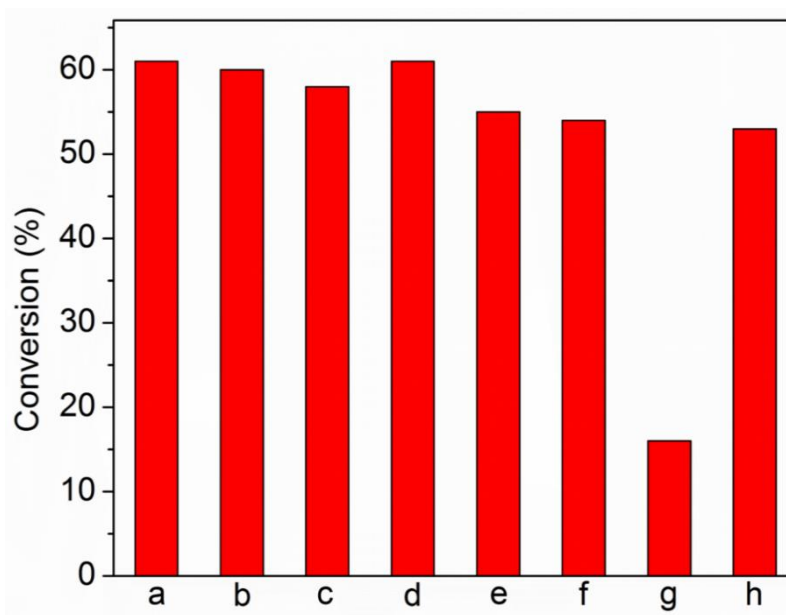


Figure 2-S6. Photocatalytic oxidation of benzyl alcohol over on 15%FAPbBr₃/TiO₂

a) reference performance

activity measured after storing the material:

b) in toluene for 8h in dark,

c) in toluene for 8h under AM1.5G simulated light irradiation,

d) in a mixture of toluene and benzyl alcohol for 8h in dark,

e) in a mixture of toluene and benzyl alcohol for 8h under AM1.5G simulated light irradiation,

f) in a mixture of toluene and benzaldehyde for 8h in dark,

g) in a mixture of toluene and benzaldehyde for 8h under AM1.5G simulated light irradiation,

h) in the solution collected from the experiment performed in g for 8h in dark.

Reaction conditions: benzyl alcohol (0.1 mmol), photocatalysts (0.01 g, including 3 μmol FAPbBr₃ and 0.1 mol TiO₂), solvent of toluene (2.5 mL) saturated with molecular oxygen, AM1.5G simulated light irradiation, irradiation time (8 h).

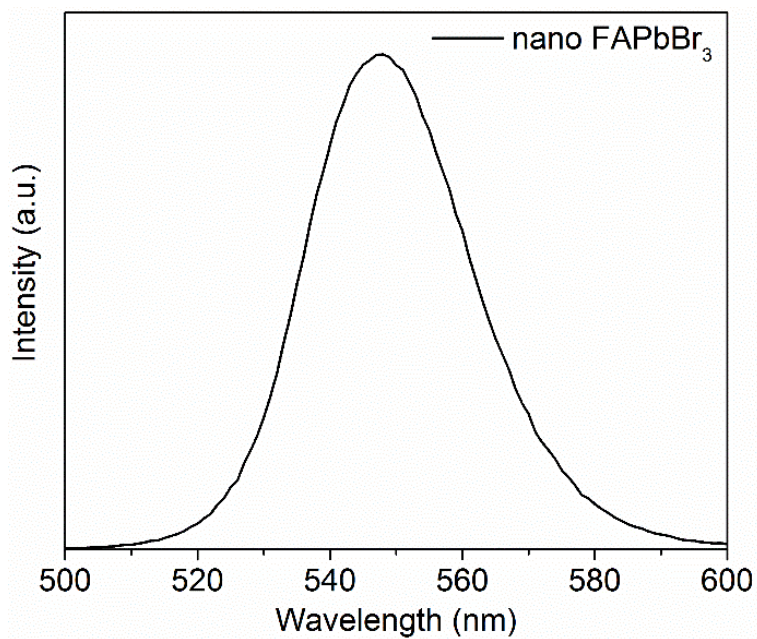


Figure 2-S7. Steady-state PL spectra of nano-FAPbBr₃.

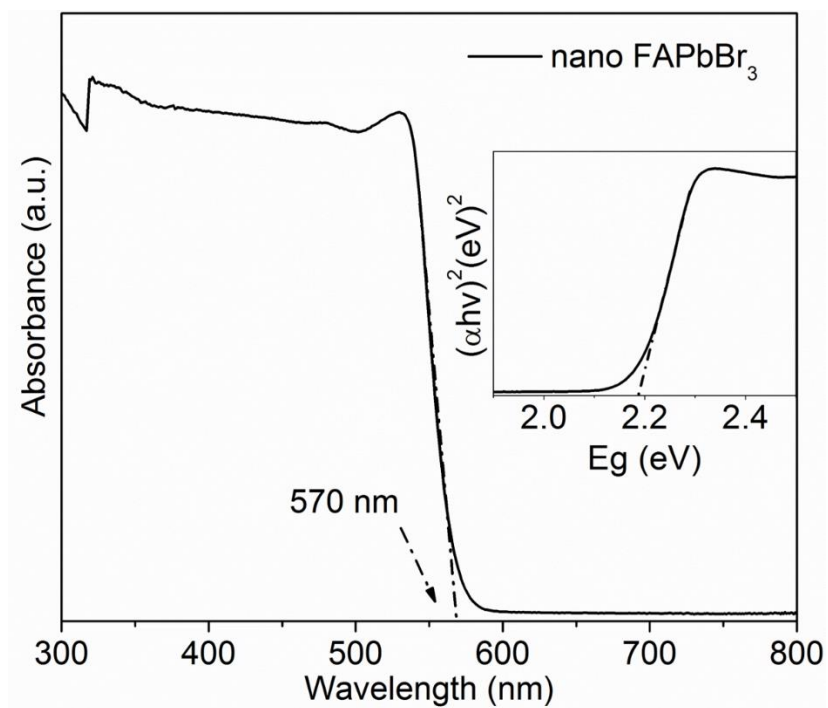


Figure 2-S8. UV-Vis DRS spectra of nano-FAPbBr₃.

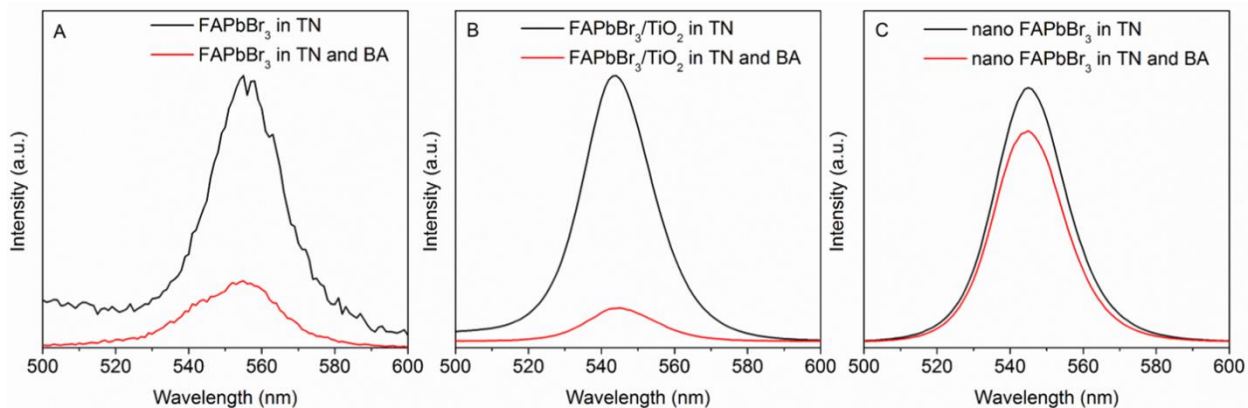


Figure 2-S9. Steady-state PL spectra of (A) FAPbBr₃, (B) FAPbBr₃/TiO₂ and (C) nano-FAPbBr₃ in toluene(TN) before and after benzyl alcohol(BA) added.

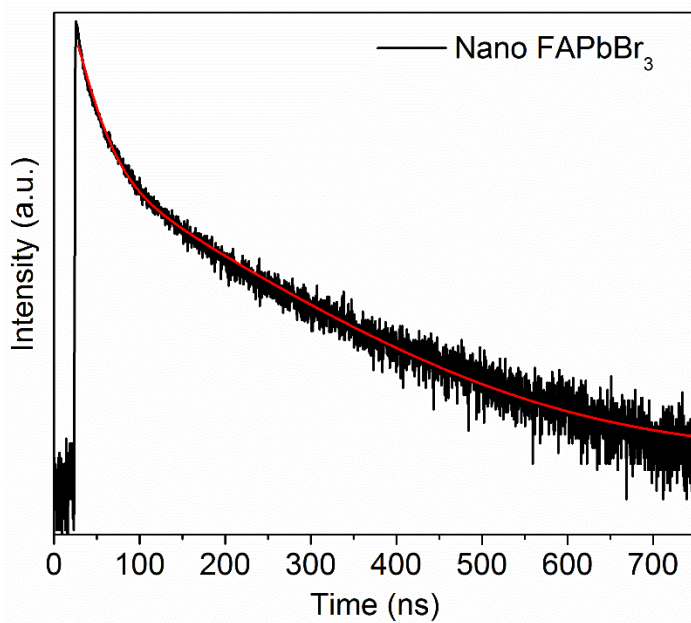


Figure 2-S10. PL decay spectra of the as prepared nano-FAPbBr₃.

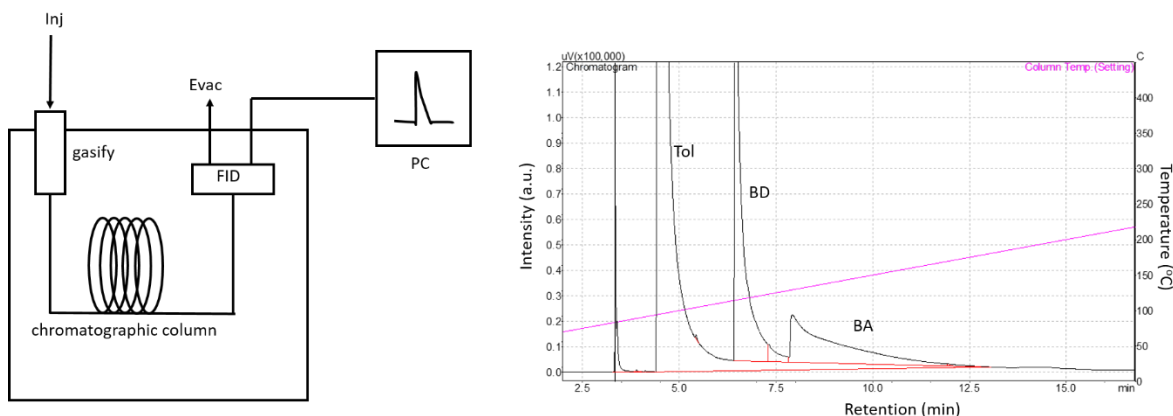


Figure 2-S11. Scheme of GC workflow(left) and an obtained spectrum on benzyl alcohol oxidation(right). The retention of BD and BA is 6.5 min and 8 min, respectively.

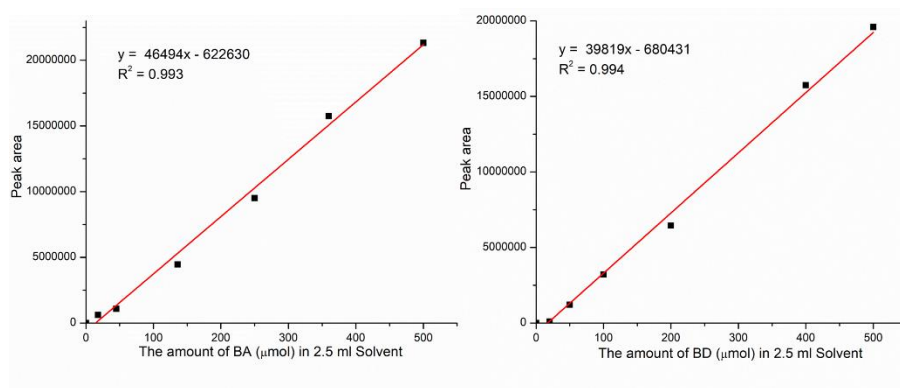
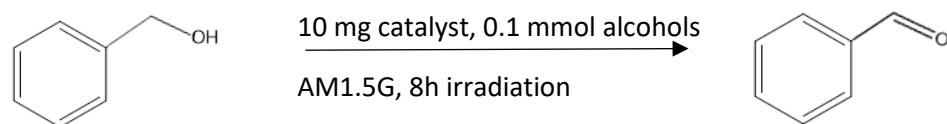


Figure 2-S12. Calibration curve recorded for BA(left) and BD(right) vs Peak area.

Supporting Tables

Table 2-S1. Photocatalytic oxidation of benzylic alcohol over the 15% FAPbBr₃/TiO₂.



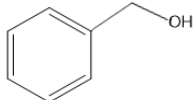
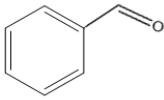
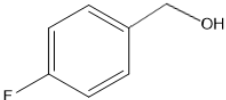
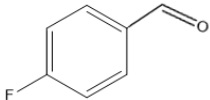
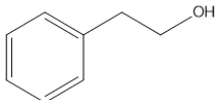
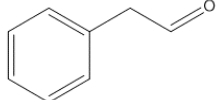
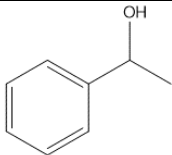
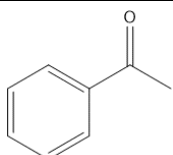
Sample	X (%)	S (%)
15% FAPbBr ₃ /TiO ₂	63	99
TiO ₂	15	95
FAPbBr ₃	15	99
nano-FAPbBr ₃	11	99
15% FAPbBr ₃ /SiO ₂	13	99
15% FAPbBr ₃ /TiO ₂ -M	37	99
Absence of catalyst	0	0
Anatase TiO ₂ ^a	0	0
15% FAPbBr ₃ /TiO ₂ ^a	13	99
15% FAPbBr ₃ /TiO ₂ ^b	0	0

Reaction conditions: benzylic alcohol (0.1 mmol), photocatalysts (0.01 g), in toluene as solvent (2.5 mL) saturated with molecular oxygen, AM1.5G simulated light irradiation (8 h).

^a with 500nm long pass filter,

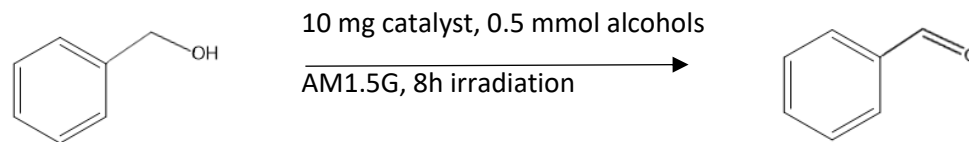
^b without light irradiation.

Table 2-S2. Photocatalytic oxidation of several aromatic alcohols over the 15% FAPbBr₃/TiO₂.

Substrate	Product	X (%)	S (%)
		20	99
		28	70
		15	93
		5	99

Reaction conditions: aromatic alcohols (0.5 mmol), photocatalysts (0.01 g), in toluene as solvent (2.5 mL) saturated with molecular oxygen, AM1.5G simulated light irradiation (8 h). Note that the reaction conditions used here are different to those implemented in the acquiring of data in Figure 2- 2 of the main article, and should be considered only on a relative basis.

Table 2-S3. Photocatalytic Oxidation of Benzyl Alcohols over the 15% FAPbBr₃/TiO₂, 15% MAPbBr₃/TiO₂ and 15% CsPbBr₃/TiO₂.



Sample	X (%)	S (%)
15% FAPbBr ₃ /TiO ₂	20	99
15% MAPbBr ₃ /TiO ₂	24	99
15% CsPbBr ₃ /TiO ₂	16	99
TiO ₂	7	95

Reaction conditions: benzyl alcohol (0.5 mmol), photocatalysts (0.01 g in toluene as solvent (2.5 mL) saturated with molecular oxygen, AM1.5G simulated light irradiation (8 h). Note that the reaction conditions used here are different to those implemented in the acquiring of data in Figure 2- 2 of the main article, and should be considered only on a relative basis.

Table 2-S4. Results of exponential fitting of PL decay traces of FAPbBr₃, 15% FAPbBr₃/TiO₂ and nano-FAPbBr₃.

sample	τ_1 (ns)	Int.1 (%)	A ₁ (%)	τ_2 (ns)	Int.2 (%)	A ₂ (%)	τ_3 (ns)	Int.3 (%)	A ₃ (%)
FAPbBr ₃	2.2	2	56	42.7	23	29	266	75	15
15%FAPbBr ₃ /TiO ₂	2.2	3	73	23.9	7	16	459	90	11
nano-FAPbBr ₃	-	-	-	21	35	77	154	65	23

Here τ indicates the exponential decay time, A represents the amplitude of exponential fitting parameter and Int. value indicates the integrated contribution of the emission from that exponential. These values are including in implemented fit equation: $y = A_1 \cdot \exp(-x/t_1) + A_2 \cdot \exp(-x/t_2) + A_3 \cdot \exp(-x/t_3)$.

Table 2-S5. Photocatalytic oxidation of benzyl alcohol over various photocatalysts under different experimental conditions.

Sample	Reaction condition	generation rate of Benzaldehyde(mmol/g/h)	Reference
FAPbBr ₃ /TiO ₂	150W Xe lamp, AM1.5G filter	1.47	This work
<i>Defect</i> BT	150W Xe lamp, AM1.5G filter	3.75	1
Bi ₂₄ O ₃₁ Br ₁₀ (OH) ₈	450 nm LED, 0.03 W/cm ⁻²	0.39	2
S-vacancy-rich In ₂ S ₃	300W Xe lamp, 420nm cut-off filter	0.71	3
Monolayer HNb ₃ O ₈	300W Xe lamp, 400nm cut-off filter	0.65	4
Au(1.0)/CeO ₂	green LED, 1.7 mW/cm ²	0.80	5
Au/BiOCl-O _v	300W Xe lamp, 420 nm cutoff filter	0.94	6
Au/BiOCl-O _v	365nm UV, 10W	1.4	6
Au/TiO ₂	Sunlight, 11.5 mW/cm ²	0.085	7
Ni/MPA-CdSe	410 nm, monochromatic light	3.0	8
AR/TiO ₂ /TEMPO	visible-light	0.83	9
Bi-TATB	UV-vis light	0.08	10
BiVO ₄	blue LED	0.77	11

GNR@TiO ₂ -4.2-YsS	visible-infrared light ($\lambda > 420$ nm)	0.15	12
CuCl ₂	400 mW/cm, 420- 780 nm light	4.3	13

References

- (1) Huang, H.; Zhou, C.; Jiao, X.; Yuan, H.; Zhao, J.; He, C.; Hofkens, J.; Roeffaers, M.; Long, J.; Steel, J.; Subsurface Defect Engineering in Single-Unit-Cell Bi₂WO₆ Monolayers Boosts Solar-Driven Photocatalytic Performance. *ACS Catal.* **2020**, *10*, 1439-1443
- (2) Dai, Y.; Ren, P.; Li, Y.; Lv, D.; Shen, Y.; Li, Y.; Niemantsverdriet, H.; Besenbacher, F.; Xiang, H.; Hao, W.; Lock, N. Solid Base Bi₂₄O₃₁Br₁₀(OH)₆ with Active Lattice Oxygen for the Efficient Photo-Oxidation of Primary Alcohols to Aldehydes. *Angew. Chem. Int. Ed.* **2019**, *58*, 6265
- (3) Sun, X.; Luo, X.; Zhang, X.; Xie, J.; Jin, S.; Wang, H.; Zheng, X.; Wu, X.; Xie, Y. Enhanced superoxide generation on defective surfaces for selective photooxidation. *J. Am. Chem. Soc.* **2019** *141*, 3797.
- (4) Liang, S.; Wen, L.; Lin, S.; Bi, J.; Feng, P.; Fu, X.; Wu, L. Monolayer HNb₃O₈ for Selective Photocatalytic Oxidation of Benzylic Alcohols with Visible Light Response. *Angew. Chem. Int. Ed.* **2014**, *53*, 2951.
- (5) Tanaka, A.; Hashimoto, K.; and Kominami, H. Preparation of Au/CeO₂ Exhibiting Strong Surface Plasmon Resonance Effective for Selective or Chemoselective Oxidation of Alcohols to Aldehydes or Ketones in Aqueous Suspensions under Irradiation by Green Light. *J. Am. Chem. Soc.* **2012**, *134*, 14526.
- (6) Li, H.; Qin, F.; Yang, Z.; Cui, X.; Wang, J.; Zhang, L. New reaction pathway induced by plasmon for selective benzyl alcohol oxidation on BiOCl possessing oxygen vacancies. *J. Am. Chem. Soc.* **2017**, *139*, 3513.
- (7) Tsukamoto, D.; Shiraishi, Y.; Sugano, Y.; Ichikawa, S.; Tanaka, S.; Hirai, T. Gold Nanoparticles Located at the Interface of Anatase/Rutile TiO₂ Particles as Active Plasmonic Photocatalysts for Aerobic Oxidation. *J. Am. Chem. Soc.* **2012**, *134*, 6309.
- (8) Zhao, L.M.; Meng, Q.Y.; Fan, X.B.; Ye, C.; Li, X.B.; Chen, B.; Ramamurthy, V.; Tung, C.H.; Wu, L.Z. Photocatalysis with quantum dots and visible light: selective and efficient oxidation of alcohols to carbonyl compounds through a radical relay process in water. *Angew. Chem. Int. Ed.* **2017**, *56*, 3020.
- (9) Zhang, M.; Chen, C.; Ma, W.; Zhao, J. Visible - Light - Induced Aerobic Oxidation of Alcohols in a Coupled Photocatalytic System of Dye - Sensitized TiO₂ and TEMPO. *Angew. Chem. Int. Ed.* **2008**, *47*, 9730.

- (10) Zhang, R.; Liu, Y.; Wang, Z.; Wang, P.; Zheng, Z.; Qin, X.; Zhang, X.; Dai, Y.; Whangbo, MH.; Huang, B. Selective photocatalytic conversion of alcohol to aldehydes by singlet oxygen over Bi-based metal-organic frameworks under UV–vis light irradiation. *Appl. Catal. B Environ.* **2019**, 254, 463.
- (11) Unsworth, CA.; Coulson, B.; Chechik, V.; Douthwaite, RE. Aerobic oxidation of benzyl alcohols to benzaldehydes using monoclinic bismuth vanadate nanoparticles under visible light irradiation: Photocatalysis selectivity and inhibition. *J. Catal.* **2017**, 354, 152.
- (12) Li, A.; Zhang, P.; Chang, X.; Cai, W.; Wang, T.; Gong, J. Gold Nanorod@TiO₂ Yolk - Shell Nanostructures for Visible - Light - Driven Photocatalytic Oxidation of Benzyl Alcohol. *Small.* **2015**, 11, 1892.
- (13) Meng, C.; Yang, K.; Fu, X.; Yuan, R. Photocatalytic Oxidation of Benzyl Alcohol by Homogeneous CuCl₂/Solvent: A Model System to Explore the Role of Molecular Oxygen. *ACS Catalysis.* **2015**, 5, 3760.

Chapter 3

C(sp³)–H Bond Activation by Perovskite Solar Photocatalyst Cell

Haowei Huang, Haifeng Yuan, Jiwu Zhao, Guillermo Solís-Fernández, Chen Zhou, Jin Won Seo, Jelle Hendrix, Elke Debroye, Julian A. Steele, Johan Hofkens, Jinlin Long*, Maarten B. J. Roeffaers*

Adapted with permission from ACS Energy Lett. 2019, 4, 1, 203-208

The original article is licensed under the ACS AuthorChoice license, and further permission requests should be directed to the ACS.

<https://pubs.acs.org/doi/abs/10.1021/acsenerylett.8b01698>

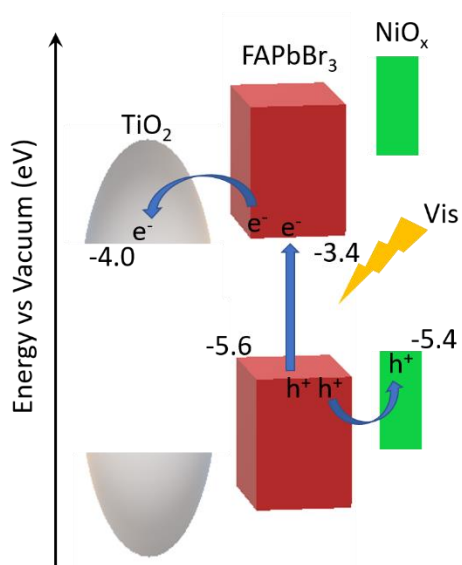
Copyright © 2018 American Chemical Society

Contributions

H.H. and M.B.J.R. designed the project; H.H. conducted the most experiments, including samples preparation, DRS, PL, XRD, TEM, SEM, GC-MS and activity tests; J.Z., G.S.F., and C.Z. performed part of the experiments; J.W.S., E.D., J. H., and J. L. supported the experiments and helped to analyse the results; H.H. analyzed all results and wrote the draft; H. H., H. Y., J. A.S. and M.B.J.R. together revised the manuscript with input from all the authors.

Abstract: Inspired by the efficient perovskite solar cells, we developed a three-component hybrid perovskite-based solar photocatalyst cell - $\text{NiO}_x/\text{FAPbBr}_3/\text{TiO}_2$ - for $\text{C}(\text{sp}^3)\text{-H}$ bonds activation with high selectivity ($\sim 90\%$) and high conversion rates ($3800 \mu\text{mol g}^{-1} \text{h}^{-1}$) under ambient conditions. Time-resolved spectroscopy on our photocatalytic cell reveals efficient exciton dissociation and charge separation, where TiO_2 and NiO_x serve respectively as the electron and hole transporting layers. The photo-generated charge carriers, injected into TiO_2 and NiO_x drive the challenging C-H activation reaction via the synergetic effects of their band alignment relative to FAPbBr_3 . The reaction pathway is investigated by controlling the free radical formation and we find that C-H activation is mainly triggered by hole oxidation. Besides aromatic alkanes, also $\text{C}(\text{sp}^3)\text{-H}$ bond in cycloalkanes can selectively be oxidised. This work demonstrates a generic strategy for engineering high-performance photocatalysts based on the perovskite solar cell concept.

Table of Contents



3.1 Introduction

Direct functionalization of saturated C-H bonds to form high added-value chemicals is one of the most challenging topics in modern chemistry. C(sp³)-H bonds are stable and kinetic stability due to low polarisation of the C-H bond and sterics, making their conversion into C-X bonds, like C-O, very difficult.^{1,2} Much progress has been made in recent decades³⁻⁵, however, the process selectivity and harsh reaction conditions of current C-H activation technologies limit their wide-spread use.³ As such, there are strong desires to develop an easy and energetically favorable route for the efficient conversion of alkanes into value-added products. Photocatalysis provides a promising solution to overcome the challenges in C-H bond activation,⁶ with numerous semiconductors being employed for the selective photo-oxidation of C-H bonds using molecular oxygen as oxidant.⁷⁻¹⁰ However, the photocatalytic performance reported until now falls short of ideal, suffering from narrow optical absorption windows, low charge separation efficiencies and poor product selectivity, owing to over oxidation and/or the need for specific solvents.

Organic-inorganic halide perovskites (OIHPs) typically display strong and broad light absorption and excellent charge transport properties.¹¹ These key physical characteristics suggest their application on photocatalysis within the wider context of light harvesting can be promising.¹²⁻¹⁸ OIHPs can provide a viable option for selective C-H bond activations, with previous work demonstrating FAPbBr₃ and CsPbBr₃ perovskites useful for the selective photo-oxidation of benzylic alcohols, to produce benzaldehyde.^{19,20} The conversion rates using pure perovskite remain low, as a large portion of the photo-generated charges recombine and circumvent the reaction process.

Inspired by efficient perovskite-based solar cells²¹⁻²⁴, we set out to rationally design a more efficient perovskite photocatalyst via superior charge separation by including transporting layers for both electrons (ETL) and holes (HTL). In solar cell devices, efficient light-electricity conversions not only rely on the properties of the perovskite itself but also on the choice of both the ETL, like TiO₂ and HTL, such as Spiro-OMeTAD, PEDOT, NiO_x, etc.²⁵⁻³¹ With regards to choosing an effective ETL, combining FAPbBr₃ and CsPbBr₃ with TiO₂ provides a significant enhancement in photocatalytic benzyl alcohol oxidation.^{19,20} Among HTL materials, we identify cheap and non-toxic p-type NiO_x as a promising choice, given its high charge carrier mobility and structural stability.³¹ Furthermore, nickel oxides and complexes are widely used in organic synthesis like aerobic epoxidation of alkenes, oxidative dehydrogenation of alkanes to alkenes, Baeyer-

Villiger oxidation and sulfoxidation, and photocatalytic organic transformation.^{32,33} More specifically, Xiao and his co-workers have shown that NiO_x could extract the photo-generated holes from TiO₂ to enhance the oxidation of toluene to benzaldehyde.³³ Specifically, 2D NiO_x sheets offer more coordinatively unsaturated Ni atoms, oxygen vacancies, and defect sites on the surface, being capable of stronger interactions with substrates.³⁴ Further, 2D layered materials have great charge transmission capacities and are widely used in photocatalysis to lengthen the carrier lifetime.³⁵ For these reasons, adopting a similar rational design employed in solar cell devices, our final design is a three-component hybrid 2D NiO_x/FAPbBr₃/TiO₂ nano-composite, which is capable of highly selective and efficient activation of C(sp³)-H bonds in alkanes, using molecular oxygen and simulated solar light (AM1.5G).

3.2 Results

The synthesis of NiO_x, FAPbBr₃, FAPbBr₃/TiO₂ and NiO_x/FAPbBr₃/TiO₂ are shown in the supporting information. XRD and XPS (Figure 3S1-3) results clearly indicate that FAPbBr₃ was prepared in its cubic phase, TiO₂ came as a mixed anatase-rutile phase, and NiO_x was a mixture of NiOOH and Ni(OH)₂ with low crystallinity. A TEM image of our nano-composite is provided in Figure 3-1A, with a high resolution micrograph (HRTEM) in Figure 3-1B. Here we see 2D NiO_x sheets supporting the FAPbBr₃ and TiO₂ nanoparticles which is corresponding to the elemental mapping as shown in Figure 3-S6. In the HRTEM image, lattice fringes with 0.4, 0.35 and 0.22 nm spacing, corresponding to (011) of FAPbBr₃, (101) and (001) facet of TiO₂ respectively, can be identified.^{36,37}

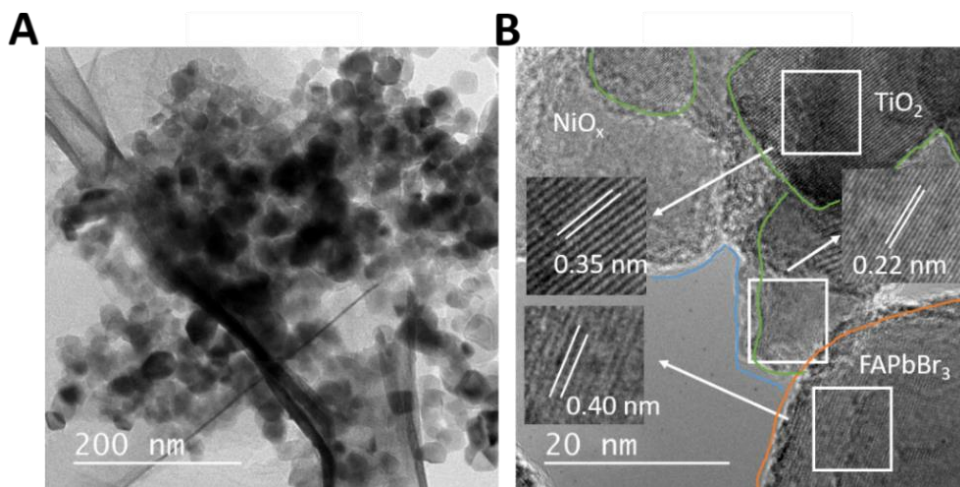


Figure 3-1. TEM (A) and HRTEM (B) image of NiO_x/FAPbBr₃/TiO₂ (Ni/FA/Ti).

The optical absorption spectra of FAPbBr₃/TiO₂ and NiO_x/FAPbBr₃/TiO₂ in Figure 3-2A reveal two band edges near 420 nm and 580 nm, which are assigned to TiO₂ and FAPbBr₃, respectively.¹⁹ Note that the absorption spectra of NiO_x, TiO₂ and FAPbBr₃ are summarized in Figure 3-S7. Over this photonic range, NiO_x barely contributes to the light absorption. A notable Urbach Tail absorption could be observed in NiO_x/FAPbBr₃/TiO₂ as the same as in pure NiO_x, indicating dense defects.³⁸

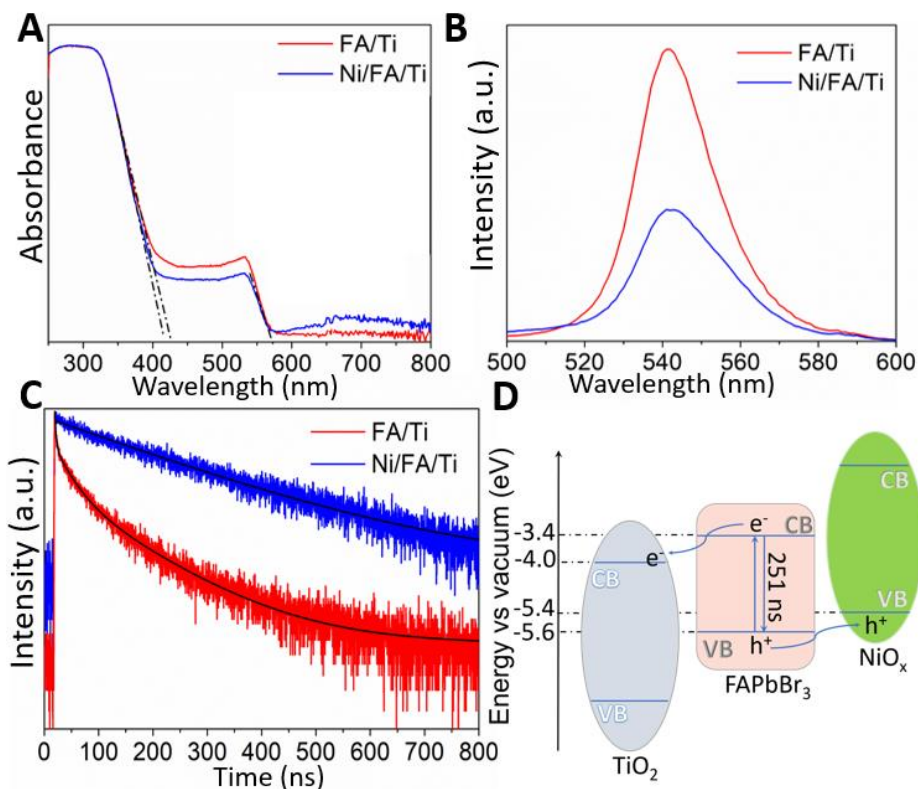


Figure 3-2. UV-Vis DRS spectra (A), Steady-state PL spectra (B) and PL decay spectra (C) of the prepared FAPbBr₃/TiO₂ (FA/Ti) and 5% NiO_x/FAPbBr₃/TiO₂ (Ni/FA/Ti), (D) The experimentally supported mechanistic energy diagram of photo-induced charge transfer in NiO_x/FAPbBr₃/TiO₂.

We next examine the photophysical processes in these materials by steady-state photoluminescence (PL) spectroscopy. FAPbBr₃ presents a typical PL emission around 560 nm (Figure 3-S8). Addition of NiO_x and TiO₂ induces a blue shift in the FAPbBr₃ PL spectra, with a peak at 540 nm in both NiO_x/FAPbBr₃/TiO₂ and FAPbBr₃/TiO₂ (Figure 3-2B), associated with the significantly smaller size of the FAPbBr₃ nanocrystals obtained in these composites.¹⁹ We note that PL intensity is strongly quenched after the addition of NiO_x

onto FAPbBr₃/TiO₂, indicating improved charge separation leading to a reduced radiative recombination or an enhanced non-radiative recombination.^{14,39} Time-resolved photoluminescence (TRPL) decays in Figure 3-2C reveal significant changes in charge dynamics in the hybrid system. Three exponential components are required to fit the FAPbBr₃/TiO₂ TRPL decay in Figure 3-2C, being linked to (1) trap-assisted exciton recombination ($\tau_1=2.2$ ns), (2) exciton recombination ($\tau_2=31.2$ ns), and (3) free carrier recombination ($\tau_3=136$ ns). For completeness, a complete list of parameters used is depicted in Table 3-S1.^{19,40} Interestingly, the introduction of NiO_x does not only strongly reduce the PL intensity but also reshapes the TRPL decay into a mono-exponential decay with a single lifetime value of 251 ns related to free-carrier recombination (τ_3). Moreover, the lifetime of free carriers in NiO_x/FAPbBr₃/TiO₂ is nearly doubled. These findings provide clear evidence for the strong suppression of excitonic recombination. In FAPbBr₃, carriers separate and move to different orientations. At the interface between FAPbBr₃ and NiO_x, and FAPbBr₃ and TiO₂, holes and electrons are extracted evenly from FAPbBr₃ to the NiO_x and TiO₂, respectively.^{19,41,42} First of all, because of the relative band alignment of the three materials, NiO_x, perovskite and TiO₂, the charge separation is much improved at the material interfaces. This exact mechanism is of course exploited in the efficient application of perovskite-based photovoltaics. The efficient charge separation thus leads to a significantly reduced exciton population, followed by the suppression of their radiative contributions. Secondly, besides the separation of excitonic charges at the interfaces, the free electrons and holes are also extracted by NiO_x and TiO₂, for the same reasons of their band alignments relative to the absorbing perovskite. As a consequence of the extraction of charges from the perovskite material to NiO_x and TiO₂, the overall density of charges on the perovskite that are available for charge recombination reduces, resulting in much lower PL emission intensity. Furthermore, as the free carrier population is reduced, promoting a longer time for free carriers to encounter each other and radiatively recombine the PL decay time becomes longer on average *i.e.* lower free carrier population. These findings reveal the efficient separation and extraction pathways for photo-generated charge carriers in the hybrid photocatalyst materials: excitons and free carriers are generated in FAPbBr₃ after photon absorption and the favorable band alignments of the HTL and ETL efficiently separate and extract electrons and holes from the perovskite, suppressing excitonic PL emissions. However, it is worth noting that unlike layer by layer structure in PV, this three-component photocatalyst is heterogeneous. It can be expected that interfaces form between NiO_x and TiO₂ which gives an alternative recombination path for electrons and holes at this interface. In reality, the interface formed in this composition and the carrier

transformation and recombination is a more complex system than the simplified schematic shown in Figure 3-2D.

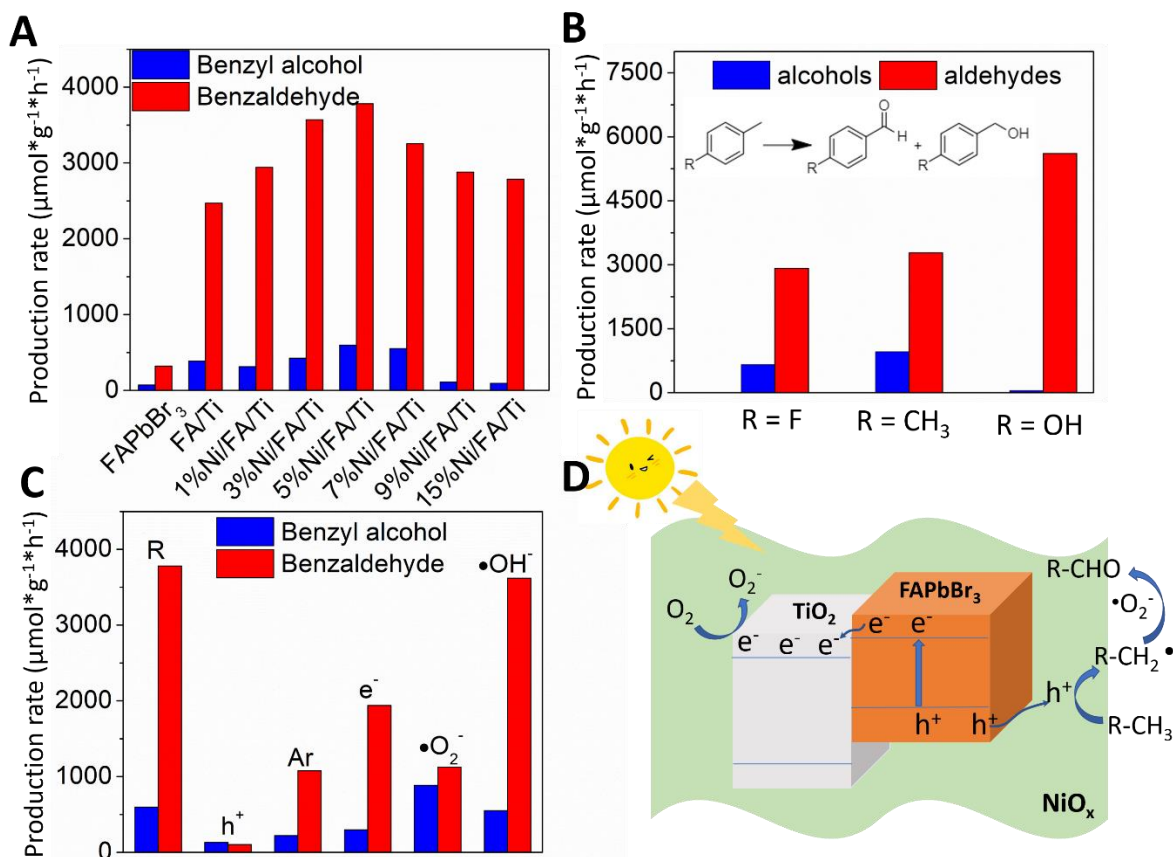


Figure 3-3. (A) Photocatalytic oxidation of C(sp³)-H in Tol over pure FAPbBr₃, FAPbBr₃/TiO₂ and a series of NiO_x/FAPbBr₃/TiO₂ (Ni/FA/Ti) hybrids; (B) Photocatalytic oxidation of C(sp³)-H in substituted toluenes over 5% NiO_x/FAPbBr₃/TiO₂; (C) C(sp³)-H Tol oxidation in the absence or presence of various radical scavengers. (D) Corresponding schematic of the proposed selective photocatalytic conversion of Tol to BD over the NiO_x/FAPbBr₃/TiO₂; detailed reaction scheme can be found in the supporting information. Reaction conditions: photocatalysts (0.01 g), Tol (2.5 mL) saturated with O₂, AM1.5G simulated light irradiation (85 mW/cm²), irradiation time (4 h).

Next, we tested our photocatalysts for the selective photo-oxidation of C(sp³)-H of the methyl group in toluene (Tol) with saturated O₂ and simulated solar light (AM1.5G) at room temperature. The photocatalytic performance under solar light irradiation is summarized in Figure 3-3A and Figure 3-S9. GC-MS was used to check the products, as shown in Figure 3-S10. After 4 hours of illumination, the formation

rates of benzaldehyde (BD) are 320 and 1129 $\mu\text{mol h}^{-1} \text{g}^{-1}$, respectively, for FAPbBr₃ and TiO₂. Additionally, significant amounts of benzyl alcohol (BA) as a side product are produced: 54 and 72 $\mu\text{mol h}^{-1} \text{g}^{-1}$ respectively, resulting in Tol oxidation selectivity to benzaldehyde of 81 % for pure FAPbBr₃ and 95 % for pure TiO₂. Compared with 15 wt% FAPbBr₃/TiO₂ and FAPbBr₃, TiO₂ as ETL results in about 8-fold improved production rates for BD (2470 $\mu\text{mol h}^{-1} \text{g}^{-1}$) and BA (387 $\mu\text{mol h}^{-1} \text{g}^{-1}$). Further integration of an HTL (NiO_x), to prepare NiO_x/FAPbBr₃/TiO₂ solar photocatalyst cell, improved the initial activity of FAPbBr₃ up to 12 times. The best photocatalytic activity being achieved with 5 wt% NiO_x loading with an impressive Tol oxidation rate of 3800 $\mu\text{mol h}^{-1} \text{g}^{-1}$ to BD and 1% external quantum efficiency at 400 nm. The yield of BD is 0.73%, see Table 3-S3. Note that further increasing NiO_x loadings beyond 5 wt% leads to diminishing returns, with reduced conversions driven by competitive light absorption. The optimal 5wt% NiO_x loading is also found to improve the conversion selectivity to BD to 86%. Control experiments using pure NiO_x, NiO_x/FAPbBr₃ and NiO_x/TiO₂ are further compared in Figure 3-S9 and 3-S11. Similar performances (Figure 3-S12) were obtained using purely visible light (> 420 nm). However, the photocatalytic reaction by using visible light shows a lower production rate, which is 10 times less than it obtained with solar light. This indicates that, with solar light irradiation, the additional UV photons can be harvested by FAPbBr₃ as well as by TiO₂ to generate holes and electrons that can react with Tol. The absorption of TiO₂ is only significant below 350 nm compared to the perovskite, as shown in Figure 3-S7.

The remarkable activity for the selective photocatalytic oxidation of C(sp³)-H in Tol offered by the three-component photocatalyst was also confirmed with several substituted toluenes in the conversion to the corresponding aldehydes (Figure 3-3B) which prove the universality of the strategy reported here. The conversion rates for p-fluorobenzaldehyde, p-methylbenzaldehyde and p-hydroxybenzaldehyde are 2915, 3280 and 5610 $\mu\text{mol h}^{-1} \text{g}^{-1}$, with selectivity of 81%, 77% and 99%, respectively. The conversion, yield and selectivity are summarized in Table 3-S2. The material stability during repeated reaction cycles was evaluated. Figure 3-S13 shows the results for 5 wt% NiO_x/FAPbBr₃/TiO₂ following their recycled use during five consecutive 4h reaction cycles. After 5 cycles, the NiO_x/FAPbBr₃/TiO₂ composite retains more than 85 % of its original activity. The slight loss of activity is due to the slow dissolution of FAPbBr₃ in the generated benzaldehyde. At the same time, water as the side product will be generated in this reaction system, which would also affect the stability of perovskite. We remain optimistic that the design of future photocatalyst cells will ultimately resolve this problem via full encapsulation of the perovskite light harvester *i.e.* the generation of a core-shell structure perovskite@HTL/ETL minimizing the contact with the more polar

reaction products, and/or the use of perovskite surface passivating molecules. The photocatalyst remains active for at least five cycles indicating that the lower limit of the turnover number (TON) to be at least 263 and turnover frequency (TOF) for the first five cycles is 13.15 (h^{-1}), see SI for details on the calculation. We also perform a continuous test to check the stability of our sample (see Figure 3-S14). After 20 h irradiation, the photocatalyst still presents a decent activity (more than 85 % of its original activity) and ,as the reaction time increases, the generated benzaldehyde will be further oxidized to benzoic acid.

To elucidate the exact photocatalytic reaction mechanism behind this selective oxidation reaction we investigated in more detail the formation of free radicals that are often involved in photocatalytic organic transformation.^{6,25,43-45} Experiments with specific radical scavengers yield more specific information regarding the role of various redox active species, e.g. ammonium oxalate for holes, potassium persulphate for electrons, 1,4-benzoquinone for $\cdot\text{O}_2^-$ and *t*-butanol for $\cdot\text{OH}$.¹⁰ The effect of these specific radical scavengers on the photocatalytic Tol conversion was tested, with the findings presented in Figure 3-3C. In the presence of ammonium oxalate as strong hole scavenger, the Tol conversion is almost completely prohibited. Scavenging the electrons with $\text{K}_2\text{S}_2\text{O}_8$ reduces the Tol conversion but it does not completely stop the reaction. A similar effect is observed when O_2 is replaced by Ar. Even though the Tol conversion drops in the presence of Ar and $\text{K}_2\text{S}_2\text{O}_8$, the selectivity is maintained. While adding *t*-BuOH has little effect on the photocatalytic Tol oxidation, 1,4-benzoquinone also leads to a reduced conversion and a higher relative BA production. Similar reactions were operated using pristine FAPbBr₃ (Figure 3-S17). These free radical scavenging experiments highlight the vital role of the photogenerated holes to initiate the activation of Tol. These radical experiments open the door to understand the reaction mechanism and give us a guide that the free radical is involved into this reaction. However, to deep insight the reaction mechanism and pathway, more experiments and DFT calculations will be useful to further confirm the reaction mechanism in future.

Therefore, based on the results of PL, TRPL and radical experiments, we propose the following reaction mechanism in Figure 3-3D: (1) Vis light illumination of FAPbBr₃ efficiently generates charge carriers, (2) the presence of ETL (TiO_2) and HTL (NiO_x) efficiently separates the carriers in FAPbBr₃, (3) molecular oxygen adsorbed on TiO_2 is reduced to O_2^- with electrons and the holes in TiO_2 and NiO_x react with Tol to form Tol radicals, a key step for the oxidation of C-H bonds, (4) these Tol radicals react with $\cdot\text{O}_2^-$ to produce the corresponding aldehyde. The generation of BA can be explained by the direct reaction of the Tol radicals

with free O₂ dissolved in Tol to generate BA which can be further oxidized to produce the aldehydes as well.^{16,17}

The highly selective and efficient C(sp³)-H bond oxidation via our rationally designed perovskite solar photocatalytic cell is further tested for the activation of cycloalkanes, using again O₂ under simulated solar illumination (see Table 3-1). Our champion 5% NiO_x/FAPbBr₃/TiO₂ displays a high activity in the selective oxidation of cyclohexane and cyclooctane, with 89 μmol h⁻¹ g⁻¹ and 138 μmol h⁻¹ g⁻¹ cyclohexanone and cyclooctenone, respectively, and with >99% selectivity. The yield is 0.016% and 0.032% for cyclohexanone and cyclooctenone, respectively (see Table 3-S4). These very promising results expand the possibilities for perovskite-based photocatalysts in organic synthesis, given that the dissociation energy of C-H bond in cycloalkanes is larger than that of aromatic methyls.

substrate	Main product	Production rate (μmol g ⁻¹ h ⁻¹)	Selectivity
		89	>99%
		138	>99%

Table 3-1. The results of the oxidation of cycloalkanes with 5%NiO_x/FAPbBr₃/TiO₂. Reaction conditions: photocatalysts (0.01 g), cycloalkanes (2.5 mL) saturated with molecular oxygen, AM1.5G simulated light irradiation, 85 mW/cm², irradiation time (4 h).

3.3 Conclusion

In summary, we have developed a new hybrid photocatalyst inspired by the design principles expressed in the field of perovskite-based solar cells and utilized it for the highly efficient and selective functionalization of C-H bonds in alkanes under relatively mild reaction conditions. A 12-fold enhancement in Tol oxidation is achieved by loading 5 wt% NiO_x onto 15% FAPbBr₃/TiO₂. Detailed time-resolved spectroscopy reveals the efficient photogenerated charge carrier separation in this synergetic system and, considering the radical scavengers, a detailed reaction process for the C(sp³)-H bond activation and selective oxidation is proposed. Most importantly, this work provides bridging the gap between efficient photocatalyst semiconductors and well-established perovskite solar cells, which are currently a prominent feature in the

field of solar energy, paving the way for the rational design of novel perovskite photocatalysts for organic synthesis.

3.4 Experiment section

Materials

Mixed phase TiO_2 , NiCl_2 and PbBr_2 were purchased from Aldrich and FABr was purchased from TCI. It is worth noting that TiO_2 used in this work in Chapters 2 and 3 is from the same supplier but from a different batch have different properties such as particle size, phase. All chemicals were used without further purification.

Sample Preparation

NiO_x sheets were synthesized by hydrothermal method.⁴⁶ In a typical experiment, 0.6 g NiCl_2 and 0.8 g hexamethylenetetramine were dissolved into 60 ml distilled water, then this solution was transferred into an 80 ml Teflon-lined stainless steel autoclave. After the autoclave was maintained at 150 °C for 24 h. A green precipitate was collected and then washed with distilled water for 3 times by centrifugation and dried in a vacuum oven at 80° C to produce the sample referred to as NiO_x . Formamidinium lead bromide was synthesized by the room-temperature antisolvent precipitation method.¹⁹ FABr and PbBr_2 were dissolved in 10 mL of N,N-Dimethylformamide (DMF) in 1:1 molar ratio, to make a 1M precursor-solution. The precursor-solution was added dropwise into a vigorously stirred 5 ml toluene solution. The mixture was kept stirred at room temperature, resulting in an orange-red suspension. The suspension was then washed 3 times with toluene and dried in a vacuum oven at 80° C.

$\text{FAPbBr}_3/\text{TiO}_2$ sample was synthesized by the same method. In a typical experiment, 100 mg TiO_2 was first added to 5 ml toluene solution. Then, 0.03 ml precursor-solution was added dropwise into the vigorously stirred TiO_2 toluene suspension. The mixture was kept stirring at room temperature. The suspension was then washed with toluene for 3 times by centrifugation and dried in a vacuum oven at 80° C to produce the samples referred to as $\text{FAPbBr}_3/\text{TiO}_2$ (the mass ratio of FAPbBr_3 is 15%).

The series of X% NiO_x/FAPbBr₃/TiO₂ (where X is equal to the wt% of NiO_x) samples were synthesized by the same method. In a typical experiment, 100 mg TiO₂ was first added to 5 ml toluene solution. Then, 0.03 ml precursor-solution and 5 mg NiO_x was added into the vigorously stirred TiO₂ toluene suspension. The mixture was kept stirring at room temperature for 1 h. The suspension was then washed with toluene for 3 times by centrifugation and dried in a vacuum oven at 80° C to produce the samples referred to as 5% NiO_x/FAPbBr₃/TiO₂.

Sample Characterization

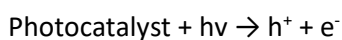
X-ray diffractometry (XRD) measurements were performed on a Stoe X-ray diffractometer using Cu K α 1 radiation ($\lambda = 1.5406 \text{ \AA}$). Scanning electron microscopy (SEM) images of samples were taken with an FEI-Q FEG250 system. Transmission electron microscopy (TEM) images of samples were obtained using a probe-lens corrected JEOL ARM200F operating at 200 kV, equipped with cold-field emission source and Centurion EDX detector. X-ray photoelectron spectroscopy (XPS) data were recorded on a VG ESCALAB XPS System with a monochromatized Al K α X-ray sources (15 kV, 200 W 500 μm pass energy = 20 eV). All binding energies were referenced to the C1s peak at 284.6 eV of surface adventitious carbon. The optical absorption spectra of the samples were studied by the Lambda-950 UV-vis spectrometer. The steady-state photoluminescence was recorded on an Edinburgh FLS980, from 500 to 600 nm with 1 nm increments and 1 s integration time, under an excitation wavelength of 395 nm. Fluorescence lifetime data was recorded on a home-built confocal FLIM microscope. Emission from a pulsed 485-nm laser diode (LDH-D-C-485, Picoquant, Berlin, Germany) was cleaned up (Chroma ET485/20x, F49-482, AHF Analysentechnik, Tübingen, Germany) and the laser pulsing was set to 1 MHz (PDL 828 Sepia2, Picoquant). The laser was coupled into a single-mode polarization maintaining optical fiber (PMC-400Si-2.6-NA012-3-APB-150-P, Schäfter+Kirchhoff GmbH, Hamburg, Germany) using a 60FC-4-RGBV11-47 fiber coupler (SuK). Light was collimated using a collimator with xyz adjustable lens (60FC-L-4-RGBV11-47, (SuK), the linear polarization cleaned up (CCM1-PBS251, Thorlabs GmbH, Dachau, Germany) and light was reflected via a 3-mm thick polychronic mirror (Chroma zt405/488/561/640rpc, F73-410, AHF) into a galvanometric mirror scanner (TILL Yanus IV digital scanner, FEI Munich, Gräfelfing, Germany) that was connected to the back port of the microscope body (IX71, Olympus Belgium, Berchem Belgium). Imaging was controlled via a home-written software (C#, Microsoft Visual Studio®). Inside the microscope body the light was reflected upwards (3-mm thick Full Reflective Ag Mirror, F21-005, AHF, mounted in a TIRF Filter Cube for

BX2/IX2, F91-960, AHF) to the objective (UPLSAPO-60XW, Olympus). Sample emission transmitted through the polychroic mirror was focussed through a 50- μm pinhole (P50S, Thorlabs) via an achromatic lens (AC254-150-A-ML, Thorlabs) and collimated again (AC254-50-A-ML, Thorlabs). After collimation, the emission was reflected on (H560LPXR, F48-559, AHF) and transmitted through (H507LPXR, F48-507) two dichroic mirrors, and emission was filtered (HQ 525/50, Chroma) and focused (AC254-50-A-ML, Thorlabs) on an avalanche photodiode (τ -SPAD, Picoquant). The detector was connected to a time-correlated single photon counting (TCSPC) device (Hydraharp 400, Picoquant) and powered using a power supply (DSN-102, Picoquant). The laser power used was 0.15 nW, measured between the polychroic mirror and the galvo (LabMax Top, Coherent, Santa Clara, California, USA)(about 40% reached the sample) that correspond to 50 mW/cm² (taking into account the size of the focal spot and percentage of laser that actually reaches the sample). Data was loaded in the PAM software (<https://pam.readthedocs.io>) written in MATLAB (The MathWorks, Eindhoven, The Netherlands). Instrument response functions (IRF) were recorded by removing the emission filter and imaging the reflection of the laser on the coverslip surface.

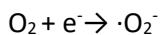
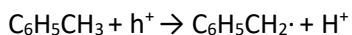
Photocatalytic Activity Measurements

All photocatalytic reactions were conducted in a 20 mL quartz reactor and with a magnetic stirring rod (500 rpm). The specific procedure was as follows: 0.01 g photocatalyst, 2.5 mL toluene prior to being saturated with molecular oxygen were loaded into the reactor and then the whole system was sealed up. The mixture was irradiated with a 150 W Xe lamp with AM 1.5G filter or 420 nm cut-off filter to simulate the solar light spectrum or visible light, respectively. After irradiation of 4 h, the suspension was centrifuged at 10000 rpm for 10 min and the liquid was analyzed by Shimadzu GC-2010 equipped with an FID detector and CP Sil-5 column. Control photoactivity experiments with different radical scavengers, ammonium oxalate, potassium persulfate, tert-butyl alcohol and 1,4-benzoquinone as scavengers for photogenerated holes, photogenerated electrons, hydroxyl radicals, and superoxide radical species, respectively, were performed under similar reaction condition.

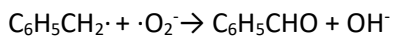
Photocatalytic Reaction Mechanism



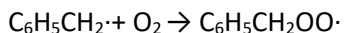
Partial oxidation of toluene and superoxide radical formation



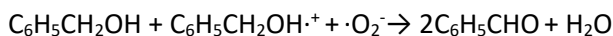
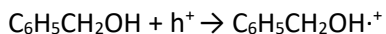
Benzaldehyde formation



Benzyl alcohol formation; with simultaneous formation of benzaldehyde



Benzyl alcohol oxidation to benzaldehyde



Turnover Number(TON) and Turnover Frequency(TOF) Calculation

TON= sum of the molar of benzaldehyde in 5 cycles / the molar of perovskite in 10 mg catalyst

TOF= sum of the molar of benzaldehyde in 5 cycles / (the molar of perovskite in 10 mg catalyst * time)

The apparent quantum efficiency (AQE) at 400 nm

Here, 400 nm bandpass filter is integrated into the light source. We take this as monochromatic light centred at 400 nm, and the light intensity (I) can be measured by a photometer.

$$\text{AQE (\%)} = 100 \times (\text{number of generated BD molecules} \times 4) / (\text{number of incident photons})$$

3.5 References

- (1) Recupero, F.; Punta, C. Free Radical Functionalization of Organic Compounds Catalyzed by N-Hydroxyphthalimide. *Chem. Rev.* **2007**, *107*, 3800-3842.
- (2) Chen, M. S.; White, M. C. Combined Effects on Selectivity in Fe-catalyzed Methylene Oxidation. *Science* **2010**, *327*, 566-571.
- (3) Punniyamurthy, T.; Velusamy, S.; Iqbal, J. Recent Advances in Transition Metal Catalyzed Oxidation of Organic Substrates with Molecular Oxygen. *Chem. Rev.* **2005**, *105*, 2329-2364.

- (4) Kamata, K.; Yonehara, K.; Nakagawa, Y.; Uehara, K.; Mizuno, N. Efficient Stereo- and Regioselective Hydroxylation of Alkanes Catalysed by a Bulky Polyoxometalate. *Nat. Chem.* **2010**, *2*, 478.
- (5) Wang, Y.; Li, H.; Yao, J.; Wang, X.; Antonietti, M. Synthesis of Boron Doped Polymeric Carbon Nitride Solids and Their Use as Metal-Free Catalysts for Aliphatic C–H Bond Oxidation. *Chem. Sci.* **2011**, *2*, 446-450.
- (6) Lang, X. J.; Chen, X. D.; Zhao, J. C. Heterogeneous Visible Light Photocatalysis for Selective Organic Transformations. *Chem. Soc. Rev.* **2014**, *43*, 473-483.
- (7) Yang, D.; Wu, T.; Chen, C.; Guo, W.; Liu, H.; Han, B. The Highly Selective Aerobic Oxidation of Cyclohexane to Cyclohexanone and Cyclohexanol over $V_2O_5@TiO_2$ under Simulated Solar Light Irradiation. *Green Chem.* **2017**, *19*, 311-318.
- (8) Liu, Y.; Chen, L.; Yuan, Q.; He, J.; Au, C.-T.; Yin, S.-F. A Green and Efficient Photocatalytic Route for the Highly-Selective Oxidation of Saturated Alpha-Carbon C–H Bonds in Aromatic Alkanes Over Flower-Like Bi_2WO_6 . *Chem. Commun.* **2016**, *52*, 1274-1277.
- (9) Zhang, P. F.; Wang, Y.; Yao, J.; Wang, C. M.; Yan, C.; Antonietti, M.; Li, H. R. Visible-Light-Induced Metal-Free Allylic Oxidation Utilizing a Coupled Photocatalytic System of G-C₃N₄ and N-Hydroxy Compounds. *Adv. Synth. Catal.* **2011**, *353*, 1447-1451.
- (10) Zhang, Y. H.; Zhang, N.; Tang, Z. R.; Xu, Y. J. Transforming Cds into an Efficient Visible Light Photocatalyst for Selective Oxidation of Saturated Primary C–H Bonds Under Ambient Conditions. *Chem. Sci.* **2012**, *3*, 2812-2822.
- (11) Gao, P.; Gratzel, M.; Nazeeruddin, M. K. Organohalide Lead Perovskites for Photovoltaic Applications. *Energy Environ. Sci.* **2014**, *7*, 2448-2463.
- (12) Wu, Y. Q.; Wang, P.; Zhu, X. L.; Zhang, Q. Q.; Wang, Z. Y.; Liu, Y. Y.; Zou, G. Z.; Dai, Y.; Whangbo, M. H.; Huang, B. B. Composite of $CH_3NH_3PbI_3$ with Reduced Graphene Oxide as a Highly Efficient and Stable Visible-Light Photocatalyst for Hydrogen Evolution in Aqueous HI Solution. *Adv. Mater.* **2018**, *30*, 1704342.
- (13) Park, S.; Chang, W. J.; Lee, C. W.; Park, S.; Ahn, H. Y.; Nam, K. T. Photocatalytic Hydrogen Generation from Hydriodic Acid Using Methylammonium Lead Iodide in Dynamic Equilibrium with Aqueous Solution. *Nat. Energy* **2017**, *2*, 16185.
- (14) Xu, Y. F.; Yang, M. Z.; Chen, B. X.; Wang, X. D.; Chen, H. Y.; Kuang, D. B.; Su, C. Y. A $CsPbBr_3$ Perovskite Quantum Dot/Graphene Oxide Composite for Photocatalytic CO₂ Reduction. *J. Am. Chem. Soc.* **2017**, *139*, 5660-5663.

- (15) Chen, K.; Deng, X. H.; Dodekatos, G.; Tuysuz, H. Photocatalytic Polymerization of 3, 4-Ethylenedioxythiophene over Cesium Lead Iodide Perovskite Quantum Dots. *J. Am. Chem. Soc.* **2017**, *139*, 12267-12273.
- (16) Xu, Y.-F.; Wang, X.-D.; Liao, J.-F.; Chen, B.-X.; Chen, H.-Y.; Kuang, D.-B. Amorphous-TiO₂-Encapsulated CsPbBr₃ Nanocrystal Composite Photocatalyst with Enhanced Charge Separation and CO₂ Fixation. *Adv. Mater. Interfaces.*, **2018**, *5*, 1801015.
- (17) Xu, Y.-F.; Yang, M.-Z.; Chen, H.-Y.; Liao, J.-F.; Wang, X.-D.; Kuang, D.-B. Enhanced Solar-Driven Gaseous CO₂ Conversion by CsPbBr₃ Nanocrystal/Pd Nanosheet Schottky-Junction Photocatalyst *ACS Appl. Energy Mater.* **2018**, *1*, 5083-5089.
- (18) Zhou, L.; Xu, Y.-F.; Chen, B.-X.; Kuang, D.-B.; Su, C.-Y. Synthesis and Photocatalytic Application of Stable Lead-Free Cs₂AgBiBr₆ Perovskite Nanocrystals *Small* **2018**, *14*, 1703762.
- (19) Huang, H.; Yuan, H.; Janssen, K. P. F.; Solís-Fernández, G.; Wang, Y.; Tan, C. Y. X.; Jonckheere, D.; Debroye, E.; Long, J.; Hendrix, J.; *et al* Efficient and Selective Photocatalytic Oxidation of Benzylic Alcohols with Hybrid Organic-Inorganic Perovskite Materials. *ACS Energy Lett.* **2018**, *3*, 755-759.
- (20) Schünemann, S.; Van Gastel, M.; Tüysüz, H. A CsPbBr₃/TiO₂ Composite for Visible-Light Driven Photocatalytic Benzyl Alcohol Oxidation. *Chemsuschem* **2018**, *11*, 2057.
- (21) Brenner, T. M.; Egger, D. A.; Kronik, L.; Hodes, G.; Cahen, D. Hybrid Organic-Inorganic Perovskites: Low-cost Semiconductors with Intriguing Charge-transport Properties *Nat. Rev. Mater.* **2016**, *1*, 150007.
- (22) Kazim, S.; Nazeeruddin, M. K.; Gratzel, M.; Ahmad, S. Perovskite as Light Harvester: a Game Changer in Photovoltaics. *Angew. Chem. Int. Ed.* **2014**, *53*, 2812-2824.
- (23) Yang, W. S.; Park, B. W.; Jung, E. H.; Jeon, N. J.; Kim, Y. C.; Lee, D. U.; Shin, S. S.; Seo, J.; Kim, E. K.; Noh, J. H.; *et al*. Iodide Management in Formamidinium-lead-halide-based Perovskite Layers for Efficient Solar Cells. *Science* **2017**, *356*, 1376-1379.
- (24) Tan, H. R.; Jain, A.; Voznyy, O.; Lan, X. Z.; De Arquer, F. P. G.; Fan, J. Z.; Quintero-Bermudez, R.; Yuan, M. J.; Zhang, B.; Zhao, Y. C.; *et al*. Efficient and Stable Solution-Processed Planar Perovskite Solar Cells via Contact Passivation. *Science* **2017**, *355*, 722-726.
- (25) Qin, P.; Tanaka, S.; Ito, S.; Tetreault, N.; Manabe, K.; Nishino, H.; Nazeeruddin, M. K.; Gratzel, M. Inorganic Hole Conductor-based Lead Halide Perovskite Solar Cells with 12.4% Conversion Efficiency. *Nat. Commun.* **2014**, *5*, 3834.
- (26) Lee, M. M.; Teuscher, J.; Miyasaka, T.; Murakami, T. N.; Snaith, H. J. Organometal Halide Perovskites Efficient Hybrid Solar Cells Based on Meso-superstructured. *Science* **2012**, *338*, 1228604.

- (27) Xiao, Z. G.; Bi, C.; Shao, Y. C.; Dong, Q. F.; Wang, Q.; Yuan, Y. B.; Wang, C. G.; Gao, Y. L.; Huang, J. S. Efficient, High Yield Perovskite Photovoltaic Devices Grown by Interdiffusion of Solution-processed Precursor Stacking Layers. *Energy Environ. Sci.* **2014**, *7*, 2619-2623.
- (28) Yang, Y.; Ri, K.; Mei, A. Y.; Liu, L. F.; Hu, M.; Liu, T. F.; Li, X.; Han, H. W. The Size Effect of TiO₂ Nanoparticles on a Printable Mesoscopic Perovskite Solar Cell. *J. Mater. Chem. A* **2015**, *3*, 9103-9107.
- (29) Jeng, J. Y.; Chen, K. C.; Chiang, T. Y.; Lin, P. Y.; Tsai, T. D.; Chang, Y. C.; Guo, T. F.; Chen, P.; Wen, T. C.; Hsu, Y. J. Nickel Oxide Electrode Interlayer in CH₃NH₃PbI₃ Perovskite/PCBM Planar-Heterojunction Hybrid Solar Cells. *Adv. Mater.* **2014**, *26*, 4107-4113.
- (30) Christians, J. A.; Fung, R. C. M.; Kamat, P. V. An Inorganic Hole Conductor for Organo-Lead Halide Perovskite Solar Cells. Improved Hole Conductivity with Copper Iodide. *J. Am. Chem. Soc.* **2014**, *136*, 758-764.
- (31) You, J.; Meng, L.; Song, T.-B.; Guo, T.-F.; Yang, Y.; Chang, W.-H.; Hong, Z.; Chen, H.; Zhou, H.; Chen, Q.; *et al.* Improved Air Stability of Perovskite Solar Cells via Solution-Processed Metal Oxide Transport Layers. *Nat. Nanotech.* **2015**, *11*, 75.
- (32) Punniyamurthy, T.; Velusamy, S.; Iqbal, J. Recent Advances In Transition Metal Catalyzed Oxidation of Organic Substrates with Molecular Oxygen. *Chem. Rev.* **2005**, *105*, 2329-2364.
- (33) Liu, J.; Li, Y.; Ke, J.; Wang, S.; Wang, L.; Xiao, H. Black NiO-TiO₂ Nanorods for Solar Photocatalysis: Recognition of Electronic Structure and Reaction Mechanism. *Appl. Catal. B Environ.* **2018**, *224*, 705-714.
- (34) Zhao, B.; Ke, X.-K.; Bao, J.-H.; Wang, C.-L.; Dong, L.; Chen, Y.-W.; Chen, H.-L. Synthesis of Flower-like NiO and Effects of Morphology on Its Catalytic Properties. *J. Phys. Chem. C* **2009**, *113*, 14440-14447.
- (35) Luo, B.; Liu, G.; Wang, L. Recent Advances in 2D Materials for Photocatalysis. *Nanoscale* **2016**, *8*, 6904-6920.
- (36) Huang, H. W.; Lin, J. J.; Fan, L. Z.; Wang, X. X.; Fu, X. Z.; Long, J. L. Heteroatomic Ni, Sn Clusters-grafted Anatase TiO₂ Photocatalysts: Structure, Electron Delocalization, and Synergy for Solar Hydrogen Production. *J. Phys. Chem. C* **2015**, *119*, 10478-10492.
- (37) Perumal, A.; Shendre, S.; Li, M. J.; Tay, Y. K. E.; Sharma, V. K.; Chen, S.; Wei, Z. H.; Liu, Q.; Gao, Y.; Buenconsejo, P. J. S.; *et al.* High Brightness Formamidinium Lead Bromide Perovskite Nanocrystal Light Emitting Devices. *Sci. Rep.* **2016**, *6*, 36733.
- (38) Paul, M.; Pal, N.; Bhaumik, A. Mesoporous Nickel-Aluminum Mixed Oxide: a Promising Catalyst in Hydride-Transfer Reactions. *Eur. J. Inorg. Chem.* **2010**, 5129-5134.

- (39) Jing, L. Q.; Qu, Y. C.; Wang, B. Q.; Li, S. D.; Jiang, B. J.; Yang, L. B.; Fu, W.; Fu, H. G.; Sun, J. Z. Review of Photoluminescence Performance of Nano-Sized Semiconductor Materials and Its Relationships with Photocatalytic Activity. *Sol. Energy Mater. Sol. Cells* **2006**, *90*, 1773-1787.
- (40) Zheng, K. B.; Zidek, K.; Abdellah, M.; Messing, M. E.; Al-Marri, M. J.; Pullerits, T. Trap States and Their Dynamics in Organometal Halide Perovskite Nanoparticles and Bulk Crystals. *J. Phys. Chem. C* **2016**, *120*, 3077-3084.
- (41) Liu, F.; Zhang, Y. H.; Ding, C.; Toyoda, T.; Ogomi, Y.; Ripolles, T. S.; Hayase, S.; Minemoto, T.; Yoshino, K.; Dai, S. Y.; *et al.* Ultrafast Electron Injection from Photoexcited Perovskite CsPbI₃ QDs Into TiO₂ Nanoparticles with Injection Efficiency Near 99%. *J. Phys. Chem. Lett.* **2018**, *9*, 294-297.
- (42) Zhu, Z. L.; Bai, Y.; Zhang, T.; Liu, Z. K.; Long, X.; Wei, Z. H.; Wang, Z. L.; Zhang, L. X.; Wang, J. N.; Yan, F.; *Et Al.* High-performance Hole-Extraction Layer of Sol-gel-processed NiO Nanocrystals for Inverted Planar Perovskite Solar Cells. *Angew. Chem. Int. Ed.* **2014**, *53*, 12779-12783.
- (43) Xu, J.; He, S.; Zhang, H. L.; Huang, J. C.; Lin, H. X.; Wang, X. X.; Long, J. L. Layered Metal–Organic Framework/Graphene Nanoarchitectures for Organic Photosynthesis under Visible Light. *J. Mater. Chem. A* **2015**, *3*, 24261-24271.
- (44) Lang, X. J.; Zhao, J. C.; Chen, X. D. Visible-Light-Induced Photoredox Catalysis of Dye-Sensitized Titanium Dioxide: Selective Aerobic Oxidation Of Organic Sulfides. *Angew. Chem. Int. Ed.* **2016**, *55*, 4697-4700.
- (45) Li, X.-H.; Wang, X.; Antonietti, M. Solvent-Free and Metal-Free Oxidation of Toluene Using O₂ and Gc₃n₄ with Nanopores: Nanostructure Boosts the Catalytic Selectivity. *ACS Catal.* **2012**, *2*, 2082-2086.

3.6 Supporting Information

Supporting Figures

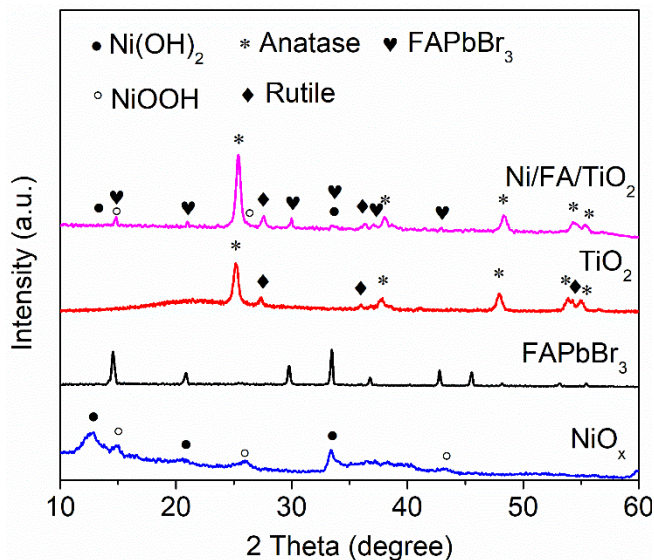


Figure 3-S1. Powder X-ray diffraction (XRD) patterns of NiO_x , FAPbBr_3 , $\text{FAPbBr}_3/\text{TiO}_2$ and $\text{NiO}_x/\text{FAPbBr}_3/\text{TiO}_2$. Here, FAPbBr_3 was prepared in its thermodynamically stable cubic phase and the precipitated TiO_2 came as a mixed anatase-rutile phase.¹ NiO_x showed low crystallinity, possessing a mixture of $\text{Ni}(\text{OH})_2$ and NiOOH nanoparticles with broadened diffraction peaks.²⁻⁴

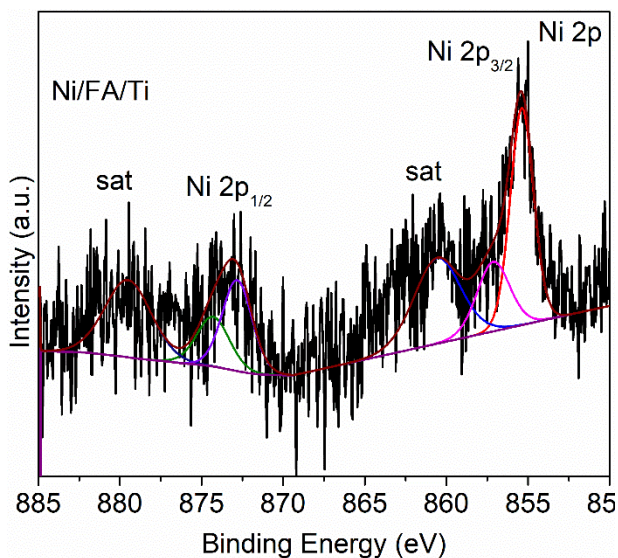


Figure 3-S2. XPS spectra of Ni in NiO_x/FAPbBr₃/TiO₂. XPS further confirmed the composition and chemical state of the synthesized photocatalysts. The high-resolution Ni 2p spectrum (Figure 3-1B) reveals two Ni 2p_{3/2} peak energies: 855.4 eV is the characteristic of the Ni²⁺-vacancy-induced Ni³⁺, Ni(OH)₂ or NiOOH,⁵⁻⁸ and the other peak at 857.2 eV can be attributed to Ni³⁺ ion.⁸ The Ni 2p_{1/2} signal contains two peaks: one at 873.0 eV originating from Ni²⁺ and the second 874.3 eV from Ni³⁺.⁸ Notably, the spin-energy separation of Ni²⁺ is 17.6 eV, corresponding to Ni(OH)₂.⁹ The Ni 2p XPS data coincides nicely with the XRD results, confirming NiO_x to be a mixture of NiOOH and Ni(OH)₂.

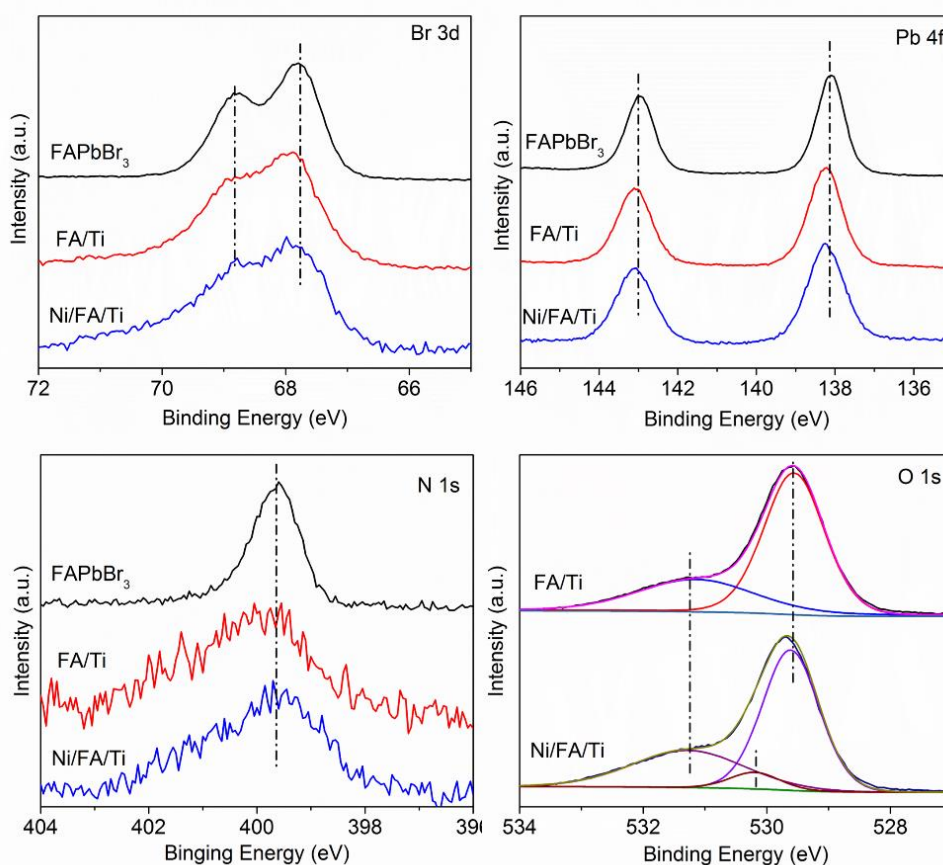


Figure 3-S3. XPS spectra of Br 3d, Pb 4f and N 1s in FAPbBr₃, FAPbBr₃/TiO₂ (FA/Ti) and NiO_x/FAPbBr₃/TiO₂ (Ni/FA/Ti) and O1s in FA/Ti and Ni/FA/Ti. There is no difference in the chemical state of Br, Pb and N. However, in O 1s spectrum, two oxygen contributions are presented in the FAPbBr₃/TiO₂. The peak at 529.5 eV can be assigned to the typical of metal-oxygen bonds Ti-O in TiO₂ and the other peak at 531.3 eV is usually associated with the absorbed OH groups on the surface. Similarly, in NiO_x/FAPbBr₃/TiO₂, we can

find these two peaks which are also ascribed to metal-oxide bonds and OH groups. Additionally, a weak peak around 530.2 eV can be assigned to Ni-O bond.¹⁰

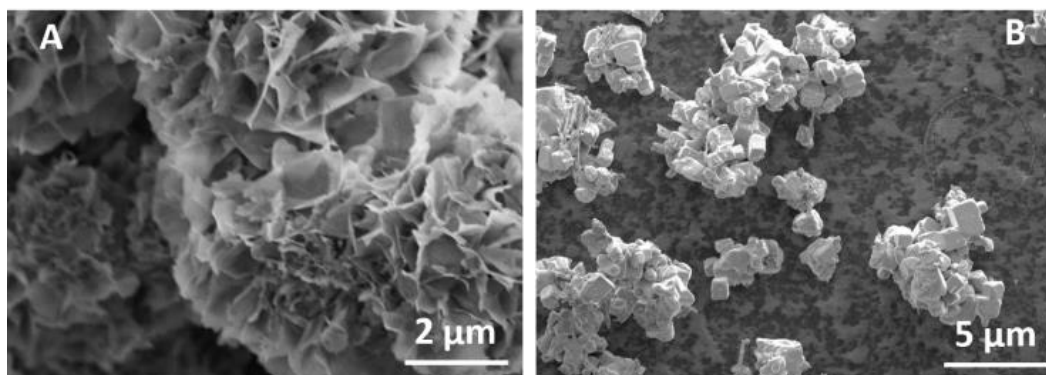


Figure 3-S4. SEM images of (A) NiO_x and (B) FAPbBr₃. From the SEM images, the pure FAPbBr₃ is around 3 μm cubic and NiO_x is composed of uniform 2D nanosheets.

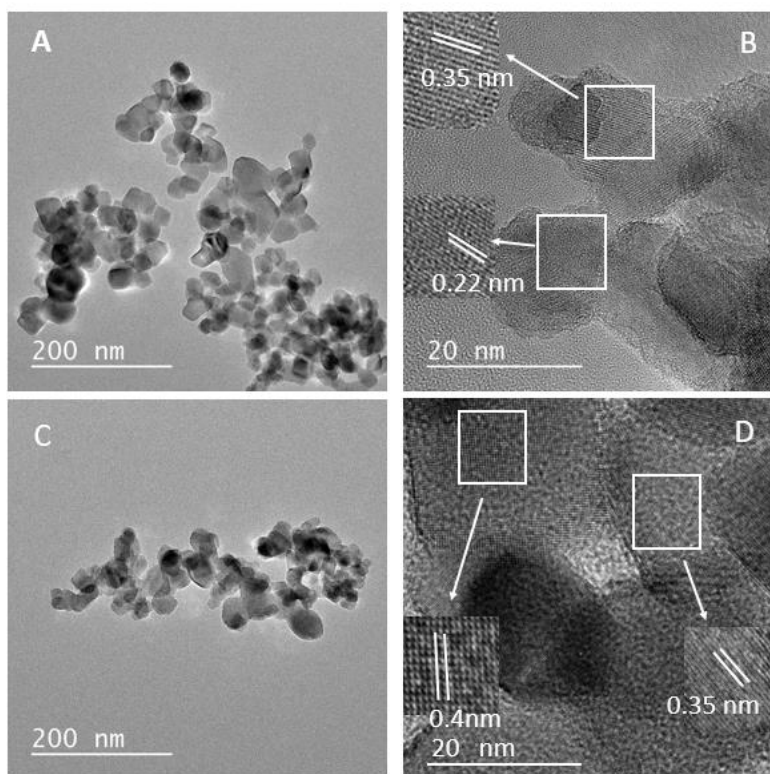


Figure 3-S5. TEM and HRTEM images of (A) and (B)TiO₂, and (C) and (D) FAPbBr₃/TiO₂. The particle shape and size of FAPbBr₃/TiO₂ sample is similar to that of the TiO₂ sample, likely the crystal formation kinetics are influenced by the presence of TiO₂. TiO₂ and FAPbBr₃/TiO₂ represent stacked nanoparticles with an average diameter of 50 nm. HRTEM images of TiO₂ show lattice spacing of 0.35 nm and 0.22 nm, which is indexed as the *d*₁₀₁ and *d*₀₀₁ spacing of anatase TiO₂.¹¹ In FAPbBr₃/TiO₂, a lattice spacing of 0.4 nm can be assigned to the (011) facet of FAPbBr₃.¹²

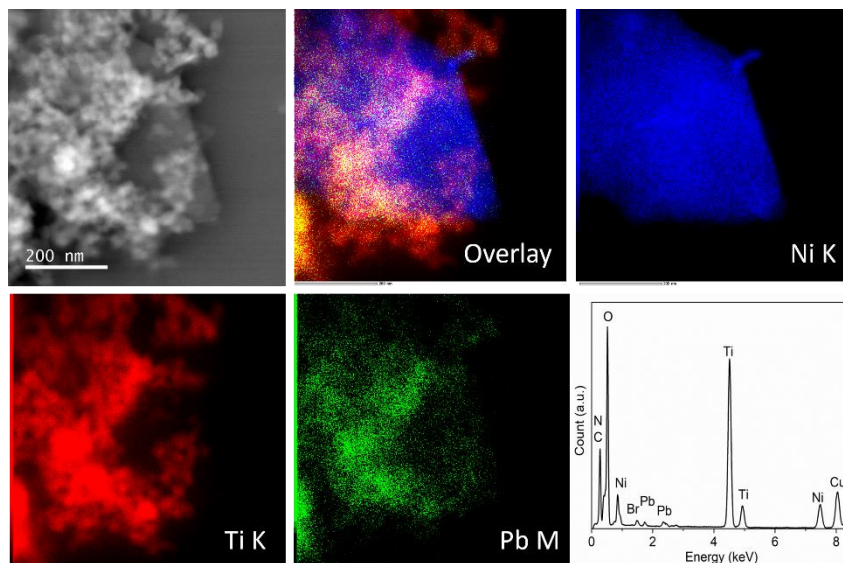


Figure 3-S6. Elemental mapping pattern of the NiO_x/FAPbBr₃/TiO₂ photocatalyst.

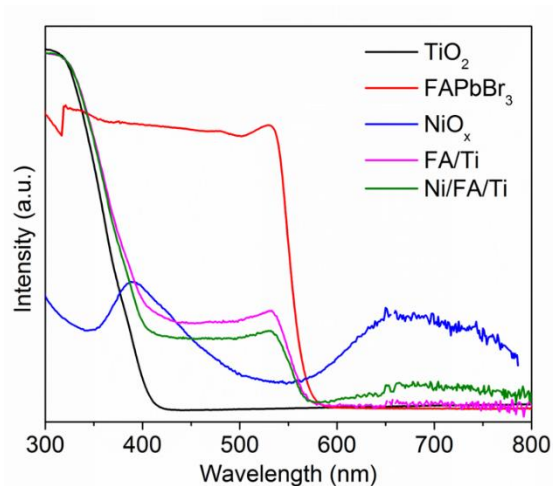


Figure 3-S7. DRS spectra of TiO₂, FAPbBr₃, NiO_x, FAPbBr₃/TiO₂ (FA/Ti) and NiO_x/FAPbBr₃/TiO₂ (Ni/FA/Ti).

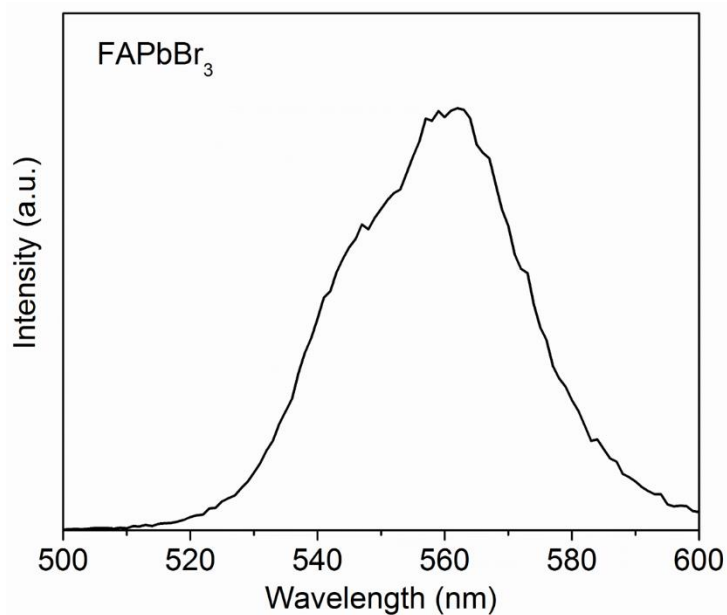


Figure 3-S8. Steady-state PL spectra of FAPbBr₃.

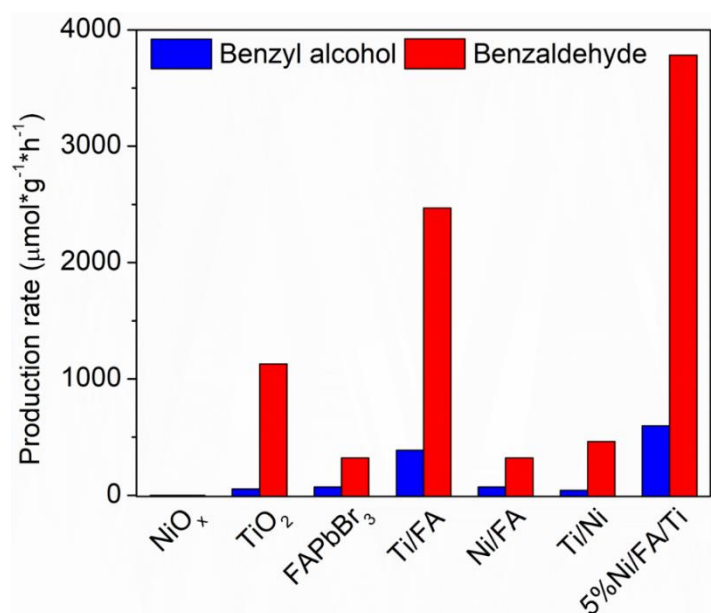


Figure 3-S9. Photocatalytic oxidation of benzyl alcohol over NiO_x, TiO₂, FAPbBr₃, FAPbBr₃/TiO₂ (FA/Ti), NiO_x/FAPbBr₃ (Ni/FA), 5%NiO_x/TiO₂ (Ni/Ti), and 5% NiO_x/FAPbBr₃/TiO₂ (Ni/FA/Ti). . Reaction conditions: photocatalysts (0.01 g), solvent of toluene (2.5 mL) saturated with molecular oxygen, AM1.5G simulated light irradiation, irradiation time (4 h).

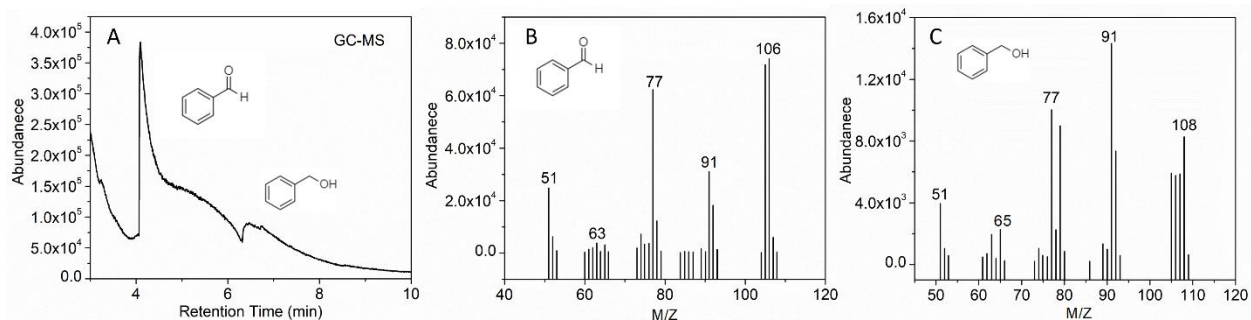


Figure 3-S10. GC-MS spectra of the products obtained after 4h light irradiation.

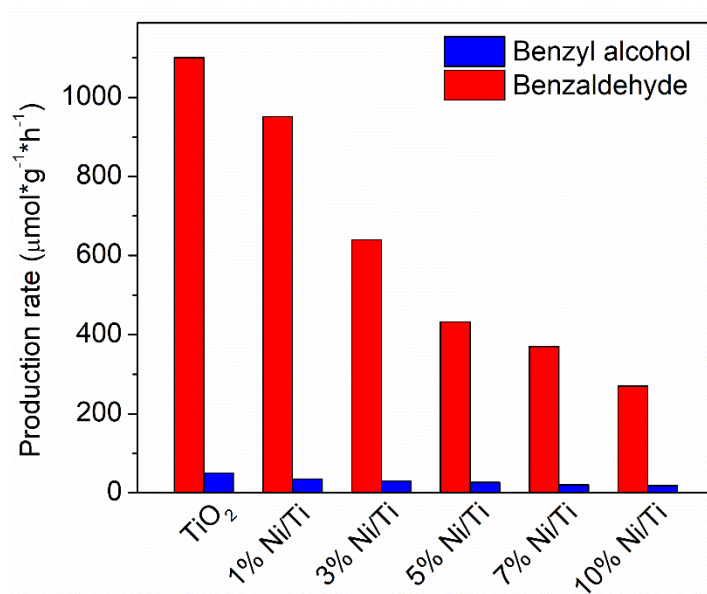


Figure 3-S11. Photocatalytic oxidation of toluene over TiO_2 and a series of $\text{NiO}_x/\text{TiO}_2$ (Ni/Ti) hybrids under solar light irradiation. Reaction conditions: photocatalysts (0.01 g), solvent of toluene (2.5 mL) saturated with molecular oxygen, AM1.5G simulate light irradiation, irradiation time (4 h).

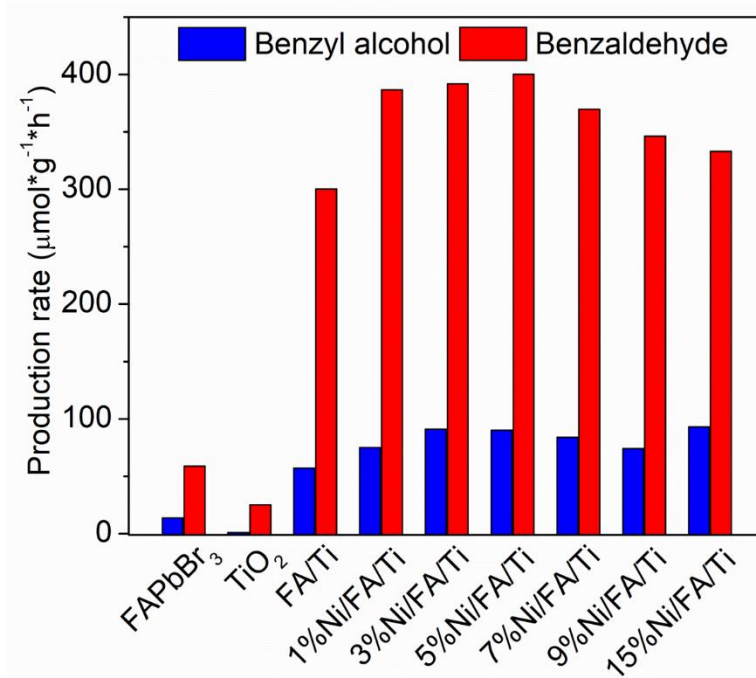


Figure 3-S12. Photocatalytic oxidation of toluene over pure FAPbBr₃, TiO₂, FAPbBr₃/TiO₂ and a series of NiO_x/FAPbBr₃/TiO₂ (Ni/FA/Ti) hybrids under visible light irradiation. Reaction conditions: photocatalysts (0.01 g), solvent of toluene (2.5 mL) saturated with molecular oxygen, visible light irradiation (>420nm), irradiation time (4 h).

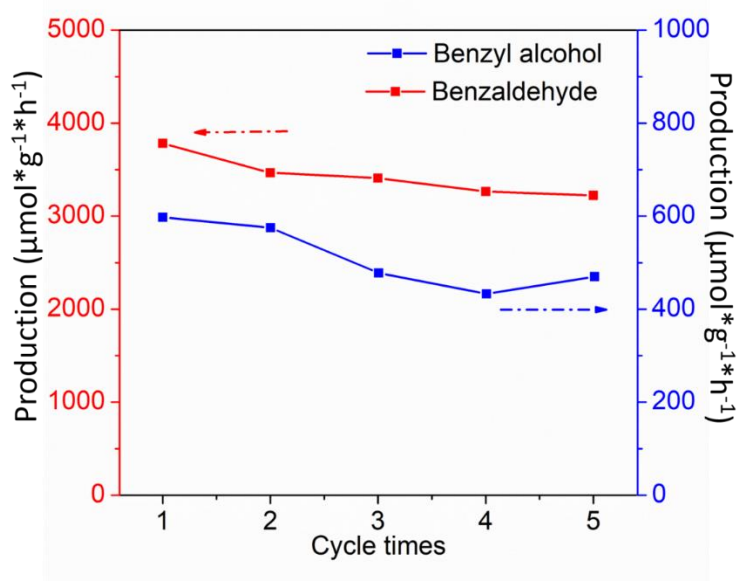


Figure 3-S13. Recycle test for 5% NiO_x/FAPbBr₃/TiO₂ for 5 times. Reaction conditions: photocatalysts (0.01 g), solvent of toluene (2.5 mL) saturated with molecular oxygen, AM1.5G simulated light irradiation, irradiation time (4 h). The material stability during repeated reaction cycles was evaluated. This picture shows the results for 5 wt% NiO_x/FAPbBr₃/TiO₂ following their recycled use during five consecutive 4h reaction cycles. After 5 cycles, the NiO_x/FAPbBr₃/TiO₂ composite remains more than 85 % of its original activity under AM1.5G simulated light irradiation. The slight loss of activity is due to the slow dissolution of FAPbBr₃ in the generated benzaldehyde and the photo-corrosion of TiO₂ under illumination.^{12,13}

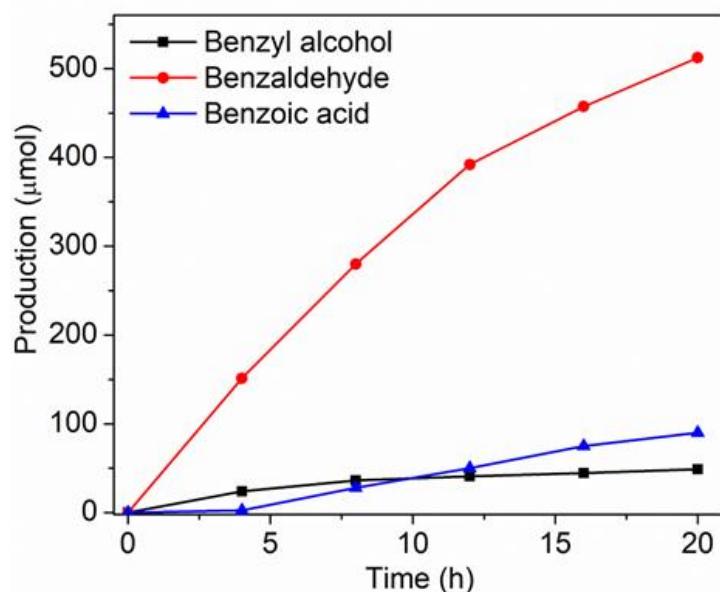


Figure 3-S14. Continuous experiment on toluene oxidation by 5%NiO_x/FAPbBr₃/TiO₂. Reaction conditions: photocatalysts (0.01 g), solvent of toluene (2.5 mL) saturated with molecular oxygen, AM1.5G simulate light irradiation.

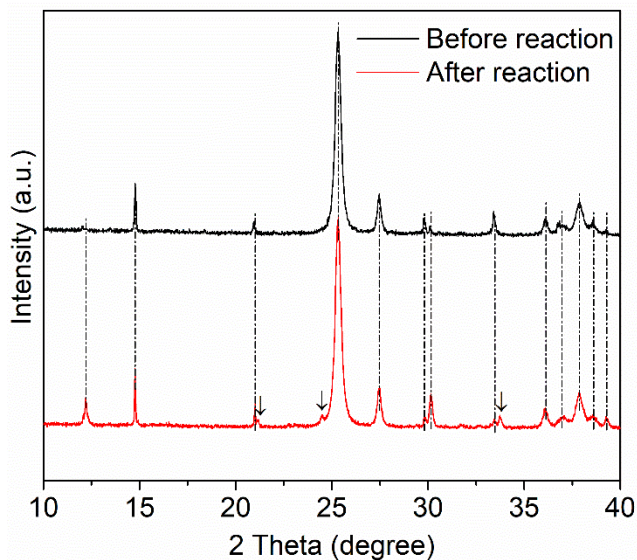


Figure 3-S15. XRD patterns of NiO_x/FAPbBr₃/TiO₂ before and after recycle reaction. After reaction, there are three new peaks appearance which can be attributed to Pb₃O₄.

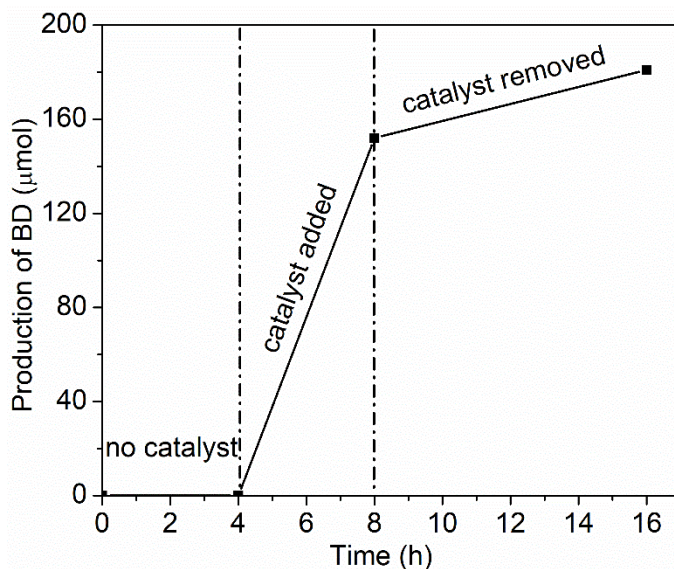


Figure 3-S16. Toluene oxidation over 5%NiO_x/FAPbBr₃/TiO₂. The catalyst was removed via centrifugation and the reaction was continued for 8 h with the liquid phase. Reaction conditions: photocatalysts (0.01 g), solvent of toluene (2.5 mL) saturated with molecular oxygen, AM1.5G simulate light irradiation. A little bit benzaldehyde (BD) generated, after the solid catalyst had been removed, indicating that some catalytically active species were dissolved into the liquid phase.

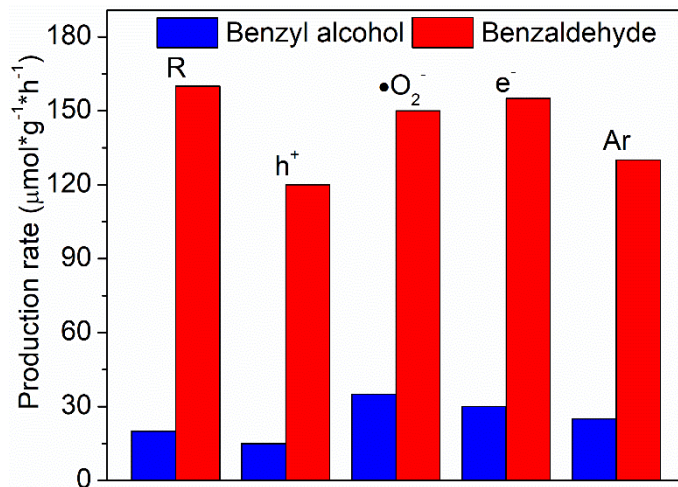


Figure 3-S17. Photocatalytic oxidation of C(sp³)-H in toluene over pure FAPbBr₃ in the absence or presence of various radical scavengers.

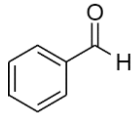
Supporting Table

Table 3-S1. Results of exponential fitting of PL decay traces of FAPbBr₃/TiO₂ and 5%Ni/FAPbBr₃/TiO₂.

Sample	τ_1 (ns)	A ₁ (%)	τ_2 (ns)	A ₂ (%)	τ_3 (ns)	A ₃ (%)
FAPbBr ₃ /TiO ₂	2.2	57	31.2	33	136	10
5%Ni/FAPbBr ₃ /TiO ₂	-	-	-	-	251	100

Here τ indicates the exponential decay time and A represents the amplitude of exponential fitting parameter. These values are including in implemented fit equation: $y = A_1 \cdot \exp(-x/\tau_1) + A_2 \cdot \exp(-x/\tau_2) + A_3 \cdot \exp(-x/\tau_3)$.

Table 3-S2. A summary of the photocatalytic C-H activation performances by photocatalysts.

Catalyst	Solution	Light source	Activity	Reference
			 ($\mu\text{mol g}^{-1} \text{h}^{-1}$)	
FAPbBr ₃	toluene	150 W Xe lamp, visible light ($\lambda >$ 420 nm)	60	This work
FAPbBr ₃	toluene	150 W Xe lamp, AM1.5G	320	This work
NiO _x /FAPbBr ₃ /TiO ₂	toluene	150 W Xe lamp, visible light ($\lambda >$ 420 nm)	400	This work
NiO _x /FAPbBr ₃ /TiO ₂	toluene	150 W Xe lamp, AM 1.5G	3800	This work
P25	9.4 mmol/L toluene in water	Six 6 W UV lamps (310 nm)	47	¹⁴
TiO ₂	9.4 mmol/L toluene in water	Six 6 W UV lamps (310 nm)	94	¹⁴
Flower-like Bi ₂ WO ₆	toluene	300 W Xe lamp, visible-light ($\lambda >$ 400 nm)	464	¹⁵
CdS	0.1 mmol toluene in 1.5 ml BTF	300 W Xe lamp, visible light ($\lambda >$ 420 nm)	201	¹⁶

CdS	toluene	300 W Xe lamp, visible-light ($\lambda >$ 400 nm)	240	15
NbBA	1mmol substrates dissolved in 10 ml BTF	Sunlight	48	17
g-C ₃ N ₄	10 mmol toluene in 20 ml acetonitrile 60 °C	250W w-filament bulb, visible-light ($\lambda >$ 420 nm)	450	18

Table 3-S3. The results of photocatalytic oxidation of C(sp³)-H on toluene and substituted toluene over pure FAPbBr₃, TiO₂, FAPbBr₃/TiO₂ and 5%NiO_x/FAPbBr₃/TiO₂ hybrid. Reaction conditions: photocatalysts (0.01 g), substrate(2.5 mL) saturated with molecular oxygen, AM1.5G simulated light irradiation, irradiation time (4 h).

Substrate	Sample	Conversion(%)	Selective(%)	Yield(%)
Toluene	FAPbBr ₃	0.075	81	0.06
Toluene	TiO ₂	0.23	95	0.22
Toluene	NiO _x	0	0	0
Toluene	TiO ₂ /NiO _x	0.10	91	0.09
Toluene	FAPbBr ₃ /NiO _x	0.075	82	0.06
Toluene	FAPbBr ₃ /TiO ₂	0.55	86	0.47

Toluene	5% NiO _x / FAPbBr ₃ /TiO ₂	0.85	86	0.73
p-Fluorotoluene	5% NiO _x / FAPbBr ₃ /TiO ₂	0.70	81	0.56
p-Xylene	5% NiO _x / FAPbBr ₃ /TiO ₂	0.82	77	0.63
p-Cresol	5% NiO _x / FAPbBr ₃ /TiO ₂	1.02	99	1.02

Table 3-S4. The results of the oxidation of cycloalkanes with 5%NiO_x/FAPbBr₃/TiO₂. Reaction conditions: photocatalysts (0.01 g), cycloalkanes (2.5 mL) saturated with molecular oxygen, AM1.5G simulated light irradiation, irradiation time (4 h).

substrate	Main product	Production rate ($\mu\text{mol g}^{-1} \text{h}^{-1}$)	Conversion(%)	Selectivity(%)	Yield(%)
		89	0.016	>99	0.016
		138	0.032	>99	0.032

References

- (1) Wang, C. C.; Ying, J. Y. Sol–Gel Synthesis and Hydrothermal Processing of Anatase and Rutile Titania Nanocrystals *Chem. Mat.* **1999**, *11*, 3113-3120.
- (2) Hall, D. S.; Lockwood, D. J.; Bock, C.; MacDougall, B. R. Nickel hydroxides and related materials: a review of their structures, synthesis and properties. *Proc. R. Soc. A* **2015**, 471.
- (3) Xia, Y.; Zhang, W. K.; Xiao, Z.; Huang, H.; Zeng, H. J.; Chen, X. R.; Chen, F.; Gan, Y. P.; Tao, X. Y. Biotemplated fabrication of hierarchically porous NiO/C composite from lotus pollen grains for lithium-ion batteries. *J. Mater. Chem.* **2012**, *22*, 9209-9215.
- (4) Zhao, Y. D.; Gu, G. C.; You, S. Q.; Ji, R. H.; Suo, H.; Zhao, C.; Liu, F. M. Preparation of Ni(OH)₂ nanosheets on Ni foam via a direct precipitation method for a highly sensitive non-enzymatic glucose sensor. *Rsc Adv.* **2015**, *5*, 53665- 53670.
- (5) You, J.; Meng, L.; Song, T.-B.; Guo, T.-F.; Yang, Y.; Chang, W.-H.; Hong, Z.; Chen, H.; Zhou, H.; Chen, Q.; et al. Improved Air Stability of Perovskite Solar Cells via Solution-Processed Metal Oxide Transport Layers. *Nat. Nanotech.* **2015**, *11*, 75.
- (6) Zhu, Z. L.; Bai, Y.; Zhang, T.; Liu, Z. K.; Long, X.; Wei, Z. H.; Wang, Z. L.; Zhang, L. X.; Wang, J. N.; Yan, F.; Et Al. High-performance Hole-Extraction Layer of Sol-gel-processed NiO Nanocrystals for Inverted Planar Perovskite Solar Cells. *Angew. Chem. Int. Ed.* **2014**, *53*, 12779-12783.
- (7) Manders, J. R.; Tsang, S. W.; Hartel, M. J.; Lai, T. H.; Chen, S.; Amb, C. M.; Reynolds, J. R.; So, F. Solution-Processed Nickel Oxide Hole Transport Layers in High Efficiency Polymer Photovoltaic Cells. *Adv. Funct. Mater.* **2013**, *23*, 2993-3001.
- (8) Zhou, T. T.; Cao, Z.; Zhang, P.; Ma, H. Y.; Gao, Z.; Wang, H.; Lu, Y.; He, J.; Zhao, Y. F. Transition metal ions regulated oxygen evolution reaction performance of Ni-based hydroxides hierarchical nanoarrays. *Sci. Rep.* **2017**, *7*.
- (9) Su, Y. Z.; Xiao, K.; Li, N.; Liu, Z. Q.; Qiao, S. Z. Amorphous Ni(OH)₂@three-dimensional Ni core–shell nanostructures for high capacitance pseudocapacitors and asymmetric supercapacitors. *J. Mater. Chem. A* **2014**, *2*, 13845-13853.
- (10) Huang, H.; Yuan, H.; Janssen, K. P. F.; Solís-Fernández, G.; Wang, Y.; Tan, C. Y. X.; Jonckheere, D.; Debroye, E.; Long, J.; Hendrix, J.; et al Efficient and Selective Photocatalytic Oxidation of Benzylic Alcohols with Hybrid Organic–Inorganic Perovskite Materials. *ACS Energy Lett.* **2018**, *3*, 755-759.

- (11) Huang, H. W.; Lin, J. J.; Fan, L. Z.; Wang, X. X.; Fu, X. Z.; Long, J. L. Heteroatomic Ni, Sn Clusters-grafted Anatase TiO₂ Photocatalysts: Structure, Electron Delocalization, and Synergy for Solar Hydrogen Production. *J. Phys. Chem. C* **2015**, 119, 10478-10492.
- (12) Perumal, A.; Shendre, S.; Li, M. J.; Tay, Y. K. E.; Sharma, V. K.; Chen, S.; Wei, Z. H.; Liu, Q.; Gao, Y.; Buenconsejo, P. J. S.; et al. High Brightness Formamidinium Lead Bromide Perovskite Nanocrystal Light Emitting Devices. *Sci. Rep.* **2016**, 6, 36733.
- (13) Schünemann, S.; Van Gastel, M.; Tüysüz, H. A Cspbb3/TiO₂ Composite for Visible-Light Driven Photocatalytic Benzyl Alcohol Oxidation. *Chemsuschem* **2018**, 11, 2057.
- (14) Cao, F.-L.; Wang, J.-G.; Lv, F.-J.; Zhang, D.-Q.; Huo, Y.-N.; Li, G.-S.; Li, H.-X.; Zhu, J. Photocatalytic oxidation of toluene to benzaldehyde over anatase TiO₂ hollow spheres with exposed {001} facets. *Catal. Commun.* **2011**, 12, 946-950.
- (15) Liu, Y.; Chen, L.; Yuan, Q.; He, J.; Au, C.-T.; Yin, S.-F. A Green and Efficient Photocatalytic Route for the Highly-Selective Oxidation of Saturated Alpha-Carbon C–H Bonds in Aromatic Alkanes Over Flower-Like Bi₂WO₆. *Chem. Commun.* **2016**, 52, 1274-1277.
- (16) Zhang, Y. H.; Zhang, N.; Tang, Z. R.; Xu, Y. J. Transforming Cds into an Efficient Visible Light Photocatalyst for Selective Oxidation of Saturated Primary C–H Bonds Under Ambient Conditions. *Chem. Sci.* **2012**, 3, 2812-2822.
- (17) Sarina, S.; Zhu, H.; Zheng, Z.; Bottle, S.; Chang, J.; Ke, X.; Zhao, J.-C.; Huang, Y.; Sutrisno, A.; Willans, M.; Li, G. Driving selective aerobic oxidation of alkyl aromatics by sunlight on alcohol grafted metal hydroxides. *Chem. Sci.* **2012**, 3, 2138-2146.
- (18) Zhang, P. F.; Wang, Y.; Yao, J.; Wang, C. M.; Yan, C.; Antonietti, M.; Li, H. R. Visible-Light-Induced Metal-Free Allylic Oxidation Utilizing a Coupled Photocatalytic System of G-C₃N₄ and N-Hydroxy Compounds. *Adv. Synth. Catal.* **2011**, 353, 1447-1451.

Chapter 4

Direct Z-Scheme FAPbBr₃/Bi₂WO₆ Heterojunction for Photoredox Reaction with Large Driving Force

Haowei Huang, Jiwu Zhao, Chen Zhou, Yijie Du, Menglong Zhang, Zhuan Wang, Yuxiang Weng, Yongfu Sun, Jinlin Long, Johan Hofkens, Julian A. Steele, and Maarten Roeffaers*

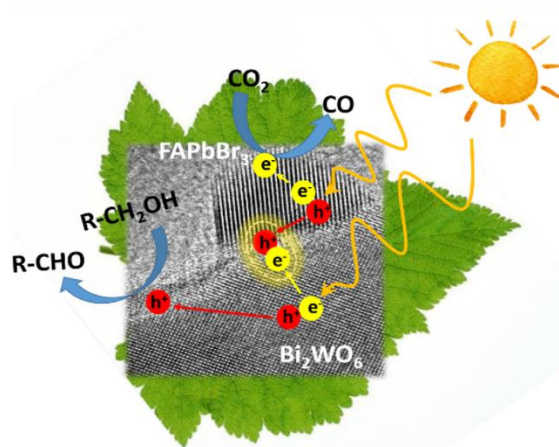
Submitted for publication.

Contributions

H.H. and M.B.J.R. designed the project; H.H. conducted the most experiments, including samples preparation, TEM, DRS, XRD, AFM, GC-MS and activity tests. Most of this work has been realized during a research stay at Fuzhou University, China, from July 2019 to September 2019. J.Z. carried out the theoretical calculations; C.Z., Y.D. and M.Z. performed part of experiments; Z. W., Y.W., Y.S., J.L., J.H. supported the experiments and helped to analyse the results; H.H. analyzed all results and wrote the draft; H.H., J.A.S. and M.B.J.R. together revised the manuscript with input from all the authors.

Abstract : Metal halide perovskites with direct bandgap and strong light absorption are promising materials for harvesting solar energy, however, their relatively narrow bandgap limits their redox ability when used as a photocatalyst. Adding a second semiconductor component with the appropriate band structure offsets can generate a Z-scheme photocatalytic system, taking full advantage of the perovskite's intrinsic properties. In this work, we develop a direct Z-scheme photocatalyst based on formamidinium lead bromide and bismuth tungstate (FAPbBr₃/Bi₂WO₆) with strong redox ability, for artificial photosynthesis. With desirable band offsets and strong joint redox potential, the dual photocatalyst is shown to form a semi-coherent hetero-interface. Ultrafast transient infrared absorption studies employing selective excitation reveal synergetic photocarrier dynamics and demonstrate Z-scheme charge transfer mechanisms. Under simulated solar irradiation, a large driving force photoredox reaction (ca. 2.57 eV) of CO₂ reduction coupled with benzyl alcohol oxidation to benzaldehyde is achieved on the Z-scheme FAPbBr₃/Bi₂WO₆ photocatalyst, harnessing the full synergetic potential of the combined system.

Table of Contents



4.1 Introduction

Like the naturally occurring photosynthetic conversion of solar light within green plants, photocatalysis presents an effective way for artificial solar-to-chemical energy conversion. For this, it is optimal to implement photocatalysts with strong and broadband light absorption, efficient photo-carrier separation and strong redox abilities. In single-component photocatalysts, the charge separation is typically limited and a strong redox ability is compromised when harvesting low-energy photons. Metal halide perovskites (MHPs) have emerged as interesting materials for solar energy conversion because of their tunable bandgap (E_g), excellent charge transport properties and their low-cost, facile processing.^{1,2} As photocatalysts, however, they have a limited redox ability for oxidation reactions. The development of MHPs-based heterojunction photocatalysts (e.g. MAPbI₃/TiO₂ and CsPbBr₃/C₃N₄) have improved their ability for photocatalytic H₂O splitting, CO₂ reduction, and organic synthesis.³⁻⁵ However, in these reported type-II heterostructures the redox ability of the MHPs is further compromised (Figure 4-1A). With the addition of a second photosystem possessing strong oxidation ability and suitable band offsets, a MHP-based direct Z-scheme hetero-junction can be engineered (Figure 4-1B) to fully harness the best of both worlds; exploit the desirable optoelectronic properties of narrow bandgap MHPs and enable photo-generated electrons/holes with stronger redox abilities.^{6,7} However, the disadvantage of this system is that it needs 2 photons to generate a redox equivalent.

Within this context, a suitable second photocatalyst is bismuth tungstate (Bi₂WO₆; bandgap of 2.9 eV) which has a relatively positive valence band (VB; ca. 3.0 eV vs RHE) and exhibits excellent photocatalytic performance in organic and water oxidation reactions under visible light irradiation.⁸⁻¹¹ Bi₂WO₆ is also n-type, with a Fermi energy near to its conduction band (CB; ca. 0.1 eV vs RHE).¹² The relative CB/VB energies of perovskites FAPbBr₃ (-1.0 eV/1.2 eV) and CsPbBr₃ (-0.8 eV/1.4 eV) are more negative than those found in Bi₂WO₆ and the Fermi energy in these two MHPs is reported to be ca. -0.8 and -0.5 eV vs RHE, respectively.^{13,14} The energetics of Bi₂WO₆ relative to these Br-based halide perovskites indicates the two systems can combine suitably to form a direct Z-scheme photocatalyst, with improved overall oxidation ability.⁶

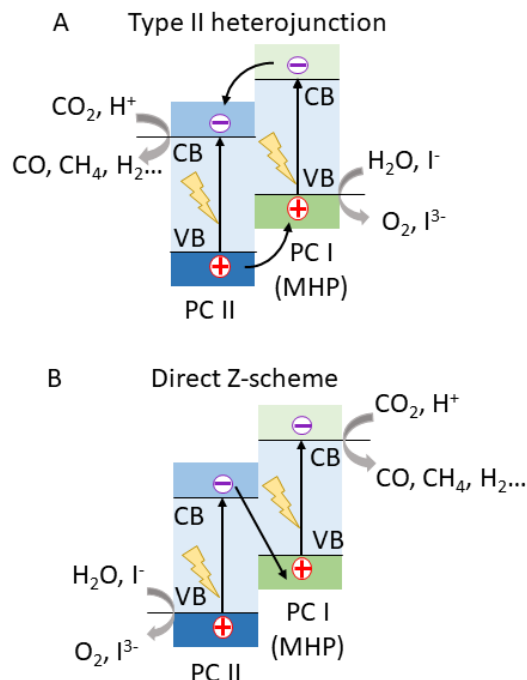


Figure 4-1. Scheme of photocatalytic H_2 evolution or CO_2 reduction on dual semiconducting photocatalysts (PCs I and II). (A) Type-II heterojunction. (B) Direct Z-scheme photocatalyst.

The solar-driven water splitting and CO_2 reduction depicted in Figure 4-1B are not optimal for fully exploiting the superior redox ability of the MHP-based direct Z-scheme; the low driving force of this reaction (< 1.5 eV) can be driven purely by a pristine MHP or a MHP-based type-II heterojunction. Further, the generated chemical fuels here are of low commercial value.¹⁵ We suggest that the generation of solar fuels can be coupled here to the synthesis of value-added organic materials requiring a large drive force, to both improve economic performance and industrialization potential of the artificial photosynthetic reaction.^{15,16} Benzaldehyde (BD) is an important industrial organic product (predicted annual sales is 301m USD by 2022¹⁷), with current production approaches employing the hydrolysis of benzal chloride, involving the stoichiometric production of HCl.¹⁸ The selective photocatalytic conversion of benzyl alcohol (BA) to BD is a highly desirable alternative route,^{19,20} though is limited by its relatively large required oxidation potential (2.45 eV vs RHE).

Here we report the development and application of the solar-driven photocatalyst $\text{FAPbBr}_3/\text{Bi}_2\text{WO}_6$, for the large driving force photoredox reaction (ca. 2.57 eV) of CO_2 reduction coupled with benzyl alcohol oxidation to benzaldehyde. Detailed physico-chemical characterization shows this hybrid system to

benefit from a semi-coherent hetero-interface as a result of only minor lattice mismatch. The photophysics of FAPbBr₃/Bi₂WO₆ were studied via ultrafast transient IR absorption, revealing a direct Z-scheme pathway for photo-generated carriers. Exploiting the full photo-oxidation strength of the hybrid system, we demonstrate effective BA-to-BD oxidation coupled to CO₂-to-CO photoreduction under simulated solar illumination (AM1.5G filter, 100 mW/cm²), with near 100% selectivity (CO and BD as main products). An experimentally and theoretically (ab initio calculations using density functional theory; DFT) supported model is proposed to rationalize the photo-reaction pathway, which constitutes the largest driving force (2.57 eV) ever reported for an artificial photosynthetic reaction^{6,16,21,22}.

4.2 Results

To generate the FAPbBr₃/Bi₂WO₆ composite photocatalysts, we first hydrothermally prepared the Bi₂WO₆ using Bi(NO₃)₃·5H₂O and Na₂WO₄·2H₂O as precursors (details are provided in the Supporting Information).⁸ The FAPbBr₃/Bi₂WO₆ (FA/Bi) composite was synthesized by a room-temperature anti-solvent precipitation method where FAPbBr₃ and PbBr₂ dissolved in N,N-dimethylformamide (DMF) was added dropwise to a suspension of Bi₂WO₆ in toluene (see SI).^{19,23} For reference, pure FAPbBr₃ was prepared by the same method using pure toluene. Powder X-ray diffraction (PXRD) was used to validate the crystallinity and phase of the obtained materials. (Figure 4-S1) Where pure FAPbBr₃ and Bi₂WO₆ are indexed to the cubic and orthorhombic phases, respectively,^{8,19} the FAPbBr₃/Bi₂WO₆ composite consists of diffraction peaks arising from both. The formation of a FAPbBr₃/Bi₂WO₆ composite, rather than two separated phases, is confirmed by scanning electron microscopy (SEM: Figure 4-S2); the morphology and surface area (Figure 4-S3 and Table 4-S1) of the dual FAPbBr₃/Bi₂WO₆ system is mainly dictated by the flower-like structure of the Bi₂WO₆ (made of ~5-nm-thick flakes; Figure 4-S4). The anti-solvent procedure yielded microcrystals of pure FAPbBr₃ in the hybrid sample which are not well-resolved using SEM.^{19,24} Figures 4-2A and 4-2B examines the FAPbBr₃/Bi₂WO₆ composite via transmission electron microscopy (TEM), revealing the Bi₂WO₆ sheets to be decorated with highly dispersed small FAPbBr₃ dots which can be confirmed by energy-dispersive X-ray spectroscopic elemental mapping (Figure 4-S5). From high-resolution transmission electron microscopy (HRTEM: Figure 4-S6 and 4-S7) the lattice spacings of FAPbBr₃ ([011] = 0.4 nm and [002] = 0.3 nm) and Bi₂WO₆ ([200] = [002] = 0.27 nm) are well-resolved.^{8,23} The boundary adjoining the two crystal structures is observed to form a semi-coherent interface spanning several unit cells, as depicted in Figure 4-2C and 4-2D. A comparison of their relative lattice parameters

indicates a low mismatch factor (f) of 10% [$f = (1 - d(\text{Bi}_2\text{WO}_6)/d(\text{FAPbBr}_3))$] arises between the FAPbBr_3 (002) and Bi_2WO_6 (002) crystal planes.²⁴ Here the structure FAPbBr_3 and Bi_2WO_6 coincide every few lattice spacing, i.e. $10d(\text{Bi}_2\text{WO}_6) = 9d(\text{FAPbBr}_3)$. The formation of this semi-coherent interface will introduce an intimate chemical and energetic interaction between the two components. The altered chemical state of the connected material was confirmed by X-ray photoelectron spectroscopy (XPS: Figure 4-S8). The binding energy of the N 1s, Pb 4f, and Br 3d (arising from FAPbBr_3) XPS peaks in the hybrid system all shift to higher energy, compared to the pristine FAPbBr_3 . This is contrasted by the XPS emerging from the Bi_2WO_6 side, namely Bi 4f, W 4f, and O 1s peaks which all display a lower binding energy, compared to pure a Bi_2WO_6 .²⁵ These complimentary features are a signature of strong heterojunction formation in the composite, with a respective decrease and increase in the electron density and electron-accepting ability of the FAPbBr_3 moiety. This is accompanied by an increased electron density and enhanced electron-donating ability for the Bi_2WO_6 side. As a result, there is an internal electric field and the tendency for the system to undergo electron transfer from Bi_2WO_6 to FAPbBr_3 is significantly strengthened.²⁴

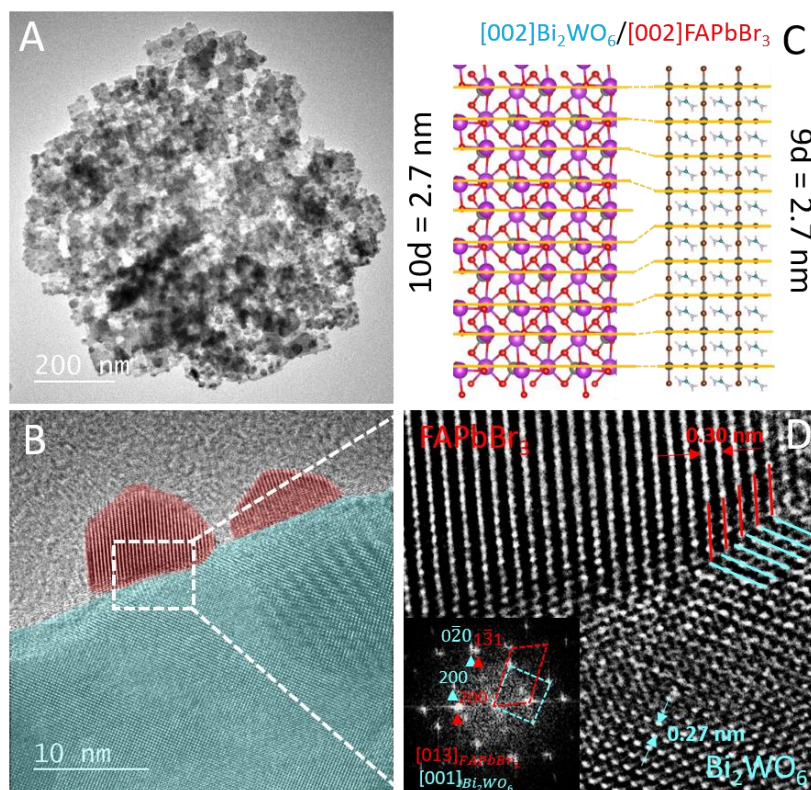


Figure 4-2. (A)TEM and (B) HRTEM of 12.5% FA/Bi; (C) scheme of the semi-coherent interface formed between FAPbBr₃ (red) and Bi₂WO₆ (blue), which is directly resolved in (D) for 12.5% FA/Bi with the corresponding FFT pattern shown in the inset.

The relative band energies of these materials are experimentally resolved using a combination of UV-visible diffuse reflectance spectroscopy (DRS) and ultraviolet photoelectron spectroscopy (UPS). Figure 4-3A shows the DRS of the FAPbBr₃/Bi₂WO₆ composite and the pure Bi₂WO₆ and FAPbBr₃ materials, along with their corresponding transformed Kubelka-Munk spectrum in Figure 4-3B. Here the band-edge absorption of Bi₂WO₆ and FAPbBr₃ is determined to be 2.9 eV and 2.2 eV, respectively (Figure 4-3C). The location of the VB edge in Bi₂WO₆ and FAPbBr₃ is determined via UPS studies (Figure 4-3D and 4-3E), with a calibration made with respect to the He I photon energy (21.2 eV). A sample bias of 5 eV was applied to observe the secondary electron cutoff (Figure 4-3F). The work function (Fermi level) can be calculated by the photon energy and secondary electron cutoff energy. For pure FAPbBr₃ and Bi₂WO₆, the work function is determined to be -0.9 and 0 eV vs RHE, respectively. Importantly, based on the VB edges (E_{VB}) (vs Fermi level) shown in Figure 4-3E, the E_{VB} of FAPbBr₃ is resolved to be 0.9 eV vs RHE,²⁶ while the value of E_{VB} in Bi₂WO₆ is 2.8 eV vs RHE.²⁷ Combined with the aforementioned optical bandgap, the relative CB edges of Bi₂WO₆ and FAPbBr₃ are positioned respectively at -0.1 and -1.3 eV vs RHE. These data directly inform the band structures depicted in Figure 4-3G, highlighting the formation of a direct Z-scheme with an internal electrostatic field when interfaced, which drives photogenerated electrons from Bi₂WO₆ to FAPbBr₃ (Figure 4-3G).⁶

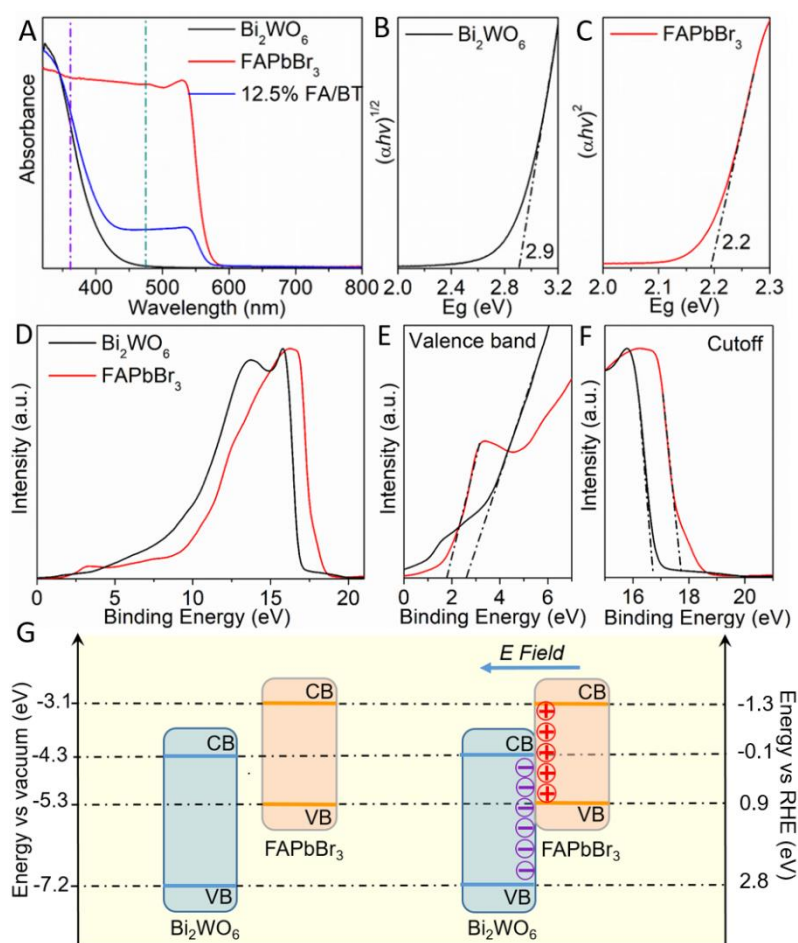


Figure 4-3. (A) UV-Vis DRS spectrum of Bi_2WO_6 , FAPbBr_3 and 12.5% $\text{FAPbBr}_3/\text{Bi}_2\text{WO}_6$, and (B, C) the corresponding bandgap; (D) UPS spectrum, (E) Valence band edge and (F) secondary electron cutoff of Bi_2WO_6 and FAPbBr_3 ; (G) Schematic diagram of the band position of Bi_2WO_6 and FAPbBr_3 determined by DRS and UPS. The vertical lines in (A) indicate the selective photo-excitation implemented in the transient pump-probe IR data shown in Figure 4-4.

Ultrafast time-resolved IR transient absorption spectroscopy is utilized to directly track the modified photogenerated charge transfer pathways in the hybrid $\text{FAPbBr}_3/\text{Bi}_2\text{WO}_6$ hetero-structure. The transient IR was probed at 2090 cm^{-1} which is free from the spectral interference caused by the vibrational absorption peaks, based on the Fourier transform infrared (FTIR) spectroscopy (Figure 4-S9). Thus, the detected changes in IR absorbance after the initial photo-carrier injection can be assigned to the intra-band transition of the electrons in the CBs.²⁸⁻³⁰ Two different pump wavelengths are implemented, at 360 nm and 470 nm, to selectively excite both materials and solely the FAPbBr_3 component, respectively (see Figure 4-3A). The IR decay curve after 470 nm excitation (Figure 4-4A and Table 4-S2) reveals that the

photoexcited electrons have a longer lifetime in the composite material compared to the pure FAPbBr₃. This is paralleled by a marked difference in the rising phase (sub-ps regime) between FAPbBr₃ and FAPbBr₃/Bi₂WO₆, corresponding to the electron injection (Figure 4-4B and Table 4-S3). Notably, the injection in FAPbBr₃/Bi₂WO₆ is much slower than the pure FAPbBr₃ perovskite that electrons were excited from VB to CB, due to the fact that electrons generated on the FAPbBr₃ side are delayed by their injection into Bi₂WO₆ (inset of Figure 4-4A). Simultaneously pumping both components with 360 nm irradiation, the lifetime of electrons in FAPbBr₃/Bi₂WO₆ is shorter than that in pure Bi₂WO₆ (Figure 4-4C and Table 4-S4). Furthermore, in the rising phase implementing 360 nm excitation (Figure 4-4D and Table 4-S3), the injection time in FAPbBr₃/Bi₂WO₆ is close to both pure FAPbBr₃ and Bi₂WO₆. These results indicate that electrons do not transfer from the FAPbBr₃ CB to the Bi₂WO₆ CB in the composite system, in the fs-ps time scale. This is in contrast to the electron transfer observed when FAPbBr₃ is selectively excited by 470 nm light (Figure 4-4A), resembling a type-II heterojunction. This can be understood considering that the Bi₂WO₆ CB gets partially filled under 360 nm excitation, which causes Coulombic repulsion between the electrons in the Bi₂WO₆ CB and FAPbBr₃ CB (inset of Figure 4-4C). Thus, electron injection into the Bi₂WO₆ CB from excited states in the FAPbBr₃ CB will be partly hindered and cannot be observed in fs-ps time scale (Figure 4-4D).

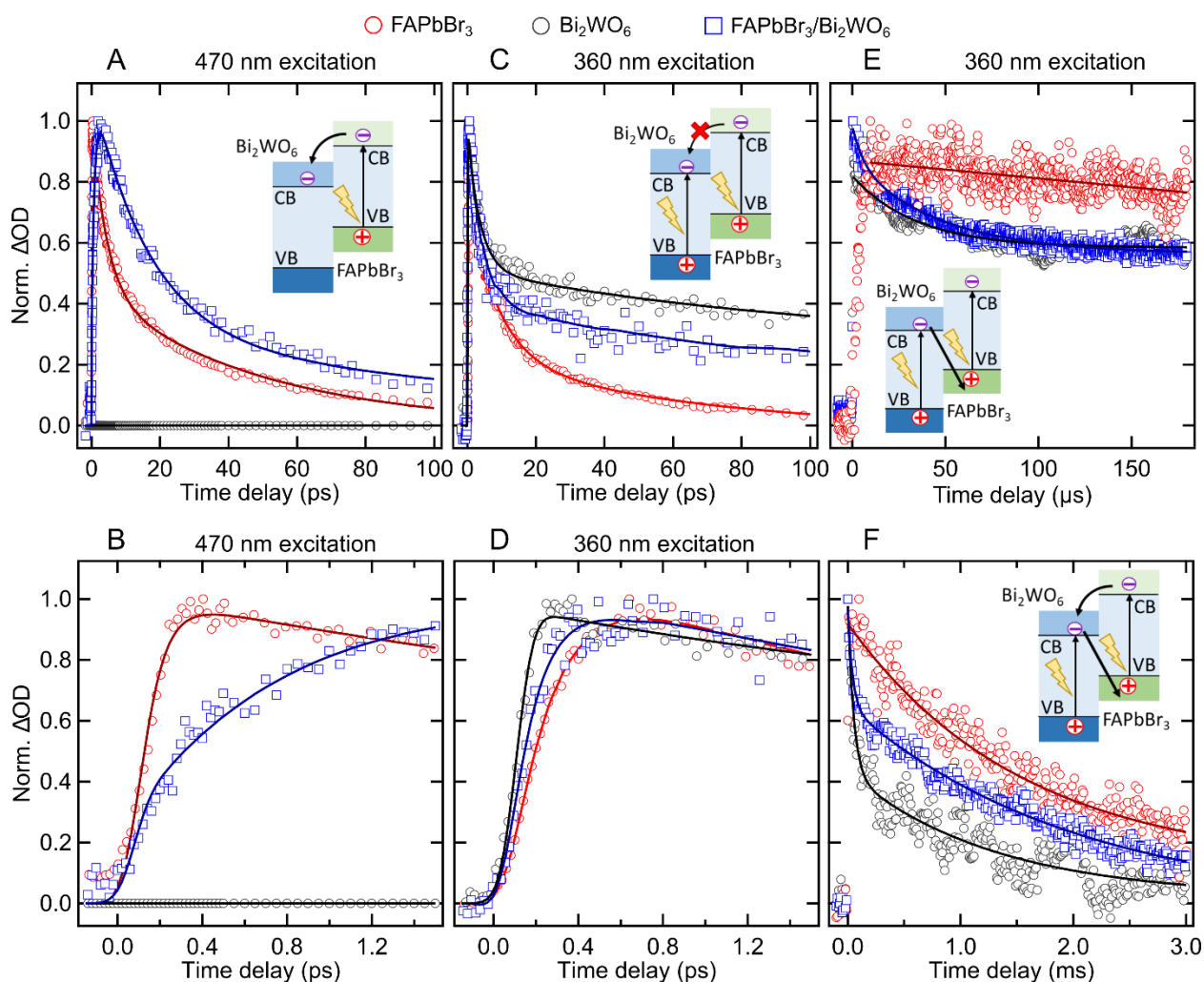


Figure 4-4. Femtosecond and nanosecond time-resolved IR transient absorption traces (normalized optical density; OD) recorded at 2090 cm^{-1} from the Bi₂WO₆, FAPbBr₃, and 12.5% FA/Bi. (A) Decay and (B) rising phase signals upon 470 nm excitation. (C) Decay and (D) rising phase signals upon 360 nm excitation. Transient changes in OD using 360 nm excitation over (E) microseconds and (F) milliseconds. The insets in A, C, E and F depict electronic interactions derived from their respective transients.

Further details of the Z-scheme structure are resolved on the ns- μ s time-scale of the IR transient absorption (Figure 4-4E and 4-4F; 360 nm excitation), which tracks the carrier recombination parameters (Table S5). Compared to the isolated Bi₂WO₆ and FAPbBr₃ systems, an additional relatively fast decaying species ($\tau_1 = 5.9 \mu\text{s}$) is introduced into the excited composite system (Figure 4-4E). This new fast component is ascribed to the recombination of electrons in the CB of Bi₂WO₆ with the VB holes in FAPbBr₃, corresponding to the Z scheme recombination process (inset of Figure 4E). This is in line with the

recombination mechanism proposed in similar studies³⁰⁻³², which emphasize a relatively fast depopulation via the Z-scheme band diagram. On a longer time scale of several milliseconds (Figure 4-4F and Table 4-S5), the slow species ($\tau_2= 47 \mu\text{s}$ and $\tau_3= 1.99 \text{ ms}$) in the composite system is much longer than that in Bi_2WO_6 ($\tau_2= 34 \mu\text{s}$ and $\tau_3= 1.07 \text{ ms}$) and FAPbBr_3 ($\tau_3= 1.53 \text{ ms}$), which can be attributed to a shift in the balance between band alignment and Coulomb repulsion at the interface, leading the system to transform back to a type-II heterojunction from the Z-scheme, as electrons in the CB of Bi_2WO_6 are consumed by holes in the FAPbBr_3 VB (inset of Figure 4-4F).

In Figure 4-5A and 4-5B photocatalytic CO_2 reduction coupled with BA oxidation in trifluorotoluene on the pure single FAPbBr_3 and Bi_2WO_6 photocatalysts, and the Z-scheme $\text{FAPbBr}_3/\text{Bi}_2\text{WO}_6$ system, is evaluated under AM 1.5G simulate solar light irradiation (100 mW/cm^2). After reaction, gas and liquids are collected and detected by gas chromatography separately to identify the products. For Pristine FAPbBr_3 , small amounts of CO can be detected. Additional experiments replacing CO_2 with Ar show this minor CO production is not related to CO_2 reduction, but rather the self-decomposition of FAPbBr_3 (Table 4-S6). For pure Bi_2WO_6 , no reduction product is detected. This is in contrast to the Z-scheme $\text{FAPbBr}_3/\text{Bi}_2\text{WO}_6$ photocatalyst, which produces significant amounts of CO. The CO evolution rate systematically increases with rising amounts of FAPbBr_3 and reaches its maximum performance at $170 \mu\text{mol g}^{-1} \text{ h}^{-1}$ (~100% selectively) with 12.5 wt% FAPbBr_3 content. This value is by far the highest among all reported perovskite-based photocatalysts (Table 4-S7). The apparent quantum yield (AQY) of CO production is 1.2% at 400 nm. At higher loadings of perovskite (i.e. over 12.5 wt%), the lower CO evolution rate can be ascribed to an over injection of charge in the FAPbBr_3 perovskite, which disrupts the balance between band alignment and Coulomb repulsion at the interface, leading more to a type-II heterojunction with diminished drive force. Additional control experiments (saturated with Ar rather than CO_2) in Table 4-S6 verify that the CO is mainly (92%) produced via the photo-reduction of CO_2 . This is further supported by isotope-labeling experiments, using $^{13}\text{CO}_2$ (Figure 4-S10). At the same time, BD is synthesized via the photo-oxidation of BA, with near 100% selectively (Figure 4-5B). While CO_2 is reduced effectively to CO, BA is oxidized to BD with a generation rate which follows the same trend as CO formation, as CO and BD generation is a two electrons/holes reaction. Here the BD production also reaches its maximum at 12.5 wt% $\text{FAPbBr}_3/\text{Bi}_2\text{WO}_6$, with $250 \mu\text{mol g}^{-1} \text{ h}^{-1}$ of BD generation rate and about 10% conversion of the 0.1 mmol benzyl alcohol present in the starting solution. The AQY of benzaldehyde is 1.7% at 400 nm. On the basis of these experimental data, the proposed reaction mechanism is shown in Figure 4-5C. For the pure phase

materials, or the type-II heterojunction formed by their sub-optimal union, the Bi_2WO_6 CB and FAPbBr_3 VB simply cannot meet the redox potentials required of CO_2 -to- CO and BA-to-BD conversion, respectively. In contrast, for the Z-scheme 12.5 wt% $\text{FAPbBr}_3/\text{Bi}_2\text{WO}_6$, the photogenerated holes and electrons can be accumulated predominantly in the Bi_2WO_6 VB and FAPbBr_3 CB, respectively, to drive the efficient production of CO and BD. Beyond the photophysical characterisation presented previously (Figure 4-4). The production of CO and BD here further confirms an underlying Z-scheme mechanism in the reaction, which cannot be realized based on a simple type-II heterojunction.

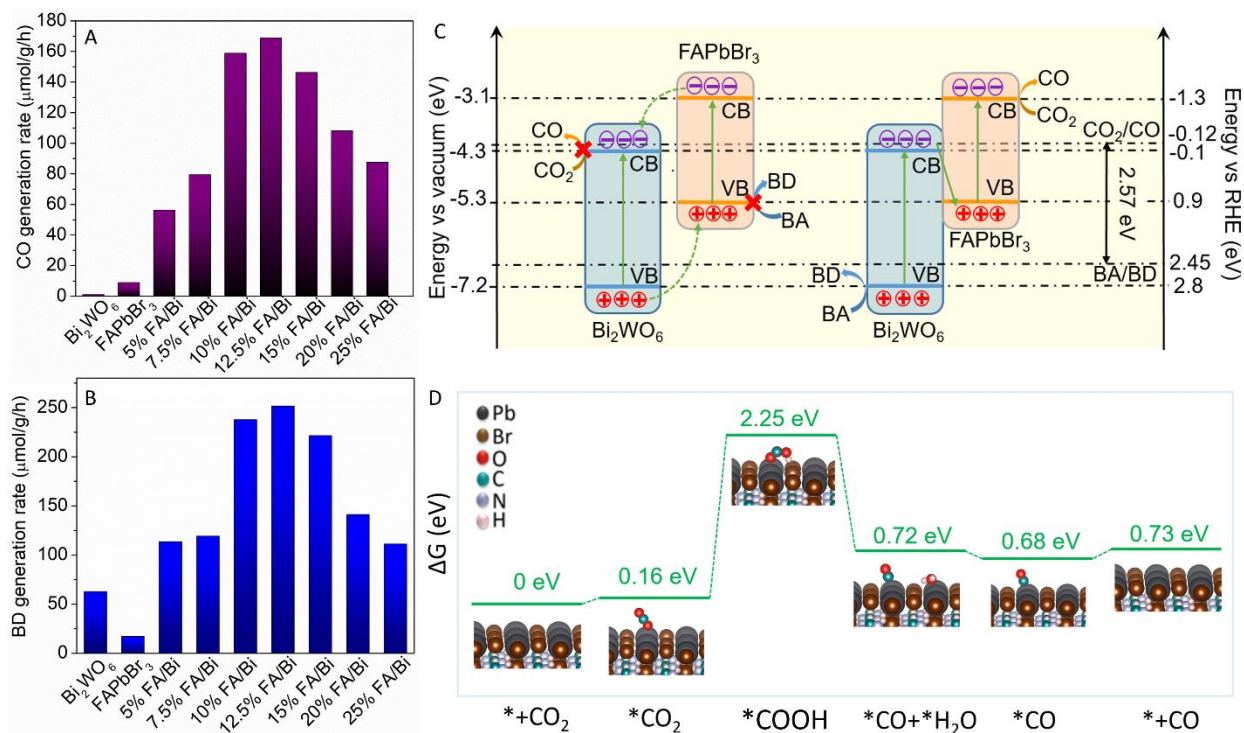
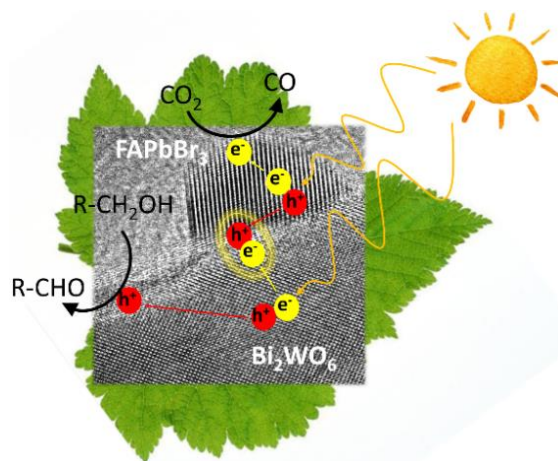


Figure 4-5. Simultaneous photocatalytic reduction of (A) CO_2 and (B) photocatalytic oxidation of BA(B) in trifluorotoluene over pure Bi_2WO_6 , FAPbBr_3 and a series of $\text{FAPbBr}_3/\text{Bi}_2\text{WO}_6$ (FA/Bi) hybrids upon solar light irradiation(1-sun, AM 1.5G filter, $100\text{mW}/\text{cm}^2$); (C)The energy diagram, charge dynamics and reaction mechanism on photocatalysts; (D)The DFT calculated potential energy diagram of CO_2 reduction on FAPbBr_3 (D).

While both the BD and CO formation rates follow generally the same trends with different FAPbBr_3 loading, the exact evolution rates do not match the expected stoichiometric ratio (i.e. 1:1). *In situ* electron spin resonance (ESR) of the optimal system (Figure 4-S11) exhibits the typical signal from superoxide radicals,³³

from traces of O₂ present in the reaction system even after flushing with CO₂. This is verified by further control experiments (Table 4-S6) and our recent work on Bi₂WO₆¹¹, where Ar is used to exclude the O₂ in the reaction system. Here we see there is BD generation on the pristine Bi₂WO₆, FAPbBr₃ and composite systems. In this scenario, the residual O₂ will consume the photo-generated electrons, which cause BD generation on pristine Bi₂WO₆ and FAPbBr₃ and reduce CO generation on the composite system.^{11,19} The stability of the composite system is tested over 5 successive cycles of catalysis (20 h in total; Figure 4-S12). The composite material here retains over 84 % of its initial activity, with the loss originating from the partial dissolution of FAPbBr₃ in the composite system (Figure 4-S13).

To develop an in-depth understanding of this reaction, at the molecular level, density functional theory (DFT) calculations are used to detail the reaction pathway of BA photo-oxidation ($C_6H_5CH_2OH + 2h^+ \rightarrow C_6H_5CHO + 2H^+$) on Bi₂WO₆ (Figure 4-S14), as well as the CO₂ reduction ($CO_2 + 2H^+ + 2e^- \rightarrow CO + H_2O$) on FAPbBr₃ (Figure 4-5D). From the change in the Gibbs free energy (Figure 4-S14), BA will be adsorbed on the Bi₂WO₆ spontaneously and is expected to follow two consecutive dehydrogenation processes; the H in OH group will dissolve first, then one H-C bond in methyl will break to finish this consecutive dehydrogenation processes, and form BD. As detailed in previous studies,³⁴⁻³⁶ the photocatalytic reduction of CO₂ is less straightforward, with two main pathways being proposed, one through hydrogenation ($CO_2 \rightarrow COOH \rightarrow \dots$) and the other via deoxygenation ($CO_2 \rightarrow CO \rightarrow \dots$).^{35,37} As suggested from our calculations in Figure 4-5D, CO₂ reduction will follow the hydrogenation pathway as the Gibbs free energy of the *COOH formation ($\Delta G(*COOH)=2.08$ eV) is substantially lower than that of the deoxygenation to form CO directly ($\Delta G(*CO + *O)=5.65$ eV) (see Figure 4-S15A for a direct comparison). Nevertheless, in the whole reaction process, the first proton-coupled electron transfer (PCET) of *COOH formation is still the rate-limiting step ($\Delta G(*COOH)=2.08$ eV). It follows that the second PCET process forming *CO and *H₂O, and the desorption of H₂O, is exothermic and spontaneous in nature. As inferred by additional DFT calculations in Figure 4-S15B, the Gibbs free energy of *CHO formation ($\Delta G(*CHO)=1.3$ eV) is markedly larger than the desorption energy of the CO molecules ($\Delta G(* + CO)=0.05$ eV). This implies that the FAPbBr₃ is more beneficial for the desorption of CO molecules from catalyst surface than for the protonation of *CO, to produce *CHO and generate hydrocarbon products. Thus, it can be concluded from our model that this reaction will only produce CO with near 100% product selectivity under solar light irradiation. Considering the full extent of details derived for this reaction, we summarize the Z-scheme photocatalytic process in Scheme 1.



Scheme 4-1. Reaction mechanism on the Z scheme photocatalyst, FAPbBr₃/Bi₂WO₆.

4.3 Conclusion

In summary, we detailed the construction and characterization of a dual Z-scheme photocatalyst FAPbBr₃/Bi₂WO₆ and evaluated its potential for artificial photosynthesis. The semi-coherent interfacing of these two semiconductors is found to yield the appropriate band structure offsets to generate a Z-scheme photocatalytic system, reaching a near-optimal balance in the carrier dynamics for a weighting of 12.5 wt% FAPbBr₃/Bi₂WO₆. Ultrafast transient infrared absorption studies confirm a Z-scheme charge transfer mechanism in this champion composition, which is capable of utilizing the reducing power of the FAPbBr₃ conduction band and the Bi₂WO₆ valence band oxidizing power. The large driving force photoredox reaction (ca. 2.57 eV) of CO₂ reduction coupled with benzyl alcohol oxidation to benzaldehyde (Scheme 1) is achieved on the 12.5 wt% FAPbBr₃/Bi₂WO₆ photocatalyst, producing CO and benzaldehyde at rates of 170 μmol g⁻¹ h⁻¹ and of 250 μmol g⁻¹ h⁻¹, respectively, under simulated solar irradiation. The apparent quantum yield at 400 nm for this system is determined at 1.2% for CO₂ reduction and 1.7% for benzyl alcohol oxidation. The turnover number (TON) of CO₂ reduction and BA oxidation at the first five cycles is 13 and 3.5, respectively. These values indicate that it is a truly catalytic reaction. In conclusion, this work not only prescribes a clear path toward using halide perovskite materials to construct Z-scheme photocatalysts with unprecedented strong redox ability, but also opens new horizons for efficient solar-to-fuel conversion of value-added materials.

4.4 Experiment section

Materials

$\text{Bi}(\text{NO}_3)_3 \cdot 5\text{H}_2\text{O}$, $\text{Na}_2\text{WO}_4 \cdot 2\text{H}_2\text{O}$ and PbBr_2 and were purchased from Aldrich and FABr was purchased from TCI. All chemicals were used without further purification.

Sample Preparation

Bi_2WO_6 were synthesized by hydrothermal method. In a typical experiment, 1mmol $\text{Na}_2\text{WO}_4 \cdot 2\text{H}_2\text{O}$, and 2 mmol $\text{Bi}(\text{NO}_3)_3 \cdot 5\text{H}_2\text{O}$ were added in 80 ml deionized water, then stir overnight. The mixed solution was poured into a 100 ml Teflon-lined autoclave. Then the autoclave was sealed into a stainless steel tank and treated at 120 °C for 24 h. The system was then allowed to cool down to room temperature naturally. Finally, the product was collected and washed several times with deionized water and dried at 60 °C in air for overnight.

Formamidinium lead bromide was synthesized by the room-temperature antisolvent precipitation method. FABr and PbBr_2 were dissolved in 10 mL of N,N-Dimethylformamide (DMF) in 1:1 molar ratio, to make a 1M precursor-solution. The precursor-solution was added dropwise into a vigorously stirred 5 ml toluene solution. The mixture was kept stirred at room temperature, resulting in an orange-red suspension. The suspension was then washed 3 times with toluene and dried in a vacuum oven at 80° C. The series of X% $\text{FAPbBr}_3/\text{Bi}_2\text{WO}_6$ (where X is equal to the wt% of FAPbBr_3) samples were synthesized by the same method. In a typical experiment, 100 mg Bi_2WO_6 was first added to 5 ml toluene solution. Then, 0.025 ml precursor-solution was added into the vigorously stirred Bi_2WO_6 toluene suspension. The mixture was kept stirring at room temperature for 2 h. The suspension was then washed with toluene for 3 times by centrifugation and dried in vacuum oven at 80° C to produce the samples referred to as 12.5% $\text{FAPbBr}_3/\text{Bi}_2\text{WO}_6$.

Sample Characterization

X-ray diffractometry (XRD) measurements were performed on a Stoe X-ray diffractometer using Cu K α 1 radiation ($\lambda = 1.5406 \text{ \AA}$). Scanning electron microscopy (SEM) images of samples were taken with a FEI-Q FEG250 system. Transmission electron microscopy (TEM) images of samples were obtained over JEOL ARM200F. X-ray photoelectron spectroscopy (XPS) data were recorded on a VG ESCALAB XPS System with a monochromatized Al K α X-ray sources (15 kV, 200 W 500 μm pass energy = 20 eV). All binding energies were referenced to the C1s peak at 284.6 eV of surface adventitious carbon. The optical absorption spectra of the samples were studied by the Lambda-950 UV-vis spectrometer. The steady-state photoluminescence was recorded on an Edinburgh FLS980, from 500 to 600 nm with 1 nm increments and 1 s integration time, under an excitation wavelength of 360 nm and 485nm. Electron spin resonance spectra were obtained over Bruker ESP 300 E electron paramagnetic resonance spectrometer. Ultraviolet photoelectron spectroscopy(UPS) were recorded on ThermoFisher ESCALAB 250xi. Transient absorption spectroscopy in nanosecond time-resolved was performed on the Nd:YAG laser (Quanta Ray, Spectra-Physics, 10 Hz), the tuning excitation light was achieved by an optical parametric oscillator (OPO, GWU premiScan-ULD/240, Spectra-Physics). The probe light ($2,090 \text{ cm}^{-1}$) came from a quantum cascade laser (Daylight Solutions). As for femtosecond time-resolved IR absorption spectroscopy, Ti:Sapphire laser was used as a laser source (Spitfire Ace, Spectra-Physics, 35 fs, 1 kHz). Then the laser was split into two beams, one of them guided to the optical parameters amplifier (TOPAS, Spectra-Physics) to generate the pump light and the other is utilized to generate the super-continuum probe light. The signals were collected by a spectrometer (iHR 320, HORIBA Jobin Yvon) and acquired by the MCT detector (FPAS-0144, Infrared Systems Development). The central wavelength was set to be 5,000 nm as the signal to noise ratio was the best.

Photocatalytic Activity Measurements

All photocatalytic reactions were conducted in a 20 mL quartz reactor and with a magnetic stirring rod (500 rpm). The specific procedure was as follows: 0.01 g photocatalyst, 0,1mmol benzyl alcohol, 2.5 mL trifluorotoluene prior to being flushed with Ar and molecular carbon dioxide for 1h, respectively, were loaded into the reactor and filled with CO $_2$, then the whole system was sealed up. The mixture was irradiated with a 150 W Xe lamp with AM 1.5G filter to simulate the solar light spectrum(100 mW/cm^2). After irradiation of 4 h, the headspace gas was analyzed by Agilent 7890B equipped with a TCD detector, an FID detector, a methane converter, and two chromatographic columns of MolSieve 5A and Porapak Q

column. The suspension was centrifuged at 10000 rpm for 10 min and the liquid was analyzed by Shimadzu GC-2010 equipped with an FID detector and CP Sil-5 column.

UPS calculation

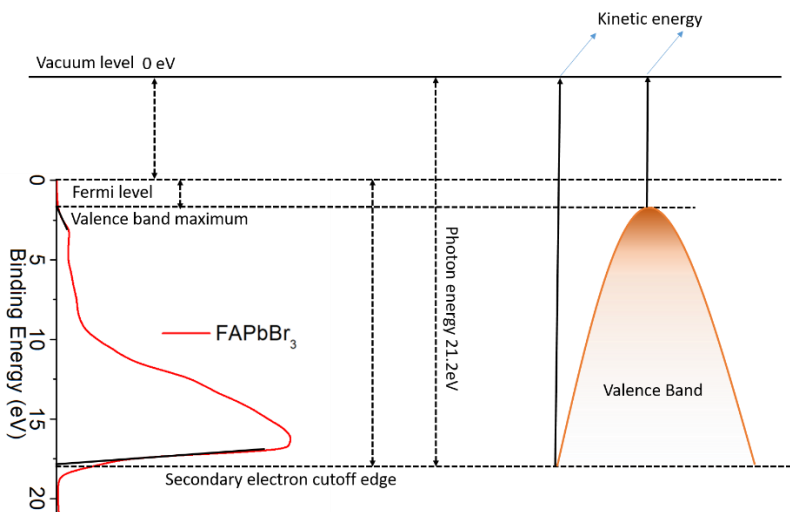


Figure 4-6. Schematic of valence band and Fermi level estimation from UPS.

Due to the low energy of the used UV photons (ca. 58.5 nm), UPS only detects the kinetic energy of the valence electrons. Based on the kinetic energy and photon energy, we can obtain the binding energy of the electrons. After calibrated with Au, the zero point of the binding energy spectrum was fixed at the Fermi level. For semiconductors, there are no electrons at the Fermi level. The signal will start raising when reaching the VB maximum as electrons can get removed from the atoms. We can obtain the position of VBM (vs Fermi level) from the tangent of the rising phase. Also, from the tangent of the declining phase, we can obtain the secondary electron cutoff edge where the kinetic energy is zero and the photon energy is equal to the energy that the electron escapes to the vacuum energy level.

$$\text{Fermi level(vs Vac)} = \text{photon energy} - \text{secondary electron cutoff edge}$$

The value of the secondary electron cutoff edge can be obtained from the UPS spectrum. The He I photon energy is 21.2 eV

$$\text{Valence band(vs Vac)} = \text{Work function(vs Vac)} - \text{Valence band(vs } E_f)$$

Valence band(vs E_f) can be obtained from the spectrum.

Conduction band(vs Vac) = Valence band(vs Vac)+ Bandgap(eV)

The Bandgap can be obtained from DRS.

$$E_{\text{RHE}} \text{ (eV)} = -E_{\text{vac}} - 4.4$$

DFT calculation

Vienna Ab-initio Simulation Package (VASP) code was employed for density functional theory (DFT) calculations. Projector-augmented wave (PAW) method was used to treat the interaction of valence electron and core. The cut-off energy was set to 450 eV. The electronic exchange-correlation functional was performed with Perdew-Burke-Ernzerhof (PBE) of generalized gradient approximation (GGA), and it was considered that the geometry was optimized when the force was less than 0.02 eV/Å. The slab was blocked by a vacuum layer with a thickness of 15Å to prevent interaction. The gamma k-point was used to perform the integration of Brillouin-zone and the calculation accuracy can be achieved. Data processing took advantage of the VASPKIT script. Transition states of elementary reactions were searched by Climbing- nudged elastic band (C-NEB) method. The Gibbs free energy of molecules were obtain from the CCCBDB database [<http://cccbdb.nist.gov/>].

The Gibbs energy of the reaction was defined as:

$$G = H - TS = U - T\Delta S = E_{\text{DFT}} + E_{\text{ZPE}} - T\Delta S$$

Where E_{DFT} were obtain from the output file of VASP, the zero point of E_{ZPE} were obtained from the calculation of the frequency of surface adsorption. Data processing took advantage of the VASPKIT script.

Calculation of the apparent quantum efficiency (AQE) of CO₂ reduction and/or benzyl alcohol oxidation

The apparent quantum efficiency is defined by the ratio of the effective electrons and holes used for reduction (CO generation) and oxidation (BD production) to the total output photon flux(not absorbed photon flux) from the light source. The reduction of CO₂ molecules to CO molecule requires two electrons, as well the oxidation of BA molecules to BD molecule requires two holes:

$$\text{AQE \%} = \text{Effective charge carriers/Total output photons} \times 100\% = (2 \times Y \times N)/(\Theta \times T \times S) \times 100\%$$

Where Y is the yield of CO or BD in the sample, N is Avogadro's number, T is the irradiation time, Θ is the photon flux and S is the illumination area.

Here, 400 nm bandpass filter is integrated into the light source. We take this as monochromatic light centred at 400 nm, and the light intensity (I) can be measured by a photometer. This is actually an underestimation of the real number number of visible light photons in the experiment.

The Θ at 400 nm can be calculated by $\Theta = I / E_{400nm}$, $I = 8 \text{ mJ s}^{-1} \text{ cm}^{-2}$, $E_{400nm} = h\nu = hc/\lambda$

The following calculation example is based on the data from BA photo-oxidation for 4 h:

$Y = 8.1 \times 10^{-6} \text{ mol}$, $N = 6.022 \times 10^{23} \text{ mol}^{-1}$, $T = 4 \text{ h}$, $S = 2.5 \text{ cm}^2$; $\Theta = 1.61 \times 10^{16} \text{ s}^{-1} \text{ cm}^{-2}$ at 400 nm.

$\text{AQE}\% = (2 \times 8.1 \times 10^{-6} \times 6.022 \times 10^{23}) / (1.61 \times 10^{16} \times 4 \times 3,600 \times 2.5) = 1.7\%$.

Similarly, the quantum efficiency of CO was calculated to be $\sim 1.2\%$. The difference was attributed to traces of oxygen present in the sample which can consume the photo-generated electrons.

Turnover Number(TON) Calculation

$\text{TON}(\text{BD}) = \text{sum of the molar of benzaldehyde in 5 cycles} / \text{the molar of Bi}_2\text{WO}_6 \text{ in 10 mg catalyst}$

$\text{TON}(\text{CO}) = \text{sum of the molar of CO in 5 cycles} / \text{the molar of perovskite in 10 mg catalyst}$

4.5 References

- (1) Brenner, T. M.; Egger, D. A.; Kronik, L.; Hodes, G.; Cahen, D. Hybrid organic-inorganic perovskites: low-cost semiconductors with intriguing charge-transport properties. *Nat. Rev. Mater.* **2016**, *1*, 16.
- (2) Park, S.; Chang, W. J.; Lee, C. W.; Park, S.; Ahn, H.-Y.; Nam, K. T. Photocatalytic hydrogen generation from hydriodic acid using methylammonium lead iodide in dynamic equilibrium with aqueous solution. *Nat. Energy* **2016**, *2*, 16185.
- (3) Ou, M.; Tu, W.; Yin, S.; Xing, W.; Wu, S.; Wang, H.; Wan, S.; Zhong, Q.; Xu, R. Amino-Assisted Anchoring of CsPbBr₃ Perovskite Quantum Dots on Porous g-C₃N₄ for Enhanced Photocatalytic CO₂ Reduction. *Angew. Chem.* **2018**, *130*, 13758-13762.

- (4) Xu, Y. F.; Yang, M. Z.; Chen, B. X.; Wang, X. D.; Chen, H. Y.; Kuang, D. B.; Su, C. Y. A CsPbBr₃ Perovskite Quantum Dot/Graphene Oxide Composite for Photocatalytic CO₂ Reduction. *J. Am. Chem. Soc.* **2017**, *139*, 5660-5663.
- (5) Wu, L.-Y.; Mu, Y.-F.; Guo, X.-X.; Zhang, W.; Zhang, Z.-M.; Zhang, M.; Lu, T.-B. Encapsulating Perovskite Quantum Dots in Iron-Based Metal-Organic Frameworks (MOFs) for Efficient Photocatalytic CO₂ Reduction. *Angew. Chem. Int. Ed.* **2019**, *58*, 9491-9495.
- (6) Xu, Q.; Zhang, L.; Yu, J.; Wageh, S.; Al-Ghamdi, A. A.; Jaroniec, M. Direct Z-scheme photocatalysts: Principles, synthesis, and applications. *Mater. Today* **2018**, *21*, 1042-1063.
- (7) Li, H.; Tu, W.; Zhou, Y.; Zou, Z. Z-Scheme Photocatalytic Systems for Promoting Photocatalytic Performance: Recent Progress and Future Challenges. *Adv. Sci.* **2016**, *3*, 1500389.
- (8) Zhou, Y. G.; Zhang, Y. F.; Lin, M. S.; Long, J. L.; Zhang, Z. Z.; Lin, H. X.; Wu, J. C. S.; Wang, X. X. Monolayered Bi₂WO₆ nanosheets mimicking heterojunction interface with open surfaces for photocatalysis. *Nat. Commun.* **2015**, *6*, 8340.
- (9) Liang, L.; Lei, F.; Gao, S.; Sun, Y.; Jiao, X.; Wu, J.; Qamar, S.; Xie, Y. Single Unit Cell Bismuth Tungstate Layers Realizing Robust Solar CO₂ Reduction to Methanol. *Angew. Chem. Int. Ed.* **2015**, *54*, 13971-13974.
- (10) Hu, J.; Chen, D.; Mo, Z.; Li, N.; Xu, Q.; Li, H.; He, J.; Xu, H.; Lu, J. Z-Scheme 2D/2D Heterojunction of Black Phosphorus/Monolayer Bi₂WO₆ Nanosheets with Enhanced Photocatalytic Activities. *Angew. Chem.* **2019**, *131*, 2095-2099.
- (11) Huang, H.; Zhou, C.; Jiao, X.; Yuan, H.; Zhao, J.; He, C.; Hofkens, J.; Roeffaers, M. B. J.; Long, J.; Steele, J. A. Subsurface Defect Engineering in Single-Unit-Cell Bi₂WO₆ Monolayers Boosts Solar-Driven Photocatalytic Performance. *ACS Catal.* **2019**, 1439-1443.
- (12) Yuan, L.; Weng, B.; Colmenares, J. C.; Sun, Y.; Xu, Y.-J. Multichannel Charge Transfer and Mechanistic Insight in Metal Decorated 2D–2D Bi₂WO₆–TiO₂ Cascade with Enhanced Photocatalytic Performance. *Small* **2017**, *13*, 1702253.
- (13) Cen, G.; Liu, Y.; Zhao, C.; Wang, G.; Fu, Y.; Yan, G.; Yuan, Y.; Su, C.; Zhao, Z.; Mai, W. Atomic-Layer Deposition-Assisted Double-Side Interfacial Engineering for High-Performance Flexible and Stable CsPbBr₃ Perovskite Photodetectors toward Visible Light Communication Applications. *Small* **2019**, *15*, 1902135.
- (14) Meng, L.; Yao, E.-P.; Hong, Z.; Chen, H.; Sun, P.; Yang, Z.; Li, G.; Yang, Y. Pure Formamidinium-Based Perovskite Light-Emitting Diodes with High Efficiency and Low Driving Voltage. *Adv. Mater.* **2017**, *29*, 1603826.

- (15) Reisner, E. When Does Organic Photoredox Catalysis Meet Artificial Photosynthesis? *Angew. Chem. Int. Ed.* **2019**, *58*, 3656-3657.
- (16) Guo, Q.; Liang, F.; Li, X.-B.; Gao, Y.-J.; Huang, M.-Y.; Wang, Y.; Xia, S.-G.; Gao, X.-Y.; Gan, Q.-C.; Lin, Z.-S.; Tung, C.-H.; Wu, L.-Z. Efficient and Selective CO₂ Reduction Integrated with Organic Synthesis by Solar Energy. *Chem* **2019**, *5*, 2605-2616.
- (17) Global Benzaldehyde Market Research Report - Forecast to 2022, <https://markets.businessinsider.com/news/stocks/global-benzaldehyde-market-research-report-forecast-to-2022-1023748543>.
- (18) Sheldon, R. A.; Arends, I.; Ten Brink, G. J.; Dijkstra, A. Green, catalytic oxidations of alcohols. *Acc. Chem. Res.* **2002**, *35*, 774-781.
- (19) Huang, H.; Yuan, H.; Janssen, K. P. F.; Solís-Fernández, G.; Wang, Y.; Tan, C. Y. X.; Jonckheere, D.; Debroye, E.; Long, J.; Hendrix, J.; Hofkens, J.; Steele, J. A.; Roeffaers, M. B. J. Efficient and Selective Photocatalytic Oxidation of Benzylic Alcohols with Hybrid Organic–Inorganic Perovskite Materials. *ACS Energy Lett.* **2018**, *3*, 755-759.
- (20) Schünemann, S.; van Gastel, M.; Tüysüz, H. A CsPbBr₃/TiO₂ Composite for Visible-Light-Driven Photocatalytic Benzyl Alcohol Oxidation. *ChemSusChem* **2018**, *11*, 2057-2061.
- (21) Luo, N.; Montini, T.; Zhang, J.; Fornasiero, P.; Fonda, E.; Hou, T.; Nie, W.; Lu, J.; Liu, J.; Heggen, M.; Lin, L.; Ma, C.; Wang, M.; Fan, F.; Jin, S.; Wang, F. Visible-light-driven coproduction of diesel precursors and hydrogen from lignocellulose-derived methylfurans. *Nat. Energy* **2019**, *4*, 575-584.
- (22) Kuehnel, M. F.; Reisner, E. Solar Hydrogen Generation from Lignocellulose. *Angew. Chem. Int. Ed.* **2018**, *57*, 3290-3296.
- (23) Huang, H.; Yuan, H.; Zhao, J.; Solís-Fernández, G.; Zhou, C.; Seo, J. W.; Hendrix, J.; Debroye, E.; Steele, J. A.; Hofkens, J.; Long, J.; Roeffaers, M. B. J. C(sp³)–H Bond Activation by Perovskite Solar Photocatalyst Cell. *ACS Energy Lett.* **2018**, *4*, 203-208.
- (24) Wang, X.-D.; Huang, Y.-H.; Liao, J.-F.; Jiang, Y.; Zhou, L.; Zhang, X.-Y.; Chen, H.-Y.; Kuang, D.-B. *In Situ* Construction of a Cs₂SnI₆ Perovskite Nanocrystal/SnS₂ Nanosheet Heterojunction with Boosted Interfacial Charge Transfer. *J. Am. Chem. Soc.* **2019**, *141*, 13434-13441.
- (25) Bagus, P. S.; Ilton, E. S.; Nelin, C. J. *Surf. Sci. Rep.* **2013**, *68*, 273-304.
- (26) Hanusch, F. C.; Wiesenmayer, E.; Mankel, E.; Binek, A.; Angloher, P.; Fraunhofer, C.; Giesbrecht, N.; Feckl, J. M.; Jaegermann, W.; Johrendt, D.; Bein, T.; Docampo, P. *J. Phys. Chem. Lett.* **2014**, *5*, 2791-2795.

- (27) Girish Kumar, S.; Koteswara Rao, K. S. R. The interpretation of XPS spectra: Insights into materials properties. *Appl. Surf. Sci.* **2015**, *355*, 939-958.
- (28) Amano, F.; Yamakata, A.; Nogami, K.; Osawa, M.; Ohtani, B. Visible Light Responsive Pristine Metal Oxide Photocatalyst: Enhancement of Activity by Crystallization under Hydrothermal Treatment. *J. Am. Chem. Soc.* **2008**, *130*, 17650-17651.
- (29) Huang, H. W.; Lin, J. J.; Zhu, G. B.; Weng, Y. X.; Wang, X. X.; Fu, X. Z.; Long, J. L. A Long-Lived Mononuclear Cyclopentadienyl Ruthenium Complex Grafted onto Anatase TiO₂ for Efficient CO₂ Photoreduction. *Angew. Chem. Int. Ed.* **2016**, *55*, 8314-8318.
- (30) Grigioni, I.; Abdellah, M.; Corti, A.; Dozzi, M. V.; Hammarström, L.; Selli, E. Photoinduced Charge-Transfer Dynamics in WO₃/BiVO₄ Photoanodes Probed through Midinfrared Transient Absorption Spectroscopy. *J. Am. Chem. Soc.* **2018**, *140*, 14042-14045.
- (31) Grigioni, I.; Stamplecoskie, K. G.; Jara, D. H.; Dozzi, M. V.; Oriana, A.; Cerullo, G.; Kamat, P. V.; Selli, E. Wavelength-Dependent Ultrafast Charge Carrier Separation in the WO₃/BiVO₄ Coupled System. *ACS Energy Lett.* **2017**, *2*, 1362-1367.
- (32) Zhu, M.; Sun, Z.; Fujitsuka, M.; Majima, T. Z-Scheme Photocatalytic Water Splitting on a 2D Heterostructure of Black Phosphorus/Bismuth Vanadate Using Visible Light. *Angew. Chem. Int. Ed.* **2018**, *57*, 2160-2164.
- (33) Dvoranova, D.; Barbierikova, Z.; Brezova, V. Radical Intermediates in Photoinduced Reactions on TiO₂ (An EPR Spin Trapping Study). *Molecules* **2014**, *19*, 17279-17304.
- (34) Ji, Y.; Luo, Y. Theoretical Study on the Mechanism of Photoreduction of CO₂ to CH₄ on the Anatase TiO₂(101) Surface. *ACS Catal.* **2016**, *6*, 2018-2025.
- (35) Wang, Y.; Zhang, Z.; Zhang, L.; Luo, Z.; Shen, J.; Lin, H.; Long, J.; Wu, J. C. S.; Fu, X.; Wang, X.; Li, C. Visible-Light Driven Overall Conversion of CO₂ and H₂O to CH₄ and O₂ on 3D-SiC@2D-MoS₂ Heterostructure. *J. Am. Chem. Soc.* **2018**, *140*, 14595-14598.
- (36) Fan, W.; Zhang, Q.; Wang, Y. Semiconductor-based nanocomposites for photocatalytic H₂ production and CO₂ conversion. *Phys. Chem. Chem. Phys.* **2013**, *15*, 2632-2649.
- (37) Xie, C.; Niu, Z.; Kim, D.; Li, M.; Yang, P. Surface and Interface Control in Nanoparticle Catalysis. *Chem. Rev.* **2019**, <https://doi.org/10.1021/acs.chemrev.9b00220>.

4.6 Supporting information

Supporting figures

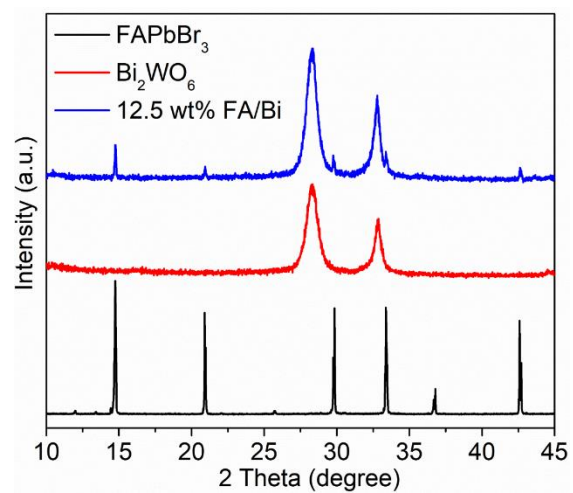


Figure 4-S1. XRD patterns of FAPbBr_3 , Bi_2WO_6 and 12.5% $\text{FAPbBr}_3/\text{Bi}_2\text{WO}_6$ (FA/Bi).

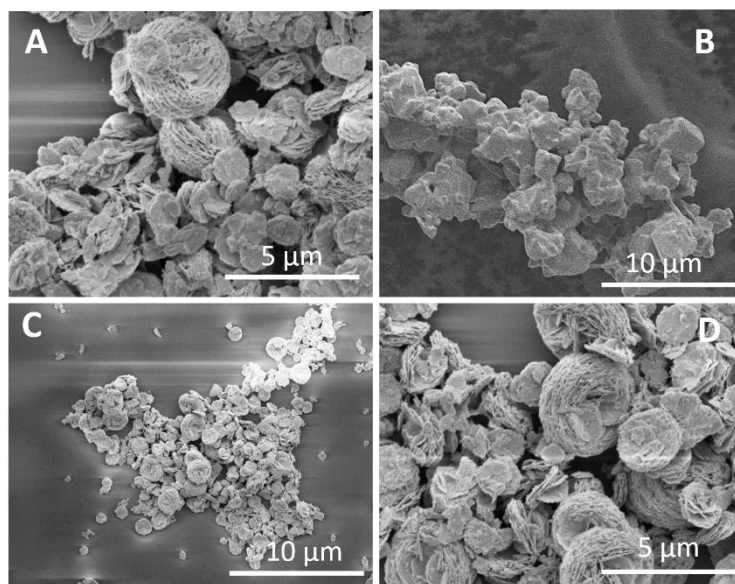


Figure 4-S2. SEM patterns of (A) Bi_2WO_6 , (B) FAPbBr_3 , (C) and (D) 12.5% FA/Bi.

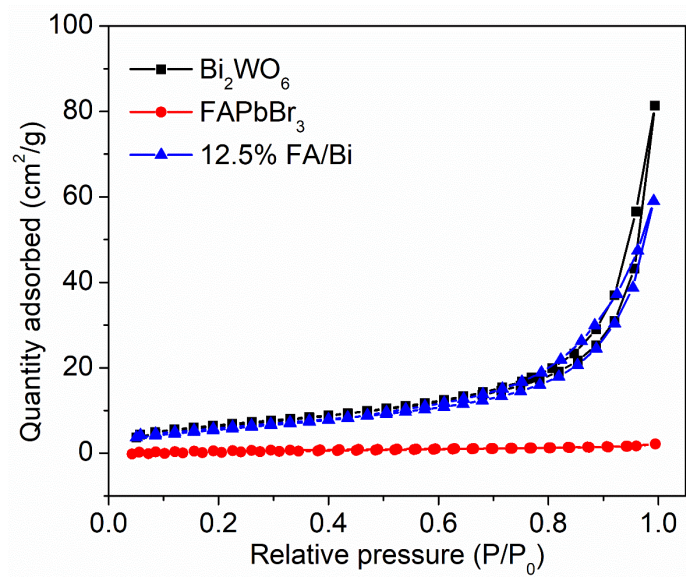


Figure 4-S3. N₂ adsorption-desorption isotherms of Bi₂WO₆, FAPbBr₃, and 12.5% FA/Bi.

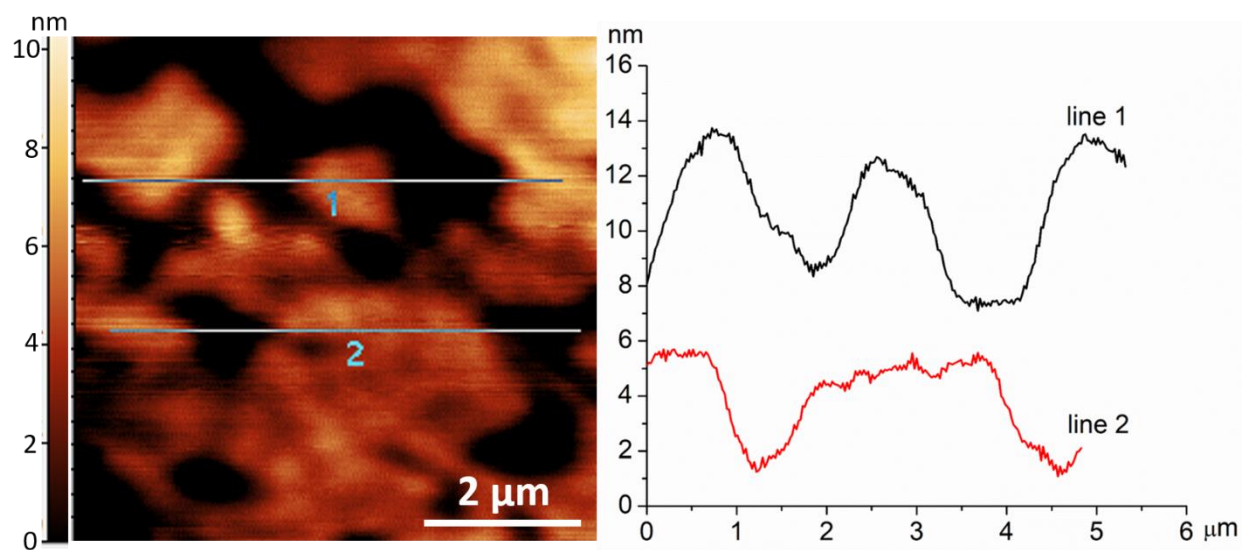


Figure 4-S4. AFM micrograph of Bi₂WO₆, and the corresponding height profiles.

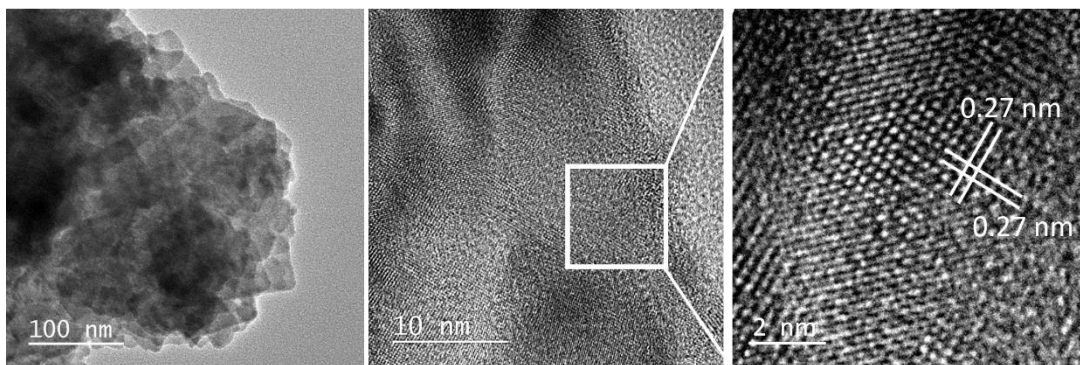


Figure 4-S5. TEM and HRTEM pattern of Bi_2WO_6 .

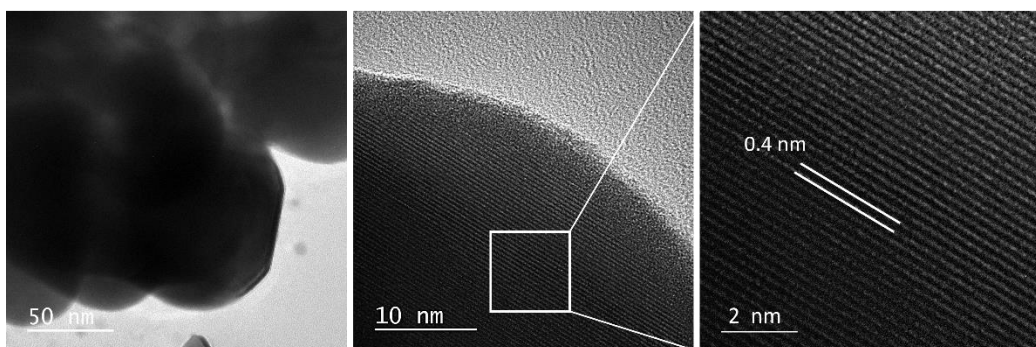


Figure 4-S6. TEM and HRTEM pattern of FAPbBr_3 .

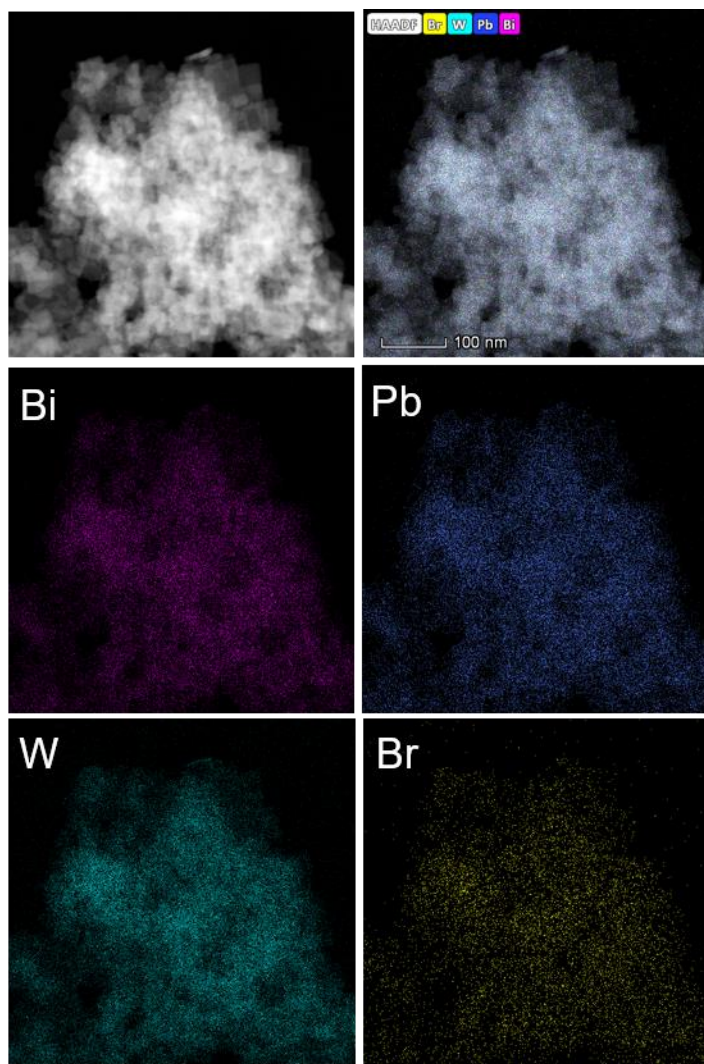


Figure 4-S7. Elemental mapping pattern of the 12.5% FA/Bi photocatalyst. Based on the EDX element mapping pattern, we further confirm the distribution relationship and intimate contact of these two components.

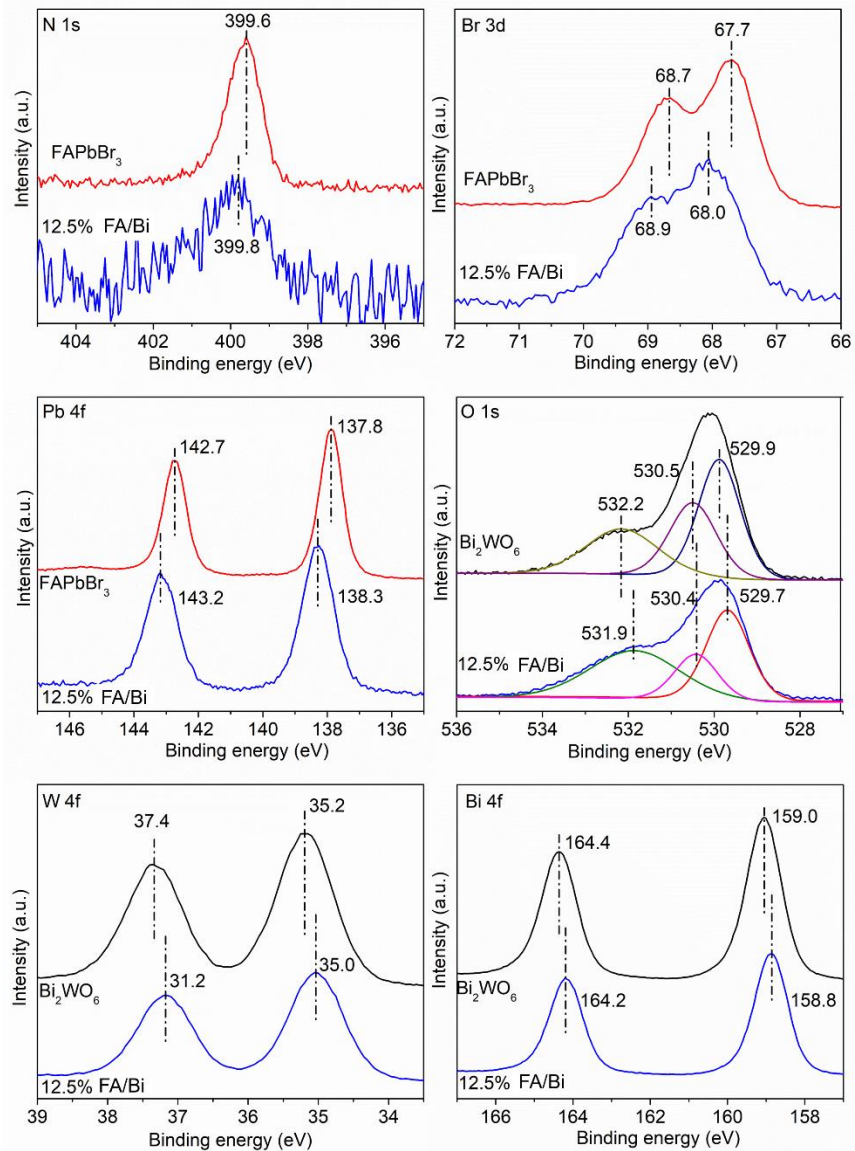


Figure 4-S8. XPS spectra of N 1s, Br 3d and Pb 4f and in FAPbBr₃ and 12.5%FA/Bi and O1s, W4f and Bi4f in Bi₂WO₆ and 12.5%FA/Bi.

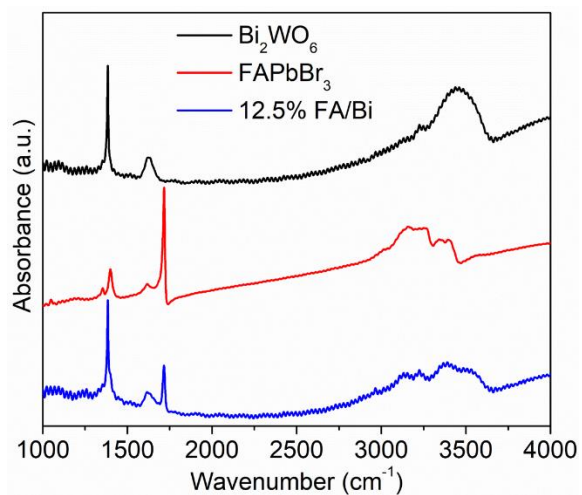


Figure 4-S9. FTIR spectra of Bi_2WO_6 , FAPbBr_3 and 12.5% FA/Bi.

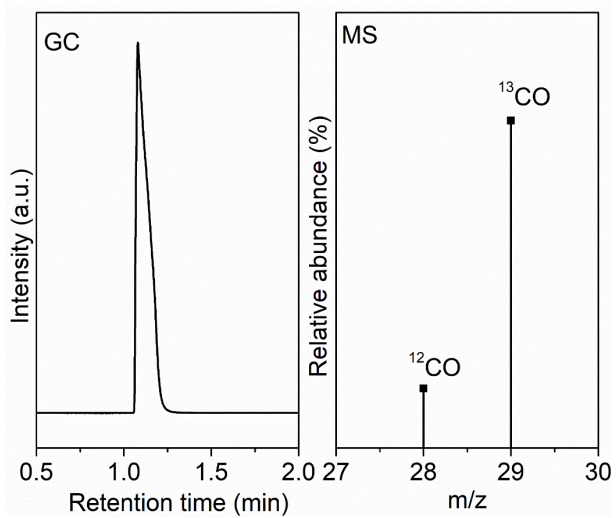


Figure 4-S10. Results of GC-MS analysis of the CO generated from $^{13}\text{CO}_2$ isotope experiment.

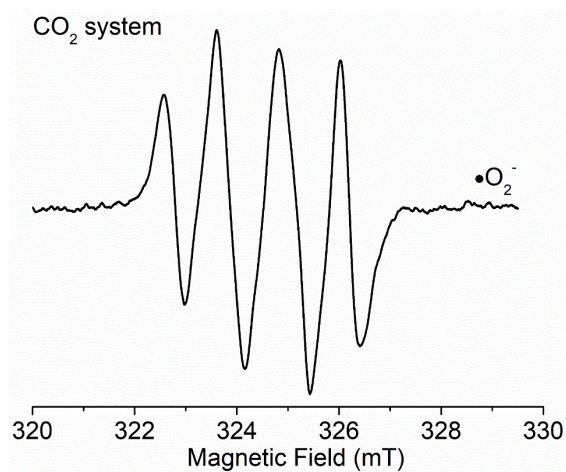


Figure 4-S11. DMPO-trapped superoxide radical of 12.5% FA/Bi in CO₂ flashed trifluorotoluene.

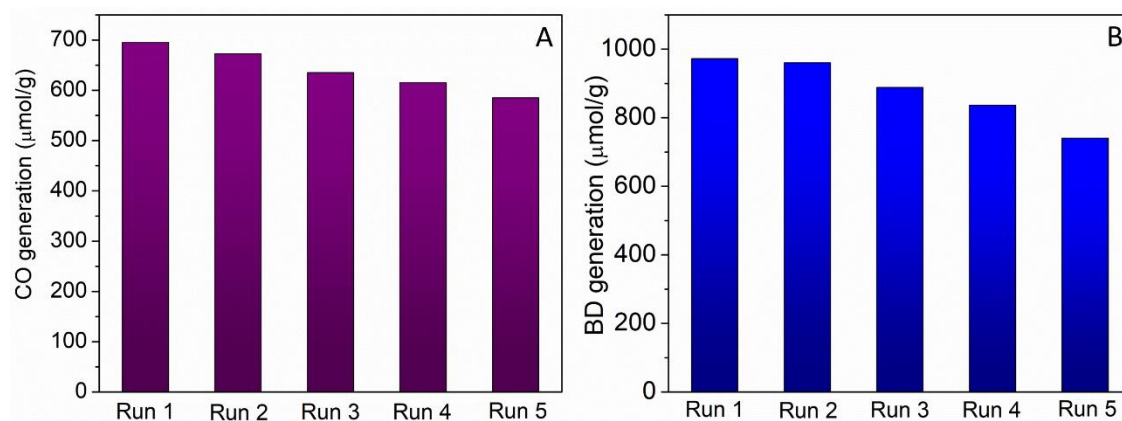


Figure 4-S12. Recycle test for 12.5% FA/Bi. Reaction conditions: benzyl alcohol (0.1 mmol), photocatalysts (0.01 g), solvent of trifluorotoluene (2.5 mL) saturated with CO₂, AM1.5G simulated light irradiation, 100mW/cm², irradiation time (4 h).

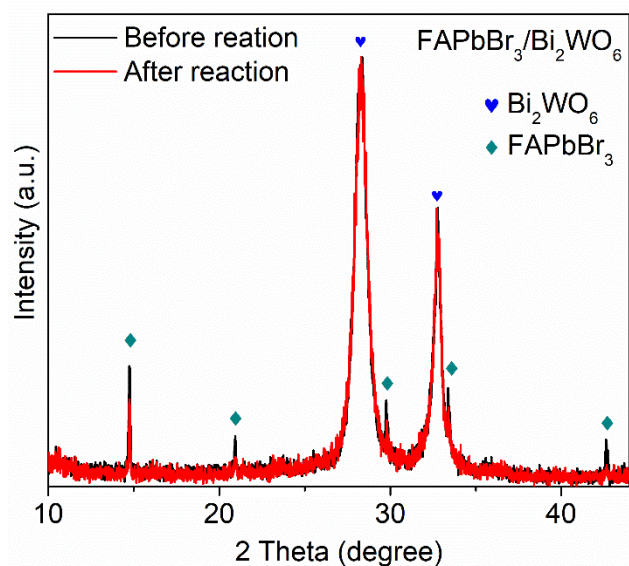


Figure 4-S13. XRD pattern of 12.5% FA/Bi after 5 cycle reaction (20h). no any new peak will appearance in the XRD pattern, but the intensity of the peaks belonging to FAPbBr₃ is weaker.

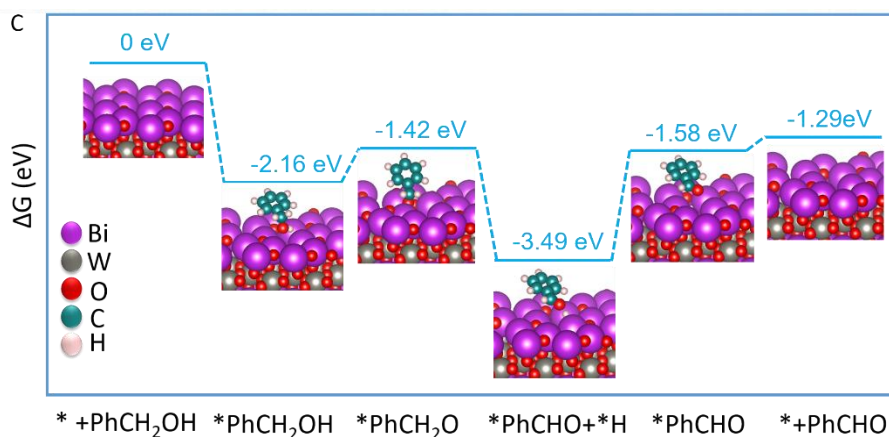


Figure 4-S14. The DFT calculated potential energy diagram of benzyl alcohol oxidation on Bi₂WO₆

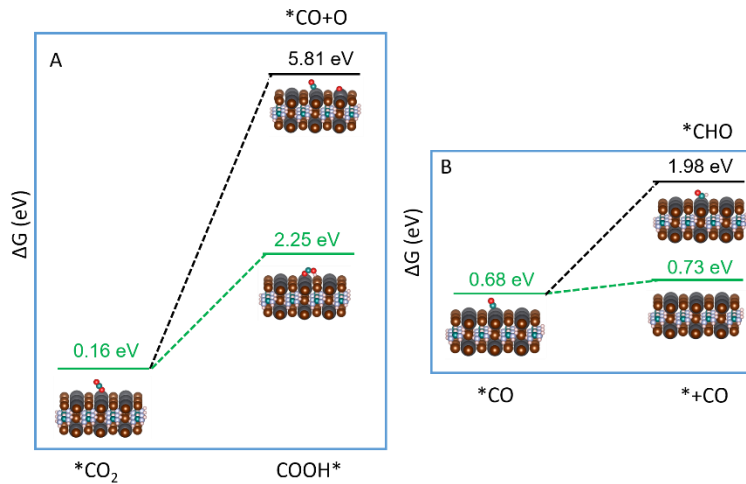


Figure 4-S15. Steps are crucial to determining the reaction pathway(A) and selectivity(B) to CO for FA/Bi.

Supporting tables

Table 4-S1 BET surface area of Bi_2WO_6 , $FAPbBr_3$ and 12.5% FA/Bi.

Sample	BET surface area (m^2/g)
Bi_2WO_6	25.4
$FAPbBr_3$	2.7
12.5% FA/Bi	22.3

Table 4-S2. The fit results of fs-ps IR kinetic traces of Bi_2WO_6 , $FAPbBr_3$ and 12.5% FA/Bi at 2090 cm^{-1} excited by 470 nm pump light.

Sample	$A_1/\tau_1(ps)$	$A_2/\tau_2(ps)$
Bi_2WO_6	-	-
$FAPbBr_3$	0.55/4.4	0.45/48.2
FA/Bi	0.81/16.6	0.3/144.6

Table 4-S3. The fit results of the raising phase in fs-ps IR kinetic traces of Bi₂WO₆, FAPbBr₃ and 12.5% FA/Bi at 2090 cm⁻¹ excited by 360 and 470 nm pump light.

Sample	$\tau(360\text{nm})$	$\tau(470\text{nm})$
Bi ₂ WO ₆	-	-
FAPbBr ₃	-	0.07 ps
FA/Bi	-	0.8 ps

Table 4-S4. The fit results of fs-ps IR kinetic traces of Bi₂WO₆, FAPbBr₃ and 12.5% FA/Bi at 2090 cm⁻¹ excited by 360 nm pump light.

Sample	A ₁ /τ ₁ (ps)	A ₂ /τ ₂ (ps)	A ₃ /τ ₃ (ns)
Bi ₂ WO ₆	0.000474/3.45	0.000227/95.2	0.000245/>3
FAPbBr ₃	0.008175/3.39	0.004996/34.3	-/>3
FA/Bi	0.000731/3.44	0.000281/66.6	0.000205/>3

Table 4-S5. The fit results of ns-μs IR kinetic traces of Bi₂WO₆, FAPbBr₃ and 12.5% FA/Bi at 2090 cm⁻¹ excited by 360 nm pump light.

Sample	A ₁ /τ ₁ (μs)	A ₂ /τ ₂ (μs)	A ₃ /τ ₃ (ms)
Bi ₂ WO ₆	-	0.579/34.0	0.424/1.07
FAPbBr ₃	-	-	0.799/1.53
FA/Bi	0.106/5.9	0.249/47.0	0.663/1.99

Table 4-S6. The amount of CO and benzaldehyde generation in different conditions.

Sample	CO evolution rate ($\mu\text{mol/g/h}$)	Benzaldehyde ($\mu\text{mol/g/h}$)	Reaction condition
FAPbBr ₃	12.5	18	AM1.5 fliter, 100mW/cm ² , CO ₂ , benzyl alcohol
FAPbBr ₃	10	16	AM1.5 fliter, 100mW/cm ² , Ar, benzyl alcohol
FAPbBr ₃	<5	<5	CO ₂ , benzyl alcohol, without light,
FAPbBr ₃	11	<5	AM1.5 fliter, 100mW/cm ² , Ar, no benzyl alcohol
Bi ₂ WO ₆	<5	63	AM1.5 fliter, 100mW/cm ² , CO ₂ , benzyl alcohol
FA/Bi	170	250	AM1.5 fliter, 100mW/cm ² , CO ₂ , benzyl alcohol
FA/Bi	<5	<5	CO ₂ , benzyl alcohol, without light
FA/Bi	13	<5	AM1.5 fliter, 100mW/cm ² , Ar, no benzyl alcohol
FA/Bi	15	<5	AM1.5 fliter, 100mW/cm ² , CO ₂ , no benzyl alcohol
FA/Bi	12	130	AM1.5 fliter, 100mW/cm ² , Ar, benzyl alcohol

FA/Bi	-	580	AM1.5 100mW/cm ² , O ₂ , benzyl alcohol	fliter,
-------	---	-----	---	---------

Table 4-S7. Photocatalytic reduction CO₂ to fuels over various photocatalysts under different experimental conditions.

Sample	Production(production rate ($\mu\text{mol/g/h}$))	Reaction condition	Reference
FA/Bi	CO(170)	AM1.5G 100mW/cm ²	fliter, This work
CsPbBr ₃ QD	CO(4.2) CH ₄ (1.9)	100-W Xe lamp, AM 1.5G filter	³
CsPbBr ₃ QD/GO	CO(5) CH ₄ (2.5)	100-W Xe lamp, AM 1.5G filter	³
Cs ₂ AgBiBr ₆	CO(2.35) CH ₄ (1.6)	AM 1.5G filter, 150 mW/cm ²	⁵
CsPb(Br _x /Cl _{1-x}) ₃	CO(87) CH ₄ (12)	300 W Xe lamp.AM 1.5G filter	⁶
CsPbBr ₃ QDs/UiO- 66(NH ₂)	CO(8)	300 W Xe lamp, 420nm cut-off	⁷
CsPbBr ₃ NC/a-TiO ₂	CO(7) CH ₄ (4)	AM 1.5G filter, 150 mW/cm ²	⁸
CsPbBr ₃ @ZIF-67	CO(1) CH ₄ (3)	AM 1.5G, 150 mW/cm ²	⁹
CsPbBr ₃ QDs/g-C ₃ N ₄	CO(148.9)	300 W Xe lamp, 420 nm cut-off	¹⁰
CsPbBr ₃ /ZnO/GO	CO(1) CH ₄ (6)	AM 1.5G, 150 mW/cm ²	¹¹
MAPbI ₃ @PCN- 221(Fe0.2)	CO(4.16) CH ₄ (13)	300 W Xe lamp, 100 mW/cm ²	¹²
Cs ₂ SnI ₆ /SnS ₂	CH ₄ (6.09)	150 mW/cm ² , 400 nm filter	¹³

Reference

- (1) Protesescu, L.; Yakunin, S.; Bodnarchuk, M. I.; Bertolotti, F.; Masciocchi, N.; Guagliardi, A.; Kovalenko, M. V. *J. Am. Chem. Soc.* **2016**, *138*, 14202.
- (2) Huang, H.; Yuan, H.; Janssen, K. P. F.; Solís-Fernández, G.; Wang, Y.; Tan, C. Y. X.; Jonckheere, D.; Debroye, E.; Long, J.; Hendrix, J.; Hofkens, J.; Steele, J. A.; Roeffaers, M. B. J. Efficient and Selective Photocatalytic Oxidation of Benzylic Alcohols with Hybrid Organic–Inorganic Perovskite Materials. *ACS Energy Lett.* **2018**, 755-759.
- (3) Xu, Y. F.; Yang, M. Z.; Chen, B. X.; Wang, X. D.; Chen, H. Y.; Kuang, D. B.; Su, C. Y. A CsPbBr₃ Perovskite Quantum Dot/Graphene Oxide Composite for Photocatalytic CO₂ Reduction. *J. Am. Chem. Soc.* **2017**, *139*, 5660.
- (4) Jing, L. Q.; Qu, Y. C.; Wang, B. Q.; Li, S. D.; Jiang, B. J.; Yang, L. B.; Fu, W.; Fu, H. G.; Sun, J. Z. Review of photoluminescence performance of nano-sized semiconductor materials and its relationships with photocatalytic activity. *Solar Energy Materials and Solar Cells* **2006**, *90*, 1773-1787.
- (5) Zhou, L.; Xu, Y.-F.; Chen, B.-X.; Kuang, D.-B.; Su, C.-Y. Synthesis and Photocatalytic Application of Stable Lead-Free Cs₂AgBiBr₆ Perovskite Nanocrystals. *Small* **2018**, *14*, 1703762.
- (6) Guo, S.-H.; Zhou, J.; Zhao, X.; Sun, C.-Y.; You, S.-Q.; Wang, X.-L.; Su, Z.-M. Enhanced CO₂ photoreduction via tuning halides in perovskites. *J. Catal.* **2019**, *369*, 201-208.
- (7) Wan, S.; Ou, M.; Zhong, Q.; Wang, X. Perovskite-type CsPbBr₃ quantum dots/UiO-66(NH₂) nanojunction as efficient visible-light-driven photocatalyst for CO₂ reduction. *Chem. Engineer. J.* **2019**, *358*, 1287-1295.
- (8) Xu, Y.-F.; Wang, X.-D.; Liao, J.-F.; Chen, B.-X.; Chen, H.-Y.; Kuang, D.-B. Amorphous-TiO₂-Encapsulated CsPbBr₃ Nanocrystal Composite Photocatalyst with Enhanced Charge Separation and CO₂ Fixation. *Adv. Mater. Interfaces* **2018**, *5*, 1801015.
- (9) Kong, Z.-C.; Liao, J.-F.; Dong, Y.-J.; Xu, Y.-F.; Chen, H.-Y.; Kuang, D.-B.; Su, C.-Y. Core@Shell CsPbBr₃@Zeolitic Imidazolate Framework Nanocomposite for Efficient Photocatalytic CO₂ Reduction. *ACS Energy Lett.* **2018**, *3*, 2656-2662.
- (10) Ou, M.; Tu, W.; Yin, S.; Xing, W.; Wu, S.; Wang, H.; Wan, S.; Zhong, Q.; Xu, R. Amino-Assisted Anchoring of CsPbBr₃ Perovskite Quantum Dots on Porous g-C₃N₄ for Enhanced Photocatalytic CO₂ Reduction *Angew. Chem.* **2018**, *130*, 13758-13762.

- (11) Jiang, Y.; Liao, J.-F.; Xu, Y.-F.; Chen, H.-Y.; Wang, X.-D.; Kuang, D.-B. Hierarchical CsPbBr₃ nanocrystal-decorated ZnO nanowire/macroporous graphene hybrids for enhancing charge separation and photocatalytic CO₂ reduction *J. Mater. Chem. A* **2019**, *7*, 13762-13769.
- (12) Wu, L.-Y.; Mu, Y.-F.; Guo, X.-X.; Zhang, W.; Zhang, Z.-M.; Zhang, M.; Lu, T.-B. Encapsulating Perovskite Quantum Dots in Iron-Based Metal-Organic Frameworks (MOFs) for Efficient Photocatalytic CO₂ Reduction/ *Angew. Chem. Int. Ed.* **2019**, *58*, 9491-9495.
- (13) Wang, X.-D.; Huang, Y.-H.; Liao, J.-F.; Jiang, Y.; Zhou, L.; Zhang, X.-Y.; Chen, H.-Y.; Kuang, D.-B. *In Situ* Construction of a Cs₂SnI₆ Perovskite Nanocrystal/SnS₂ Nanosheet Heterojunction with Boosted Interfacial Charge Transfer. *J. Am. Chem. Soc.* **2019**, *141*, 13434-13441.

Chapter 5

Summary and future direction

In this thesis, the advantageous characteristics of MHPs for the development of photocatalytic materials, such as tunable bandgap, efficient charge separation and suitable band position, have been exploited to drive various chemical reactions through the use of solar light. The photo-activity of the pure MHPs was improved through the development of composite materials and the formation of different heterojunctions such as type II single and dual heterojunctions and Z-scheme heterojunction. The main focus of this PhD work was centered around FAPbBr₃.

In Chapter 1, pure FAPbBr₃ and other Br-based MHPs were synthesized via the anti-solvent method which offers the advantage to handle large solution volumes and to tune the synthesis conditions for controlling the size and shape of MHP crystals and thus improving photophysical properties. These Br-based MHPs were used for the selective oxidation of benzylic alcohol to benzaldehyde in non-polar toluene solutions upon solar light irradiation. After 8 h of irradiation, 10 mg of FAPbBr₃ converted about 15% of a 0.1 mM benzylalcohol solution (2.5 mL toluene) with near 100% selectivity to benzaldehyde. Through the use of an apolar solvent, the MHP also showed a decent stability, after 5 reaction cycles (40 h in total) the FAPbBr₃ photocatalyst displayed no significant decrease in activity. The activity of the MHP photocatalyst was further improved by selecting a suitable co-catalyst and re-engineering the band structure of the composite photocatalyst. FAPbBr₃ was grown on top of TiO₂ by the *in-situ* anti-solvent growth. This FAPbBr₃/TiO₂ composite realized the highest conversion rate of benzyl alcohol when optimized (ca. 63% conversion, with 15 wt % FAPbBr₃ in 10 mg of FAPbBr₃/TiO₂ composite), being 4 times higher compared to the pristine MHP. However, after TiO₂ was incorporated, the increased activity comes at the cost of compromising the stability of the photocatalyst, which was mainly attributable to the breakdown of FAPbBr₃ following aldehyde and water generation. The overall excellent performance of MHPs in this selective oxidation was the first proof of organic synthesis with MHP photocatalysts.

The direct functionalization of saturated C–H bonds to form value-added chemicals is another challenging topic in modern chemistry. We next used FAPbBr₃ to photo-activate the C(sp³)-H bond in aromatic hydrocarbons to selectively form the corresponding alcohols and aldehydes. Similar to tailoring the

energetics within solar cells, the addition of an electron transfer layer (TiO₂) and hole transfer layer (NiO_x) allows for optimizing the conversion efficiency of the MHP photocatalyst, by improving charge separation properties. This TiO₂/FAPbBr₃/NiO_x achieved C(sp³)-H bond activation in toluene with high selectivity and high conversion rates of benzaldehyde generation from toluene (3800 μmol/g/h).

As the junctions mentioned above would weaken the redox ability of MHPs, an MHP based Z-scheme photocatalyst FAPbBr₃/Bi₂WO₆, has been developed by *in situ* growth, which assigns the strong redox abilities of electrons/holes to different activities sites. This Z-scheme composite photocatalyst could successfully couple CO₂ reduction to the selective benzyl alcohol oxidation. However, the conversion of benzyl alcohol on this Z-scheme photocatalyst with CO₂ is smaller compared to the conversion on FAPbBr₃/TiO₂ with O₂.

Although the reported FAPbBr₃ and FAPbBr₃-based photocatalysts display an outstanding activity in the studied photocatalytic reactions, instability issues always arise when long-term experiments exceeding 1 day were performed. In the future, improving the stability of MHPs is a potential direction to put forward MHPs photocatalysts. To enhance resistance to material degradation pathways, synthesizing core-shell structures (e.g. oxide capping layers) with near-perfect coverage will help to limit contact between the MHP and any polar solvent. MHP based solar cells have recently made progress with the instability issues associated with operation under ambient conditions, achieving reliable operation performance exceeding 1000 hours. This was achieved by engineering stable device architectures with a top and bottom HTL and ETL material fully covering the MHPs. Such stable sandwich structures with the MHP layer at the center sealed from the environment can be obtained through simple spin coating, CVD or ALD. Furthermore the HTL and ETL facilitate charge carrier separation and transportation. Increasing the valence charges of the dopant ions (doping of trivalent ions at the B site; e.g. Sb³⁺ in CsPbI₃) to increase the interaction between the ions and the crystal frame might give rise to intrinsically more stable perovskite structures without the need for additional functionalization.

Further expanding the reaction scope that can be photocatalyzed by MHPs should be focused on maximally employing the redox ability and coupling this to the synthesis of value-added organics. Several organic transformations have been reported so far, such as benzyl alcohol oxidation and C-H, C-O and C-N bond activations. Unlike water splitting and CO₂ reduction, MHPs offer an impressive activity in organic

transformations. However, the reported organic transformations by means of MHP photocatalysts are narrow, in comparison to known heterogeneous and homogeneous photocatalytic organic synthesis by other semiconductor photocatalysts or molecular photoredox catalysts. Expanding the photoredox reaction scope of MHPs by combining them with other molecule catalysts, such as Ir, Ru, Ni complexes, can be promising for high value-added organic synthesis. Further, aiming for high specificity and stereoselectivity is a promising direction for MHP-based photo-redox catalysis.

Safety Aspects

All experimental work performed during this thesis was executed in compliance with the Code of Practice for Safety in the Lab¹ and Basic Rules For Chemistry Practicals.² For all used chemicals, risk assessments have been drawn up and, accordingly, the necessary precautions were taken. Specific information for personal protection and precautions can be found on the website of Health, Safety and Environment (HSE) service³. In general, the chemicals used in this work should be handled with care (lab coat, safety goggles, gloves) as they are irritating or harmful in the case of contact with skin, eyes or by inhalation (H311, 331, EUH070). Furthermore, Pb salts and Ni salts should be manipulated correctly as most of them are toxic and teratogenic (H361d, 360D, 361f, 360F, 361fd, 360FD, 360Df, 360Fd) and long-term exposure may cause organ damage (H371, 372, 370) and cancer (H350, 350i). Specific caution is necessary when working with E4 products such as common solvents like toluene, which are highly flammable (H220, 222, 224, 225) or with DMSO and DMF that may cause cancer (H350, 351). Extra attention is necessary when working with nanoparticles, such as TiO₂, Bi₂WO₆ NPs to avoid inhalation (H311: toxic if inhaled).

1. <https://admin.kuleuven.be/sab/vgm/kuleuven/risicoactiviteiten/cv/cglp>
2. <https://admin.kuleuven.be/sab/vgm/kuleuven/en/riskactivities/cs/basic-rules-for-chemistry-practicals>
3. <https://admin.kuleuven.be/sab/vgm/kuleuven/en>

Publication list

11. **Huang H.**, Pradhan B., Hofkens J., Roeffaers B. J. M., Steele A. J., Solar-driven Metal Halide Perovskite Photocatalysis: Design, Stability, and Performance. *ACS Energy Letters*, 2020, 5, 1107-1123.
10. **Huang H.**, Zhou C., Jiao X., Yuan H., Zhao J., He C., Hofkens J., Roeffaers B. J. M., Long J., Steele J. A. Subsurface Defect Engineering in Single-Unit-Cell Bi₂WO₆ Monolayers Boosts Solar-Driven Photocatalytic Performance. *ACS Catalysis*. 2020, 10, 1439-1443.
9. Ming J., Liu A., Zhao J., Zhang P., **Huang H.**, Lin H., Xu Z., Zhang X., Wang X., Hofkens J., Roeffaers B. J. M., Long J., Hot π -Electron Tunneling of Metal-Insulator-COF Nanostructures for Efficient Hydrogen Production. *Angewandte Chemie International Edition*, 2019, 131, 18458-18462.
8. Bhatia H, Steele J. A, Martin C., Keshavarz M., Solís-Fernandez G., Yuan H., Fleury G., **Huang H.**, Dovgaliuk I., Chernyshov D., Hendrix J., Roeffaers B. J. M., Debroye E., Single-Step Synthesis of Dual Phase Bright Blue-Green Emitting Lead Halide Perovskite Nanocrystal Thin Films. *Chemistry of Materials*. 2019, 31, 6824-6832.
7. **Huang H.**, Yuan H., Zhao J., Solís-Fernández G., Zhou C., Seo J., Hendrix J., Debroye E., Steele J. A., Hofkens J., Long J., Roeffaers B. J. M., C(sp³)-H Bond Activation by Perovskite Solar Photocatalyst Cell, *ACS Energy Letters*, 2019, 4, 203-208.
6. **Huang H.**, Yuan, H., Janssen, K. P., Solís-Fernández, G., Wang, Y., Tan, C. Y., ... & Hofkens, J. Efficient and Selective Photocatalytic Oxidation of Benzylic Alcohols with Hybrid Organic-Inorganic Perovskite Materials. *ACS Energy Letters*, 2018. 3, 755-759.
5. Zhang M., Mitchell R. W., **Huang H.**, Douthwaite R. E. Ordered multilayer films of hollow sphere aluminium-doped zinc oxide for photoelectrochemical solar energy conversion. *Journal of Materials Chemistry A*, 2017, 42, 22193-22198.
4. **Huang H.**, Lin J., Zhu G., Weng Y., Wang X., Fu X., Long J. A Long-Lived Mononuclear Cyclopentadienyl Ruthenium Complex Grafted onto Anatase TiO₂ for Efficient CO₂ Photoreduction. *Angewandte Chemie International Edition*, 2016, 55, 8314-8318.
3. Zhuang H., Miao J., **Huang H.**, Long J., Zhang Y., Yang H., He S., Yang Y., Wang X., Liu B. Interim Anatase Coating Layer Stabilizes Rutile@Cr_xO_y Photoanode for Visible-Light-Driven Water Oxidation. *ChemPhysChem*, 2015. 16, 1352-1355.
2. **Huang, H.**, Lin, J., Fan, L., Wang, X., Fu, X., Long, J. Heteroatomic Ni, Sn clusters-grafted anatase TiO₂ photocatalysts: structure, electron delocalization, and synergy for solar hydrogen production. *The Journal of Physical Chemistry C*, 2015, 119, 10478-10492.
1. Fan L., Long J., Gu Q., **Huang H.**, Lin H., Wang X., Single-site nickel-grafted anatase TiO₂ for hydrogen production: Toward understanding the nature of visible-light photocatalysis. *Journal of Catalysis*, 2014, 320, 147-159.